Double J/ψ production at LHCb.

by

Andrew David Cook

A thesis submitted to the University of Bristol for the
degree of Doctor of Philosophy

in the
Faculty of Science
School of Physics

March 2015

Abstract

The production of J/ψ pairs in pp collisions at a centre of mass energy of $\sqrt{s} = 7$ TeV was studied using the LHCb detector. The cross section was measured in the region of J/ψ transverse momentum $p_{\mathrm{T}} \in [0;10]$ GeV/c and rapidity $y \in [2.0;4.2]$ using an integrated luminosity of 998 pb^{-1} to be 6.08 ± 0.40 (stat) $\pm$ 0.29 (syst) nb. The differential cross section was measured as a function of the J/ψ pair transverse momentum, the total mass of the J/ψ pair, the difference in rapidity of the J/ψ pair and the difference in azimuthal angle between the J/ψ pair.

Declaration of authorship

I, Andrew Cook, declare that the work in this dissertation was carried out in accordance with the requirements of the University's Regulations and Code of Practice for Research Degree Programmes and that it has not been submitted for any other academic award. Except where indicated by specific reference in the text, the work is the candidate's own work. Work done in collaboration with, or with the assistance of, others, is indicated as such. Any views expressed in the dissertation are those of the author.

Signed: ______________________________

Date: ______________________________

For Mum and John

Thanks for everything you’ve done for me.

Acknowledgements

Nearly five years ago, I was sat on a train pulling out of Bristol station, gripping a cornish pasty and covered in sweat. It was a beautiful Spring evening, and I had just ran half-way across the city, from the Robin Hood pub. The year was 2010; the LHC was still a day away from colliding its first 3.5 TeV beams, the Higg's boson was undiscovered and the selfie-stick hadn't even been invented. Unexpectedly, my phone rang, and on answering it, I was amazed to find it was an offer from the department I had just left. Somewhat dazed, I thanked the caller and indicated I would let them know my decision in a week or two, whereupon, it was made clear to me that the timescale was expected to be orders of magnitude smaller. The journey had only just begun.

I would firstly like to thank the Bristol LHCb group for giving me the opportunity to carry out this PhD, and the STFC for funding the position, both of which I am extremely grateful for. I would also like to thank UK-LO for giving me such great accommodation during my time in Switzerland and France; I feel hugely privileged to have been able to be at CERN at such a pivotal time, and will never forget the buzz around CERN the day the Higg's discovery was announced, or the day-to-day energy down the corridors and in the cafeteria.

Thank you to Nick for finding time to meet me in a very busy schedule and for reading through numerous drafts of my thesis. Thanks to Marco for your ideas and help on the double J/ψ analysis. Thank you to Anatoly for coming up with the original idea of a RICH HLT line and for many interesting discussions, and thanks to Tom for help with the RICH, Root, and for showing me your mad skillz. Thanks also to the rest of my colleagues in the wider collaboration whose work made this PhD possible.

Thank you to the friends I met during my PhD; I wish I had worked less and spent more time with you, but you invariably brightened my day. Except for Ed.

Thanks a lot to my sister and Mark, who let me take over their garage with all my stuff whilst I was in CERN and also let me stay there (in the house, not the garage) whilst I looked for a flat. Thanks to Faith and Honour for being super little scientists.

Finally, thank you to Becky for your support; particularly over the last few months, which I don't know how I would have got through without you.

Bristol, 7th March 2015.

"A hard beginning maketh a good ending."

John Heywood (1497 - 1580)

Author's contribution

In Chapter 3, all of the work detailed in Sec. 3.6, Sec. 3.7 and Sec. 3.8 was carried out by the author.

The analysis described in Chapter 4 was carried out in collaboration with another member of the Bristol group, Marco Adinolfi. Many parts of the study were repeated in parallel as an internal cross-check, including the event selection, reconstruction and selection efficiency, two dimensional invariant mass fit, one dimensional muon efficiency, reweighting of MC and the sPlot code. Work was done in collaboration on the fiducial acceptance, alternative fit models, global event cut efficiency, geometric efficiency, total cross-section and differential cross-sections. Marco Adinolfi estimated the trigger efficiency, binned muon efficiency and wrote the Toy MC code. The author carried out the work estimating the 'optimum' selection criteria, efficiency of the four muon DTF selection, a number of systematic errors (fit model, multiple candidate events and J/ψ polarisation) and the comparison with theoretical models.

Contents

Introduction

The production of heavy quark-antiquark bound states has been an intriguing area of study for over forty years. Whilst theoretical models of production of such ‘quarkonia’ states appeared soon after their discovery, the models are still unable to fully describe all of the experimental data.

The J/ψ particle, a bound state of a charm and anti-charm quark, was the first quarkonia resonance to be discovered [1] [2]. A number of theoretical models of production soon followed, including the Colour Singlet (CS) model, which was initially successfully applied at relatively low energies [3]. However, studies of J/ψ production at the Tevatron demonstrated that the CS model underestimated the measured cross-section by over two orders of magnitude [4]. Recent theoretical corrections, and new models such as the non-relativistic QCD (NRQCD) effective field theory, have closed the gap between prediction and experiment, but no theory can correctly describe both the p_{T} differential cross section and the polarisation distributions [5].

The errors on the existing experimental data are already smaller than on the corresponding theoretical models, therefore more diverse sources of experimental data are required, rather than higher precision measurements [6]. It is therefore instructive to study interactions where two quarkonia are produced in the same interaction, such as the production of two J/ψ. Additionally, double charmonium production offers insights into events where two hard scatterings occur, know as Double Parton Scattering (DPS), which are expected to be significant, and therefore important to understand, at the Large Hadron Collider (LHC) [7] [8].

Double J/ψ production was first observed in 1982 by the NA3 collaboration in multi-muon events in pion-platinum at 150 and 280 GeV [9]. It was measured at a hadron collider for the first time by the Large Hadron Collider Beauty (LHCb) experiment in 2010 [10]. More recently, Double J/ψ production has also been measured at the CMS [11] and D0 [12] experiments.

The LHCb experiment [13] is one of the four main experiments at the LHC [14]. It is designed to make precision measurements of CP violation and is optimised to study B meson decays, which also makes it ideally suited to exploit the high $c\bar{c}$ cross-section at the LHC. The 1 fb^{-1} of data recorded by the LHCb experiment in 2011 allows the total cross-section of double J/ψ production to be measured with much greater accuracy and kinematical distributions investigated, in order to further test theoretical models of quarkonium production.

Chapter 1 of this thesis presents a review of the existing experimental work and theoretical models of double J/ψ production. A description of the LHC and the LHCb detector is presented in chapter 2. In chapter 3, a project to optimise the selection of data for the alignment of the the LHCb Ring Imaging Cherenkov (RICH) detectors is described. The analysis of double J/ψ production at $\sqrt{s} = 7$ TeV is presented in chapter 4.

Chapter 1

Review of Double J/ψ Production

This chapter will first outline the discovery and properties of the J/ψ particle, in the context of the Standard Model. The leading theoretical models of production, namely the Colour Singlet Model, Colour Evaporation Model and the Non Relativistic QCD model, are examined. Existing double J/ψ experimental results are discussed, as are the predictions of the leading theoretical models for double J/ψ production. The creation of double J/ψ by two independent scattering events (Double Parton Scattering) is also discussed.

1.1 The Standard Model

The Standard Model (SM) of particle physics describes the properties of the fundamental particles and their interactions with the weak, electromagnetic and strong forces. The SM framework includes 12 spin-$\frac{1}{2}$ matter particles (fermions), which can be divided, according to their interactions, into quarks and leptons. Additionally, for each quark and lepton, there is a corresponding anti-particle. These particles can be further subdivided into three 'generations' following the hierarchy in mass; the first generation consists of the up (u) and down (d) quarks and the electron (e) and electron-neutrino (ν_e). The second generation is made up of the charm (c) and strange (s) quarks and the muon (μ) and mu-neutrino (ν_μ). The third generation comprises the top (t) and bottom (b) quarks and the tau (τ) and tau-neutrino (ν_τ). Forces are transmitted via the exchange of the force mediators (bosons), which have integer spin. The weak force is mediated by the exchange of the $W^{\pm}$ and Z bosons, the electromagnetic force by the photon and the strong force by the exchange of the gluon. The quarks interact with all three forces, the charged leptons with the weak and electromagnetic forces, and the neutral leptons only interact weakly. The SM also includes the Higgs boson, which gives mass to the fermions and the $W^{\pm}$ and Z bosons via their interaction with the Higgs field.

Quantum Chromodynamics (QCD) is the theory of the strong force, which mediates the interactions between particles that carry the colour charge, namely the quarks and gluons. Quarks can have 'red', 'green' and 'blue' colour charge with anti-quarks carrying corresponding 'anti-red', 'anti-green' and 'anti-blue'. As gluons both couple to and carry the colour charge, the strong force has the property that its coupling constant, α_s, decreases at higher energies and smaller distance scales. This behaviour, known as asymptotic freedom, means that at high energies perturbative calculations can be carried out with α_s as the parameter of expansion. Conversely, at larger distant scales, the behaviour of the QCD coupling constant leads to the phenomenon of 'colour confinement', whereby colour charged particles cannot be individually isolated, and can only be observed in colourless aggregated states. In this regime, perturbative calculations can no longer be carried out.

The production of J/ψ particles consists of both perturbative and non-perturbative QCD processes, and as such, it is an ideal testing ground for investigating the interplay between these two regimes.

1.2 J/ψ Discovery and Properties

The J/ψ resonance was discovered in November 1974 simultaneously by Ting *et al* at Brookhaven [1] and Richter *et al* at Stanford [2]. The particle they found was a bound state of a charm and anti-charm quark. Although the charm quark was previously predicted by the GIM mechanism [15], this was the first experimental evidence of its existence. Further discoveries, such as of $\psi(2S)$ [16], began to make it clear that the

Mode	Submode	Branching fraction
hadrons		87.7 ± 0.5 %
	virtual$\gamma \to$ hadrons	13.5 ± 0.3 %
	ggg	64.1 ± 1 %
	$\gamma\ gg$	8.8 ± 1.1 %
e^+e^-		5.94 ± 0.06 %
	$e^+e^-\ \gamma$	$(8.8 \pm 1.4) \times 10^{-3}$ %
$\mu^+\mu^-$		5.93 ± 0.06 %

Table 1.1: *J/ψ* decay modes and branching fractions [17].

J/ψ was one of a family of particles composed of $c\bar{c}$, as shown in Fig. 1.1, which were subsequently named charmonium. Alongside the later discovered bottomonium states, composed of $b\bar{b}$, they formed a group of particles, composed of a heavy quark and anti-quark, termed quarkonium.

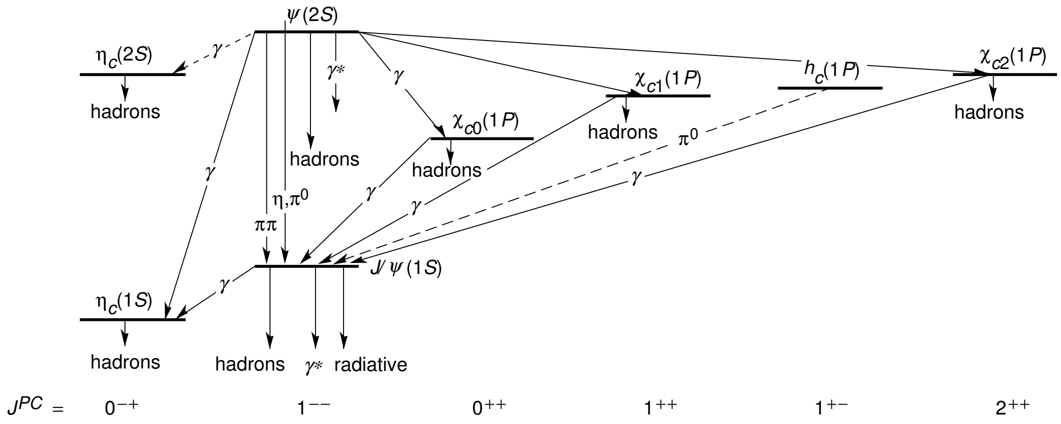

Figure 1.1: The mass spectrum of the charmonium family.

The different charmonium states can be characterised by their total angular momentum (J), spin (S) and orbital angular momentum (L). The *J/ψ* particle has the same quantum numbers as the photon, J = 1, S = 1 and L = 0 and is in a spin triplet state, which is represented in spectroscopic notation as 1^3S_1.

The mass of the *J/ψ*, 3096.916 ± 0.011 MeV/c^2 [17], lies below the open-charm meson threshold, which, coupled with the fact the *J/ψ* is colourless, means at the leading order it can only decay via three gluons or two gluons and a radiative photon. This leads to a relatively high di-lepton branching ratio, of the same order as the hadronic. Additionally, it means the *J/ψ* has a very narrow resonance of only 92.9 ± 2.8 keV [17]. The *J/ψ* decay modes are listed in Table 1.1.

1.3 Models of Quarkonium Production

At proton proton colliders, J/ψ particles can be produced in three ways

- **Prompt-direct:** J/ψ are produced directly in the primary *pp* collision.
- **Prompt-feed-down:** J/ψ are the decay products of charmonium that have been produced directly in the *pp* collision, (allowed charmonium transitions are shown in Fig. 1.1).
- **Non-prompt:** charmonium states are produced from the decay products of B mesons.

In this thesis, 'prompt' will refer to the prompt-direct and prompt-feed-down components, and 'direct' will refer to the 'prompt-direct' component. In order to differentiate between the prompt and non-prompt J/ψ, the long lifetime of the B mesons, which results in the non-prompt J/ψ being produced a significant distance from the primary production vertex, is usually exploited.

Since the discovery of the J/ψ resonance a number of models and effective QCD theories, which aim to describe the formation of quarkonia, have been formulated. However, despite many years of progress and endeavour, no model can explain all the experimental data. The leading models of production, which include the Colour Singlet model (CS), the Colour Evaporation model (CE) and NRQCD, are discussed in the following sections.

1.3.1 Colour Singlet Model

The Colour Singlet Model (CS) [18] was proposed shortly after the discovery of J/ψ particle. In the model, production is theorised to occur at two separate scales and therefore it is assumed the calculation can be factorised. In the first step the on-shell heavy quark pair is produced in a short distance process. The second step involves the transition from the heavy quark pair to the physical quarkonium, which takes place at longer distance scales of the order of the quarkonium size. The first step is assumed to be a perturbative QCD process, which can be computed with Feynman diagram techniques. The second step is described by a 'universal' wave function (i.e. it doesn't depend on the production process or kinematics) and uses the 'static' approximation; as the process concerns heavy quarks their relative velocity must be small, therefore it is assumed that they are at rest in the rest frame of the meson. It is further assumed that the colour and spin of the heavy quark pair are not changed during the formation of the physical quarkonium. Therefore, as the quarkonium must be colourless, the heavy quark pair are assumed to be in a colour singlet state, which is from where the theory derives its name.

A strength of the theory is its predictive power; the model only requires as input the Parton Density Function (PDF) and the universal wave function, which can be determined from experimental data from decay processes. Although it was initially successfully applied at leading order (LO) at relatively low energies [3], studies of J/ψ production at the Tevatron demonstrated that the model severely underestimated the cross-section and did not reproduce the p_{T} distribution shape [4]. Adding in the fragmentation contribution at next to leading order (NLO) [19] meant that the shape of the experimental distribution was reproduced. However, the magnitude of the direct J/ψ cross-section was still greatly underestimated, as can be seen in Fig. 1.2(a). Additionally, when the theory was applied to higher orbital angular momentum quarkonium it led to infrared divergences, implying that the simple factorisation approach used breaks down [18].

Recent calculations have shown large corrections at high energy to the CS model at NLO and next to next leading order (NNLO), as shown in Fig. 1.2(b). Although this means the CS model largely closes the gap between theory and experiment, given the size of the corrections at NLO and NNLO, it is not clear that the perturbative expansion in α_s is convergent [20].

1.3.2 Colour Evaporation Model

The Colour Evaporation Model (CE) [23] [24] was first introduced three years after the discovery of the J/ψ, and was later revived in 1996 [25]. Unlike the CS model, the CE model does not assume that the heavy quark pair is produced in a colour singlet state, but instead that its colour and spin are randomised by soft interactions that occur after production of the $Q\bar{Q}$ pair. Therefore, the probability for the $Q\bar{Q}$ pair to end up in a colour singlet state, rather than colour octet, is simply $\frac{1}{9}$. The CE model cross-section

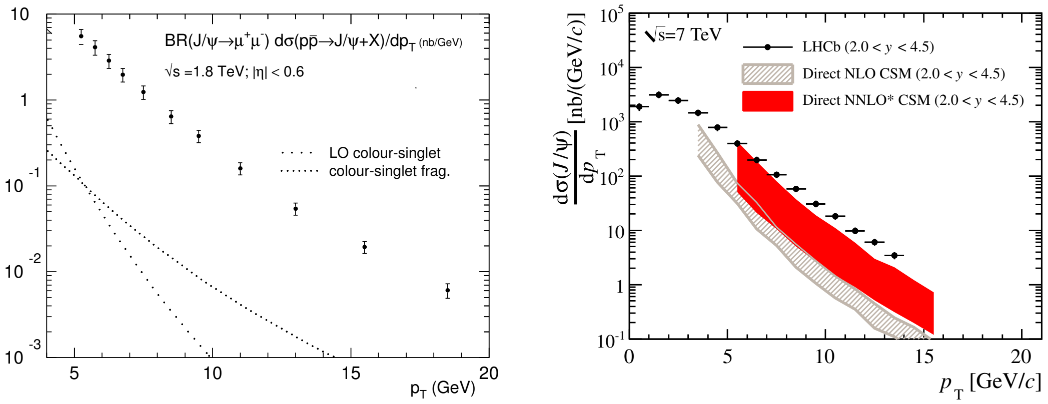

(a) (b)

Figure 1.2: Direct J/ψ production as a function of p_{T} at (a) CDF, with predictions from a LO CS model and CS fragmentation [21] and (b) LHCb, with predictions from NLO CS model and NNLO*, where the star indicates that not all of the terms in the NNLO have been calculated [22].

is calculated by integrating from the threshold to produce a heavy quark pair, $2m_Q$, up to the threshold for producing heavy quark mesons, $2m_{\bar{q}Q}$. The total cross-section to produce quarkonium in the CE model is therefore

$$\sigma_{onium} = \frac{1}{9}\int_{2m_Q}^{2m_{\bar{q}Q}} dm \frac{d\sigma_{Q\bar{Q}}}{dm} \tag{1.1}$$

The cross-section for a particular state, such as J/ψ, is then given by

$$\sigma_{J/\psi} = \rho_{J/\psi}\sigma_{onium} \tag{1.2}$$

where ρ is a factor that takes into account the distribution of the cross-section amongst the produced quarkonium states, which is assumed to be universal.

A comparison of a contemporary NLO CE model to prompt single J/ψ production at $\sqrt{s} = 7$ TeV is shown in Fig. 1.3 [22], which includes contributions from χ_c and $\psi(2S)$. The CE model reproduces the shape and magnitude of production well for mid-range values of p_{T}, but is less accurate for low and high values of p_{T}.

Although the CE model is phenomenologically reasonable and has an appealing simplicity, it has several limitations. The model cannot make any predictions about the polarisation of the produced quarkonium, which is an important test on the validity of other models. Additionally, the prediction of the universality of the ρ factor fails to

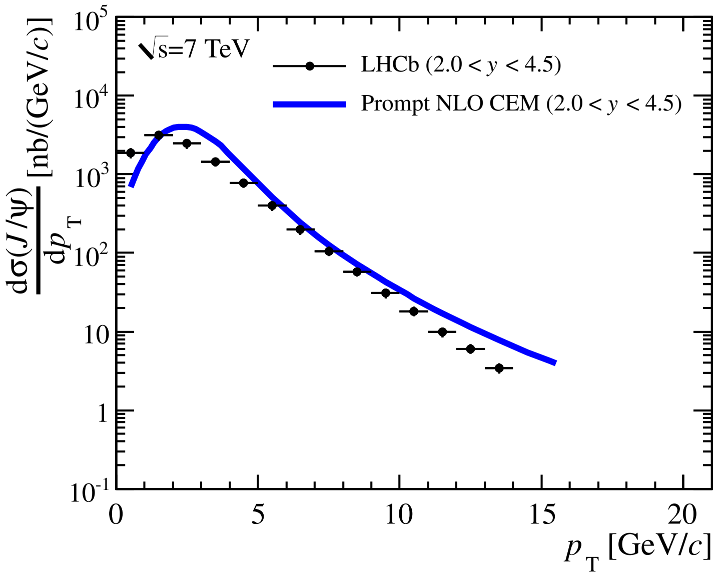

Figure 1.3: Prompt J/ψ production at $\sqrt{s} = 7$ TeV at LHCb as a function of p_T, with predictions from a NLO CE model [22].

replicate what is seen in experiments, where the ratio of different states varies according to the production process or the kinematics of production [18].

1.3.3 NRQCD

Non-Relativistic QCD (NRQCD) [26] [27] is an Effective Field Theory (EFT) which encompasses the CS model. Like the CS model, the production process is factorised into a long distance and short distance process, which represent the creation of the heavy quark pair and the formation of the physical quarkonium, respectively. The short distance component is process dependent, and can be calculated perturbatively using the strong coupling constant, α_s. The long distance non-perturbative process is universal and is taken into account via a sum of Long Distance Matrix Elements (LDME). The cross-section for the production of a quarkonium state H can therefore be written as

$$\sigma(H) = \sum_n \sigma_n(\Lambda)\langle\mathcal{O}_n^H(\Lambda)\rangle \tag{1.3}$$

where Λ is the cutoff of the effective theory, which determines the scale of the short distance and long distance processes. The index n denotes the colour, spin and angular momentum of an intermediate $c\bar{c}$ state. The cross-section for producing a heavy quark pair with properties n is represented by $\sigma_n(\Lambda)$ and the LDME are written as $\langle \mathcal{O}_n^H(\Lambda)\rangle$.

Potentially, there are infinitely many LDME to take into account, but they can be organised as a Taylor expansion in powers of the relative heavy quark velocity, v, and truncated at a fixed order in v. The LDME can be calculated from experimental data and potentially also from lattice calculations.

Unlike the CS model, NRQCD represents processes where the $Q\bar{Q}$ pair are produced in both a colour singlet state and a colour octet state. Heavy quark pairs formed in a colour octet state will emit one or more soft gluons in order that the physical quarkonium is in a colour singlet state. The CS model can be obtained from the NRQCD, by taking only the colour singlet terms in the leading order in v. However, the colour octet terms cancel the infrared divergences that occur in the CS model for higher orbital angular momentum quarkonium states.

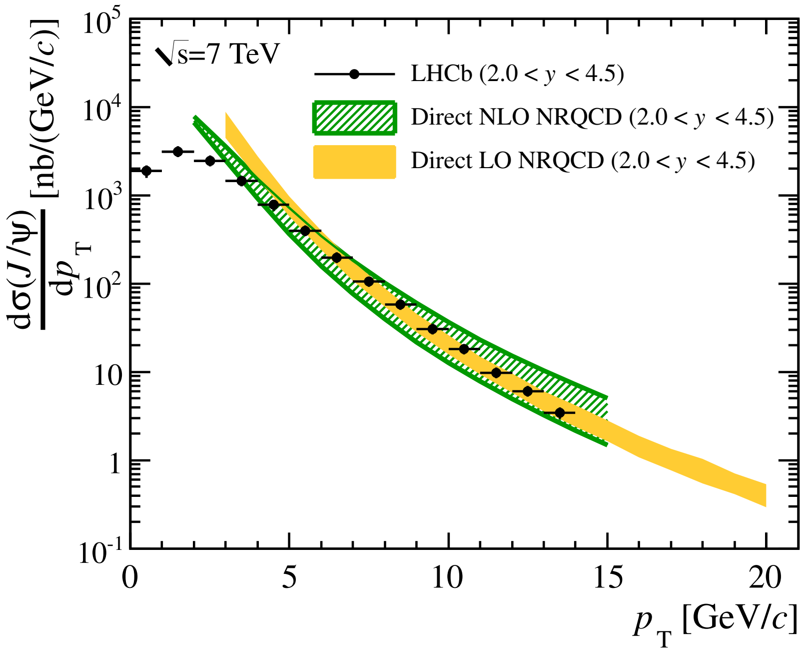

Figure 1.4: Direct J/ψ production as a function of p_T at LHCb, with predictions from LO NQCD and NLO NRQCD [22].

A comparison of NRQCD at LO and NLO as a function of p_T is given for direct J/ψ production at LHCb, in Fig. 1.4. It can be seen that the NRQCD reproduces the shape of the distribution well.

An additional important test of models of quarkonium production is how well the polarisation is predicted. The polarisation measurement of prompt J/ψ made by LHCb as a function of p_{T} [5] is shown in Fig. 1.5. The polarisation is almost flat along the p_{T} range and slightly negative, which means that it is longitudinally polarised. Predictions from a number of models are also shown, which include a NLO CS model and three different NLO NRQCD predictions that differ in the way they evaluate the LDME. The experimental results do not agree well with the NLO CS, which predicts increasingly large longitudinal polarisation as p_{T} increases. The best agreement between experiment and theory is given with the NRQCD predictions from Ref. [28], shown in green, which predicts almost no polarisation.

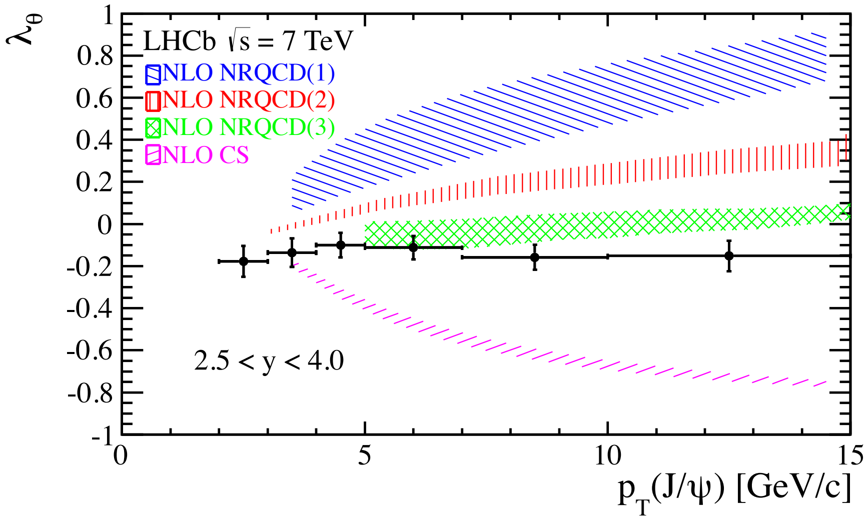

Figure 1.5: Polarisation of prompt J/ψ from the LHCb experiment in the rapidity range $2.5 < y < 4.0$ [29], with a NLO CS model with magenta diagonal lines [30] and three different NLO NRQCD predictions, in blue diagonal lines [30], red vertical lines [31] green hatched lines [28]

It has been suggested that a possible reason for the general failure of NRQCD to predict the polarisation in the case of charmonium production, is that the charmonium system is too light to ignore relativistic effects and that the expansion in the relative quark velocity may similarly not be valid [32].

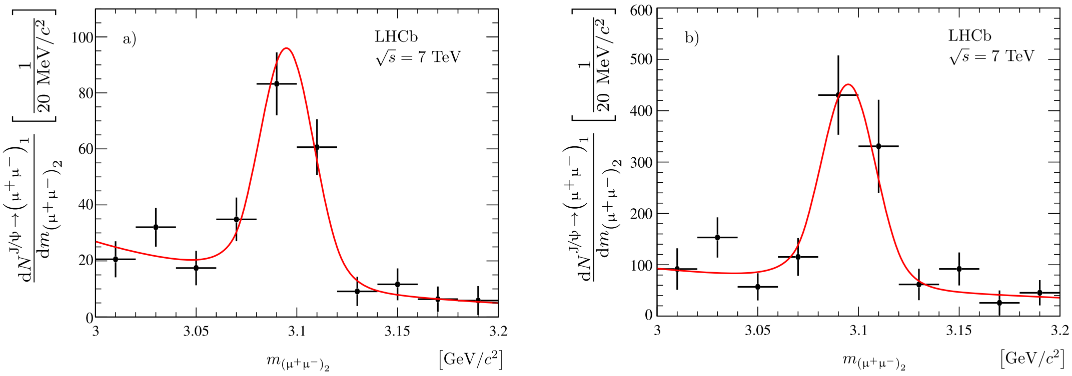

(a)

(b)

Figure 1.6: Fitted yields of $J/\psi \to (\mu^+\mu^-)_1$ in bins of $(\mu^+\mu^-)_2$ (a) the raw signal yield (b) the efficiency corrected yield. The red line shows a fit with a double-sided Crystal Ball function for the signal and a exponential for the background [10].

1.4 Double J/ψ Production

Double J/ψ production was first observed in 1982 by the NA3 collaboration in multi-muon events in pion-platinum interactions at 150 and 280 GeV [9]. It was later observed in proton-platinum collisions at 400 GeV [33]. At NA3, the cross section was dominated by the quark-antiquark annihilation channel.

At the LHC, the main contribution to double J/ψ production comes instead from gluon gluon fusion, as discussed further in Sec. 1.4.1. Double J/ψ production was measured at LHCb using 37.5 pb^{-1} of 2010 data at a centre of mass energy of $\sqrt{s} = 7$ TeV and the cross section was found to be 5.1 ± 1.0 (stat) ± 1.1 (syst) nb [10] with $p_\mathrm{T} < 10$ GeV, in the rapidity, y, range of $2 < y < 4.5$, with rapidity defined by

$$y = \frac{1}{2}\ln\frac{E + p_z}{E - p_z} \tag{1.4}$$

where E is the total energy and p_z is the momentum along the beam axis. The fitted yields and the efficiency corrected yield from this study can be seen in Fig. 1.6.

The CMS collaboration has also investigated double J/ψ production [11]. Using an integrated luminosity of $4.73 \pm 0.12\ \mathrm{fb}^{-1}$ the study extracted 446 ± 23 signal events. The cross section, assuming unpolarized prompt J/ψ, was 1.49 ± 0.07 (stat) ± 0.14 (syst) nb. Maximal estimates of the unknown double J/ψ polarisation increased the cross-section by as much as 27 % or decreased it by a factor of 31 %. The differential cross section as a function of the double *J/ψ* invariant mass can be seen in Fig. 1.7. Additionally, the D0 collaboration have recently also made a measurement of double *J/ψ* production [12]. The cross-section for double *J/ψ* events was calculated as 169 ± 15(stat) ± 38(sys) fb.

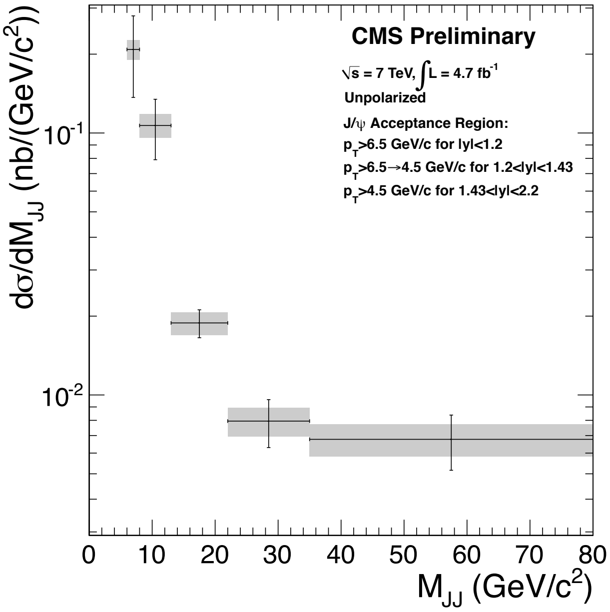

Figure 1.7: Differential cross-section for prompt double *J/ψ* production as a function of the double *J/ψ* invariant mass at the CMS experiment. The error bars show statistical and systematic errors added in quadrature, the grey boxes represent statistical errors only [11].

1.4.1 Theoretical Double *J/ψ* Production

Double *J/ψ* production at the LHC is dominated by gluon gluon fusion [7], with the cross-section being over three orders of magnitude lower than for single *J/ψ* production [10]. This difference in cross-section is due both to kinematic reasons, because of the requirement of producing larger mass, and also because the perturbative component in double production starts at higher orders of α_s. The CS Feynman diagrams for double *J/ψ* production start at order α_s^4, whereas in single *J/ψ* production they begin at order α_s^3. The 31 Feynman diagrams which account for the LO perturbative QCD contribution of CS charmonium pairs by gluon gluon fusion are shown in Fig. 1.8. In these LO CS diagrams the two initial gluons are in a colour singlet state and are C-even. Whilst the production of pairs consisting of *J/ψ*, η_c, or χ_c is allowed, the production of particles with different C-parity, such as *J/ψ* + χ_c, is prohibited. This therefore restricts the feed down from higher charmonium states to double J/ψ at LO [7]. However, it should be noted that beyond the LO CS contribution these restrictions on feed down do not exist. A LO CS model from Ref. [34] predicts a cross-section at LHCb of 3.2 nb with an uncertainty of 30 %, for J/ψ with $p_\mathrm{T} < 10$ GeV and rapidity between 2 and 4.2.

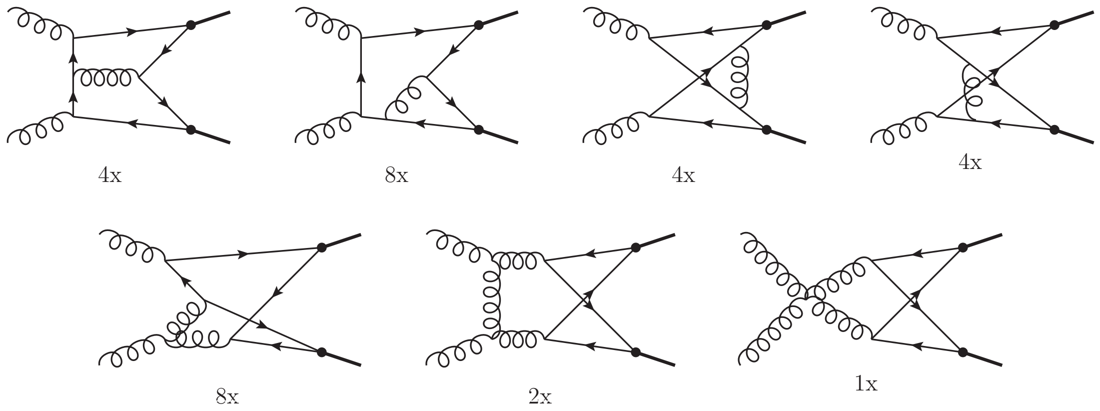

Figure 1.8: Leading order colour singlet Feynman diagrams contributing to $gg \rightarrow 2 \times J/\psi$ [7].

In single J/ψ production, significant corrections were seen at NLO and NNLO, as described in Sec. 1.3.1. Calculations have been carried out using NRQCD for double J/ψ production by Ref. [35] to investigate if there are similarly large corrections at NLO. An example of a Feynman diagram contributing towards the NLO corrections, at order α_s^5, is shown in Fig. 1.9. The prediction for $\sigma_{J/\psi\, J/\psi} \times \mathcal{B}^2_{\mu^+\mu}$, where $\mathcal{B}_{\mu^+\mu}$ is the branching ratio of J/ψ to $\mu^+ \mu^-$, for direct production at LO is $22^{+27.7}_{-13.1}$ pb and for NLO $24.3^{+30.6}_{-14.4}$ pb. This calculation is carried out for J/ψ with a p_T less than 10 GeV and a rapidity between 2 and 4.2. The LO and NLO predictions can be seen to be in good agreement, which demonstrates convergence of the perturbative series in this regime, although very large uncertainties exist on these values.

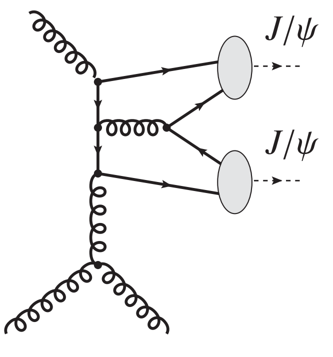

Figure 1.9: An example Feynman diagram contributing towards the NLO CS terms [35].

Colour octet contributions to double J/ψ production are only expected to become significant for larger values of p_{T}, approximately 10 GeV [36] [37]. The relative insignificance of the CO contribution in the low p_{T} region is due to the smallness of the colour octet LDMEs, however, the cross-section for the CO component falls more slowly as transverse momentum increases than the CS contributions, as can be seen in Fig. 1.10 [36]. The leading order CO Feynman diagrams contributing to double J/ψ production are shown in Fig. 1.11. NLO calculations have also shown the absence of significant CO contributions [35]. As such, it is not expected that CO contributions will be important in the LHCb fiducial volume.

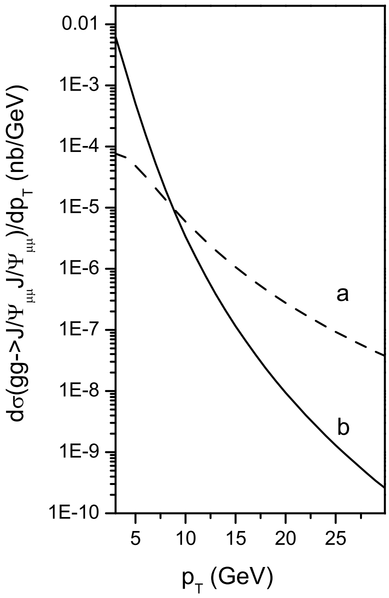

Figure 1.10: The p_{T} differential cross-section of double J/ψ at the LHC at $\sqrt{s} = 7$ TeV with (a) unpolarised colour octet contribution (b) unpolarised colour singlet [36].

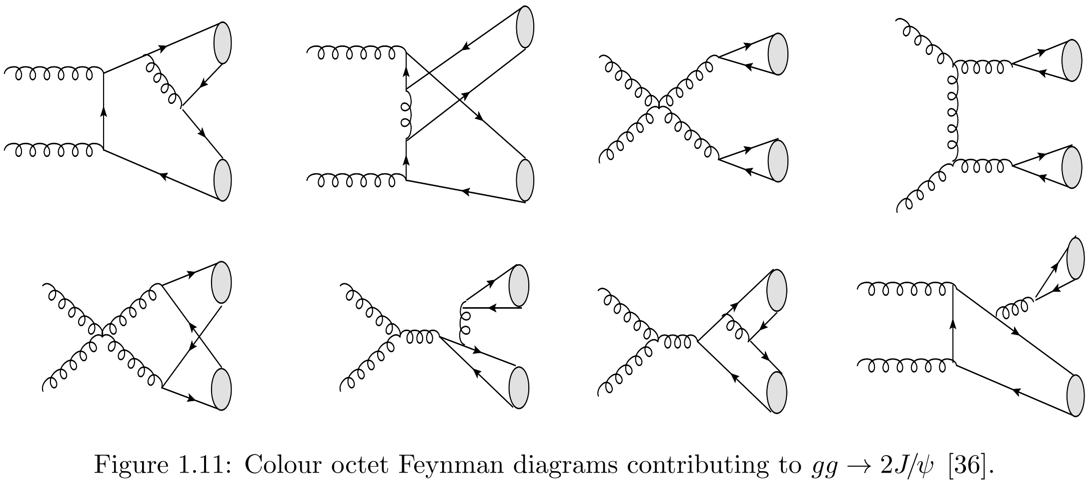

Figure 1.11: Colour octet Feynman diagrams contributing to $gg \to 2J/\psi$ [36].

1.5 Double Parton Scattering

Double parton scattering (DPS) events, where two hard scattering processes take place, as shown in Fig. 1.12, are expected to be significant in number at the LHC [38]. As such, it is important to investigate DPS in order to more fully understand the hadronic processes that are taking place. Experimental evidence for DPS was first seen by the AFS collaboration at CERN [39] and has been further investigated by a number of other experiments, including CDF and D0 [40].

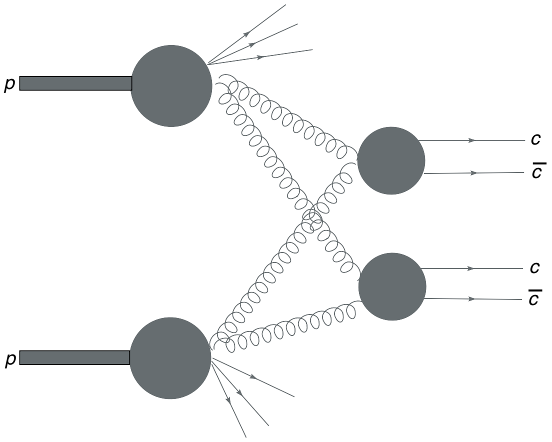

Figure 1.12: Creation of 2x$c\bar{c}$ via double parton scattering.

Theoretical calculations for DPS are based on the assumption that the DPS event can be decomposed into two single parton scattering (SPS) events, which are not correlated and do not interfere. Therefore, the DPS cross-section can be written as

$$\sigma^{DPS}(pp \to c\bar{c}c\bar{c}X) = \frac{1}{2\sigma_{eff}} \sigma^{SPS}(pp \to c\bar{c}X_1)\sigma^{SPS}(pp \to c\bar{c}X_2) \qquad (1.5)$$

where σ^{SPS} is the cross-section for SPS production of $c\bar{c}$ pairs. The factor $\frac{1}{2}$ is due to the assumption that the number of parton parton interactions per collision is distributed according to Poisson statistics. σ_{eff} is a factor that takes into account the probability that the ‘second’ SPS emission takes place given the ‘first’ SPS event has occurred.

In double J/ψ production at LHCb, it has been theorised that DPS may potentially be a significant mode of production [7] [41] [42] [8]. A prediction for the LO CS DPS cross-section of double J/ψ production at LHCb was made by Ref. [41], using the measured

	$\sigma^{prompt}_{experiment}$	$\sigma^{NLO,prompt}_{SPS}$	σ^{prompt}_{DPS}
LHCb	18 ± 5.3	$42.6^{+53.7}_{-25.3}$	$36.0^{+44.0}_{-12.8}$
D0	SPS: 112 ± 32, DPS: 57 ± 24	160^{+310}_{-97}	87^{+106}_{-31}
CMS	5.25 ± 0.52	$1.43^{+2.07}_{-0.81}$	$1.46^{+1.78}_{-0.52}$
ATLAS	N/A	$62.1^{+85.6}_{-34.8}$	$39.1^{+47.7}_{-13.9}$

Table 1.2: Theoretical predication of $\sigma_{J/\psi\, J/\psi} \times \mathcal{B}^2_{\mu^+\mu}$. Units in pb for LHCb and CMS and in fb for D0 and ATLAS. [35]

value of single J/ψ production at LHCb of 10.5 μb [22], and a value for σ_{eff} of 14.5 mb[*] [40]. A cross-section of 2 nb was calculated, which compares with the LO CS SPS prediction of 3.2 nb.

Predictions have also been calculated using NRQCD; in Ref. [44] the DPS cross-section is predicted to be ~ 3.3 nb, using a value of σ_{eff} of 14.5 mb. A NLO NRQCD prediction for DPS production at LHCb was calculated in Ref. [35], which used a value for σ_{eff} of 5.0 mb [12] that has been more recently calculated in double J/ψ events (see Sec. 1.5.1). The calculated values for LHCb and a number of other experiment can be seen in Table. 1.2. Whilst the DPS predictions for LHCb are significant, the NLO SPS predictions are already well above the measured cross-section, which leaves room for the DPS yield only when the very large uncertainties are accounted for [35].

Theoretical kinematic distributions have also been calculated, with the aim of disentangling the DPS and SPS components. DPS in double J/ψ production at the LHCb has been simulated for a number of kinematic distributions in Ref. [45]. The difference in azimuthal angle between the two J/ψ, $\Delta\phi$, is shown in Fig. 1.13(a). Naive expectations for the SPS $\Delta\phi$ distribution is that it would be characterised by the two J/ψ being produced back-to-back [8], with the uncorrelated DPS being characterised by a flat $\Delta\phi$ distribution. Whilst it can be seen in Fig 1.13(a) that the DPS distribution follows this pattern, the simple picture of back-to-back SPS production does not hold once the effects of Initial State Radiation (ISR) and the intrinsic p_{T} distribution of the partons, are included. The difference in rapidity between the two J/ψ, $|\Delta y|$, could potentially be more successful in distinguishing between DPS and SPS contributions. The theoretical

---

[*] Ref [43] has suggested that errors in the calculation of σ_{eff} means this value should actually be 12.0 mb. However, this would not significantly alter the DPS cross-section prediction.

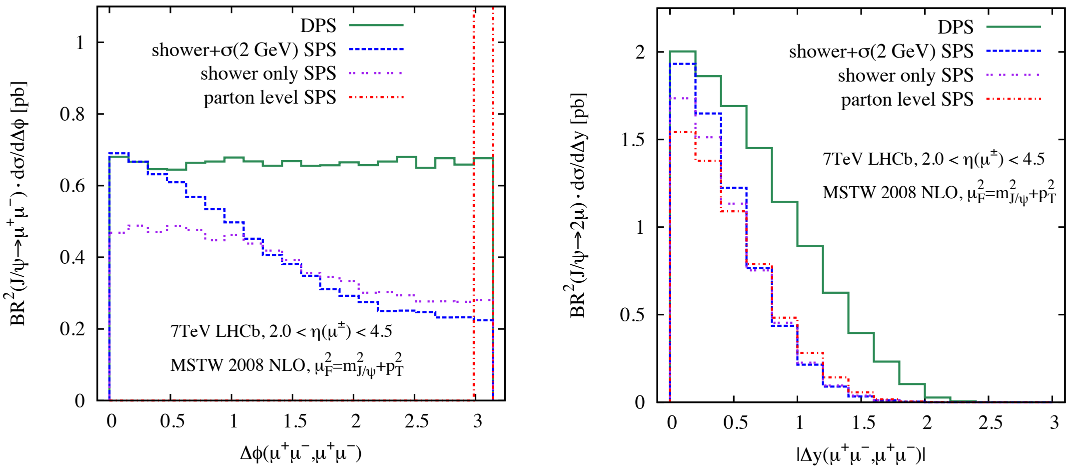

(a) (b)

Figure 1.13: (a) Difference in azimuthal angle, $\Delta\phi$ and (b) difference in rapidity, $|\Delta y|$ between the two J/ψ for DPS and SPS contributions at LHCb. DPS contributions are shown in green. The LO CS contributions are shown in red. The LO CS with the addition of initial state radiation (ISR) is shown in purple ('shower only'). The LO CS with ISR and effect of intrinsic p_T broadening is shown in blue ('shower+σ(2 GeV)') [44].

$|\Delta y|$ distribution is shown in Fig. 1.13(b); DPS is characterised by a much broader $|\Delta y|$ distribution than the SPS.

1.5.1 Experimental Results

The CMS collaboration has measured the differential cross-section as a function of the absolute rapidity difference between the two J/ψ mesons, $|\Delta y|$ [11], which can be seen in Fig. 1.14. They report that there is evidence for an excess in production for $|\Delta y| > 2.6$, which is a region that theoretical models suggest is populated exclusively with DPS production.

The D0 collaboration at Fermilab have measured double J/ψ production as a function of the absolute pseudorapidity difference between the two J/ψ particles [12], which is shown in Fig. 1.15. Using MC simulation of double J/ψ SPS and DPS processes they have individually fitted these contributions. In the region where the rapidity difference is greater or equal to 2 it can be seen the DPS events dominate over the SPS. The fraction of SPS events was found to be 0.70 ± 0.11 and the fraction of DPS events to be 0.30 ± 0.10. Using these results they calculated a value for σ_{eff} as $5.0 \pm 0.5(\text{stat}) \pm 2.7(\text{sys})$ mb.

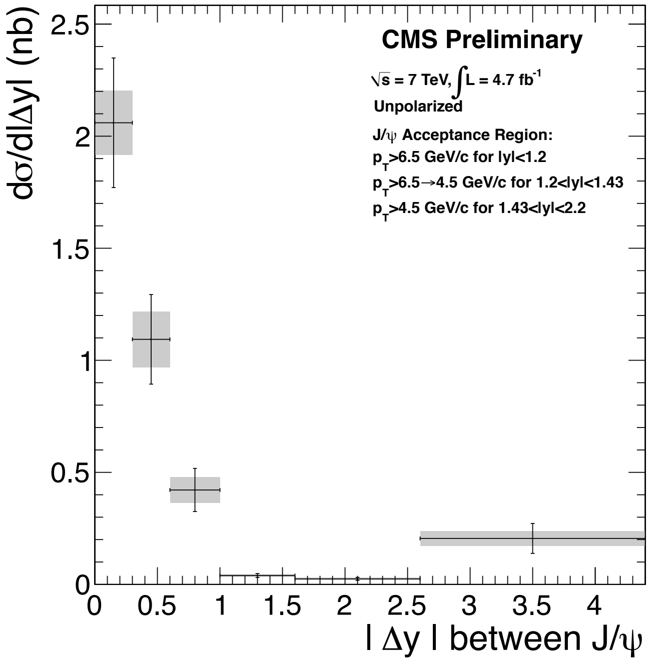

Figure 1.14: Differential cross-section for prompt double J/ψ production as a function of the absolute rapidity difference between J/ψ mesons. The error bars show statistical and systematic errors added in quadrature, the grey boxes represent statistical errors only [11].

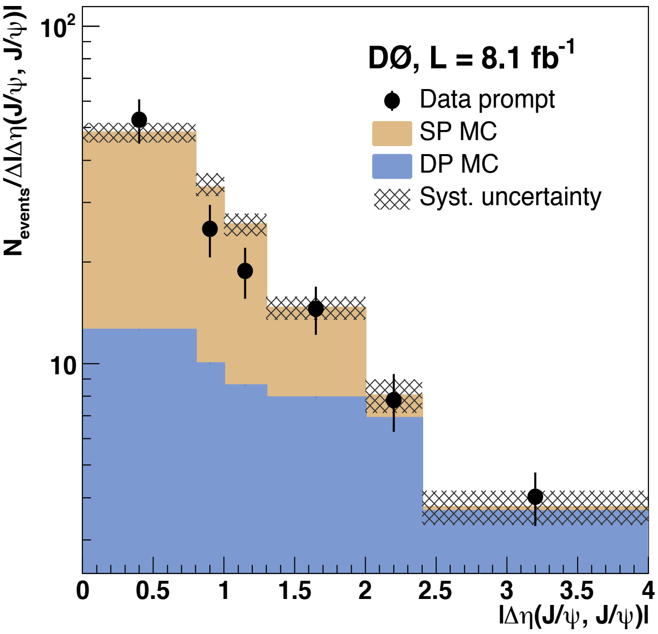

Figure 1.15: Differential cross-section for prompt double J/ψ production as a function of the absolute pseudorapidity difference between J/ψ mesons. The uncertainty band corresponds to the total systematic uncertainty on the sum of the SPS and DPS events [12].

1.6 Summary

Whilst quarkonia production has been studied for forty years, theoretical models fail to fully describe both the kinematic and polarisation experimental data. Three main models of production exist; the CS model, the CE model and NRQCD. As experimental uncertainties are already smaller than those of the theoretical models, it motivates the study of further sources of quarkonium production, such as double J/ψ production. Double J/ψ production can also offer insights into events with two hard scatterings, which are expected to be significant in number at the LHC and are theorised to be characterised by a broader difference in rapidity distribution than single parton scattering events.

There are a number of theoretical predictions for double J/ψ production at LHCb. The LO CS SPS model from Ref. [44] predicts a cross-section that is approximately three fifths the magnitude of the previous measured cross-section. Double parton scattering contributions to the cross-section may be as large, or larger than LO CS SPS contributions [44]. Next to leading order CS contributions may also be significant [22] as could NRQCD LO and NLO predictions [35], which therefore could reduce the need for a substantial DPS component. Colour octet contributions are thought to be negligible in the LHCb acceptance [35]. However, substantial theoretical uncertainties exist on all these predictions.

This study will measure the total cross-section and differential cross-sections of double J/ψ production, and compare these results to selected theoretical predictions.

Chapter 2

The LHCb Experiment

2.1 The Large Hadron Collider

The Large Hadron Collider (LHC) [14] is designed to test the Standard Model (SM) and probe for new physics, and is the most powerful particle accelerator ever built. The LHC, as shown in Fig. 2.1, was constructed in collaboration with over 100 countries by the European Organisation for Nuclear Research (CERN). Protons and heavy ions can be accelerated inside a 26.7 km long ring situated 45 to 170 m beneath the border of Switzerland and France.

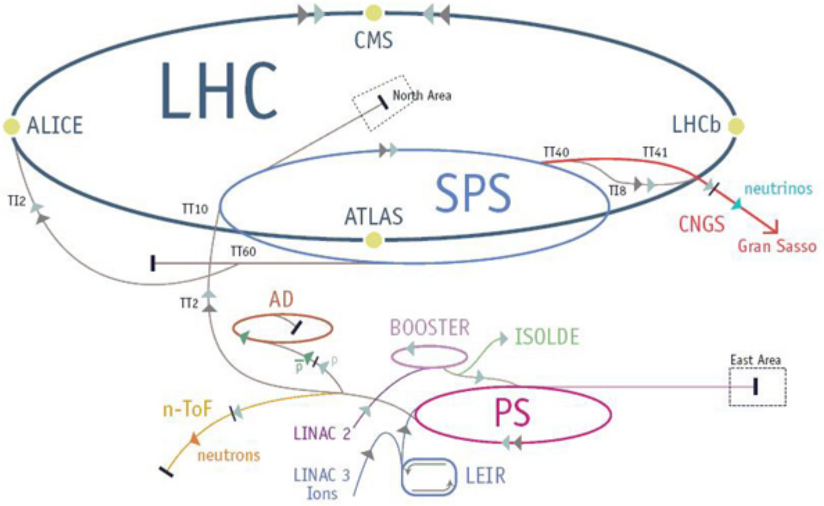

Figure 2.1: The LHC ring and the injector complex.

Particles are accelerated round the LHC ring by means of 1232 superconducting dipole magnets. These magnets are cooled by superfluid helium to below 2 K and operate at fields above 8 T. The LHC ring contains two vacuum cavities, with the polarity of the magnetic field being opposite in each cavity, which means particles with the same charge will travel in opposite directions in each cavity. The cross section of the LHC is shown in Fig. 2.2. Superconducting quadrupole magnets focus the beam.

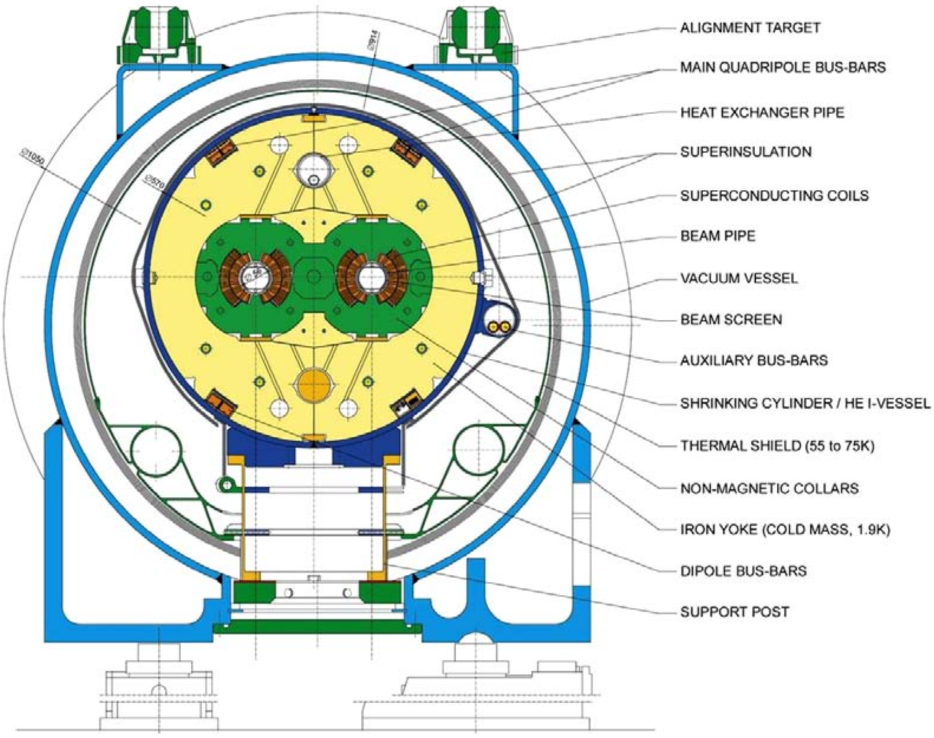

Figure 2.2: Cross section of the LHC dipole magnet [14].

Particles are accelerated in stages in the injector chain before transfer into the main ring. LHC protons are first derived from a hydrogen source, which are then ionised. The proton injection process begins with Linac2, where protons are accelerated to an energy of 50 MeV before injection into the Proton Synchrotron Booster (PSB), which increases the energy to 1.4 GeV. The Proton Synchrotron (PS) passes the protons onto the Super Proton Synchrotron (SPS) once they have an energy of 25 GeV. The SPS injects the particles into the main ring at an energy of 450 GeV. Heavy ions are instead initially accelerated by Linac3. The injector chain is shown in Fig. 2.1.

There are four points around the main LHC ring where the beams are collided; at these points lie the ATLAS, CMS, ALICE and LHCb experiments, as displayed in Fig. 2.1.

The ATLAS and CMS experiments are general purpose detectors, designed to hunt for the Higgs boson and direct signals of new physics such as supersymmetry, as well as making other physics measurements relevant to the energy frontier. Satisfying one of their main analysis goals, on the 4th July 2012 ATLAS and CMS jointly announced the discovery of a particle consistent with the Higgs boson [46] [47]. ALICE is optimised to study the quark-gluon plasma that is produced in lead-lead collisions. LHCb is designed to make precision measurements of bottom (B) and charm meson decays and is discussed further in the next section.

2.2 The LHCb detector

The Large Hadron Collider Beauty (LHCb) experiment [13] is designed to make precision measurements of CP violation and to search for new physics in quantum loop processes. To this end, it is optimised to study B meson decays, which also makes it ideally suited to study charm meson decays. It consists of a single-arm forward detector covering the pseudorapidity range, η, between 2 and 5. This design is motivated by the fact that at high energies the $b\bar{b}$ pairs are produced predominantly in the same forwards or backwards cone, as show in Fig. 2.3.

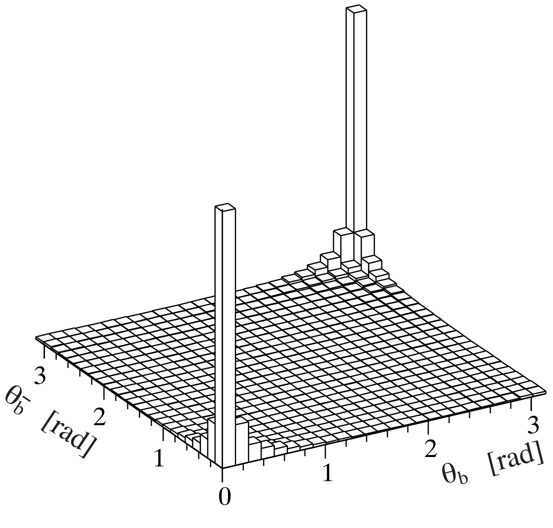

Figure 2.3: The polar angle of $b\bar{b}$ production in LHCb with respect to the beam line.

The LHCb detector is shown in Fig. 2.4. The z axis is defined along the beam pipe, the y axis in the vertical direction and the x axis, which with the z axis forms the bending plane, completes the right handed coordinate system. LHCb covers a polar angle, θ, from 10 mrad to 300 mrad along the y axis and from 10 mrad to 250 mrad along the x axis.

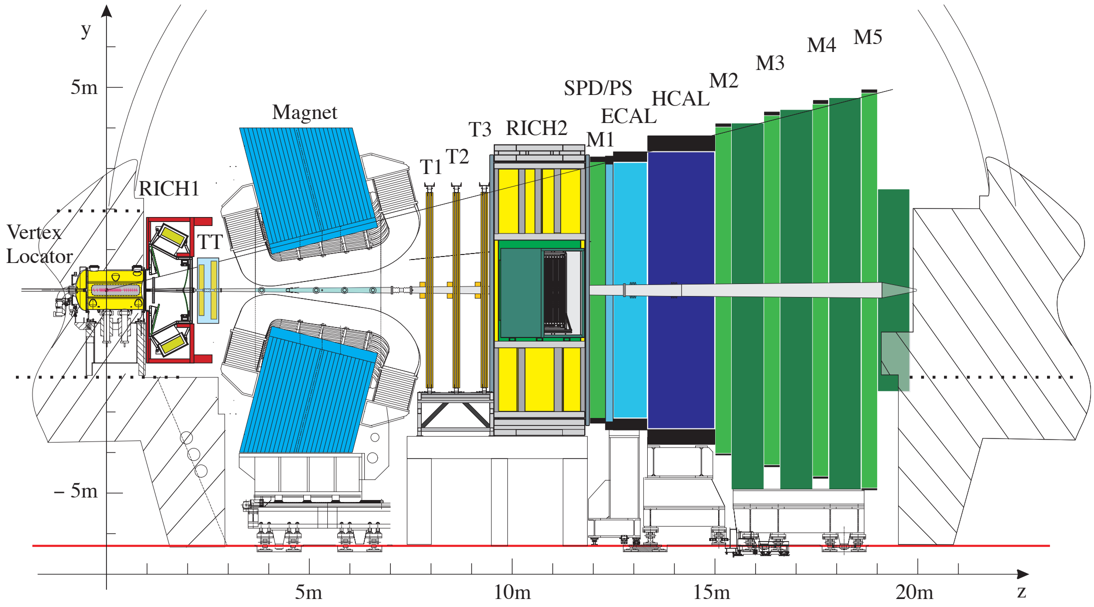

Figure 2.4: The LHCb detector in the $x - y$ plane [13].

LHCb operates at a much lower luminosity than the maximum LHC design luminosity of 10^{34} cm^{-2}s^{-1}, which is achieved by defocussing of the beams. The lower luminosity means that the number of events with multiple collisions is reduced, which allows events to be more cleanly reconstructed, particularly enhancing the ability to separate prompt B hadron decays. Additionally, the lower luminosity lessens the damage to the electronics and detector.

In the latter part of 2009, LHCb carried out its first pp collisions at $\sqrt{s} = 0.9$ TeV, which allowed testing of the detector systems and physics data to be taken. In 2010, the pp beam energy was increased to $\sqrt{s} = 7$ TeV. In the initial phase of running the luminosity quickly increased from 10^{28} cm^{-2}s^{-1} with few events with multiple collisions (‘pileup’) to 10^{32} cm^{-2}s^{-1} with up to 3 collisions per pp collision. This level of pileup was 4 times the nominal value and caused by the low number of pp bunches in the ring. Despite running conditions being beyond design expectations, data taking was not compromised. The integrated luminosity produced in 2010 was approximately 38 pb^{-1}.

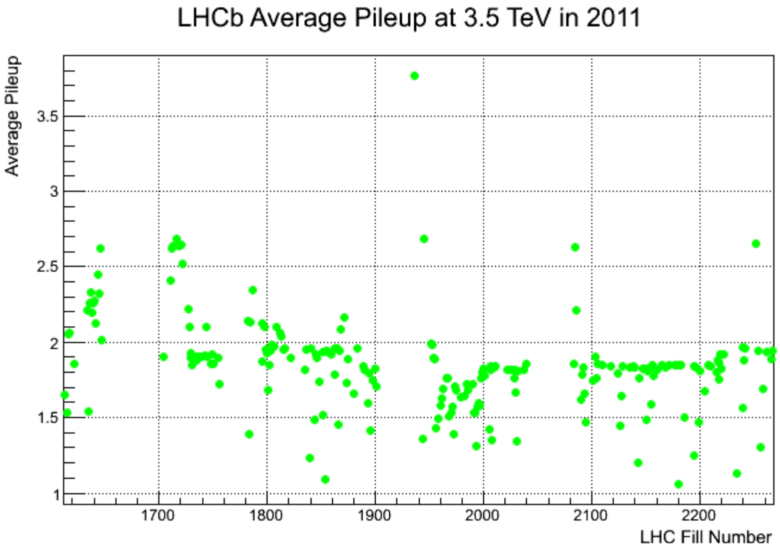

Figure 2.5: Average pile up as a function of time in 2011.

During 2011 the average luminosity was 2×10^{32} $\text{cm}^{-2}\text{s}^{-1}$, twice the nominal design value. Pileup was reduced to around 1.5 due to the increased number of *pp* bunches in the LHC, as shown in Fig. 2.5.

The beam energy was increased to $\sqrt{s} = 8\,\text{TeV}$ for data taking in 2012, producing an integrated luminosity of over 2 fb^{-1}. The integrated luminosity recorded by LHCb in the period 2010 to 2012 is shown in Fig. 2.6. At the beginning of 2013, collisions ceased for Long Shutdown 1 (LS1), in order that maintenance and upgrades on the LHC accelerator and experiments could be performed. Operation will recommence in early 2015 at a centre of mass energy of $\sqrt{s} = 13\,\text{TeV}$.

The subsystems that make up the LHCb detector are displayed in Fig. 2.4. The tracking system, outlined in section 2.2.1, makes measurements of charged particle trajectories. Accurate charged particle identification is carried out by two ring imaging Cherenkov sub-detectors, as detailed in section 2.2.2. A dipole magnet, described in section 2.2.3, provides a bending power of about 4 Tm. Photon, electron and hadron candidates are identified by the calorimeter system, described in section 2.2.4, and muons are identified by the muon system, as explained in section 2.2.5. The trigger selects interactions of the most interest so they can be written to storage for further analysis, described in

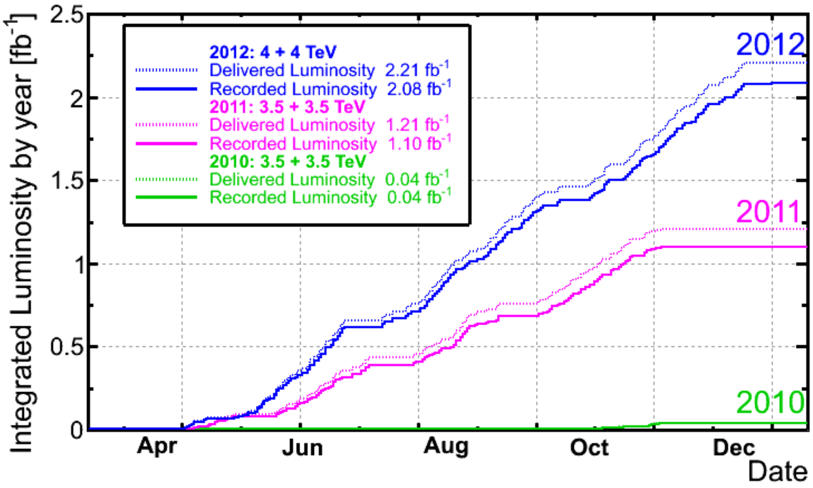

Figure 2.6: The integrated luminosity delivered by LHCb 2010 - 2012.

section 2.2.6. Analysis is carried out using the computing and software framework as detailed in section 2.2.7.

2.2.1 Tracking

The tracking system is made up of the Vertex Locator (VELO), the Trigger Tracker (TT) and Tracking Stations (T1-T2) [13]. The tracking system makes spatial measurements of charged particle trajectories from which the momentum can be calculated.

2.2.1.1 The Vertex Locator (VELO)

The VELO [13] [48] allows production and decay vertices to be precisely reconstructed. This ensures that decay lifetimes of B and charm mesons can be accurately measured and primary and secondary vertices separated. The ability to distinguish detached vertices can be used in the High Level Trigger (HLT) in order to enhance the B hadron content of data. Additionally, the VELO provides precise measurement of the impact parameter for charged tracks.

The VELO consists of 21 stations arranged along the beampipe, each measuring radial, r, and azimuthal, ϕ, coordinates. In every VELO module these coordinates are measured by two sensors called respectively the r-measuring sensor and the ϕ-measuring sensor,

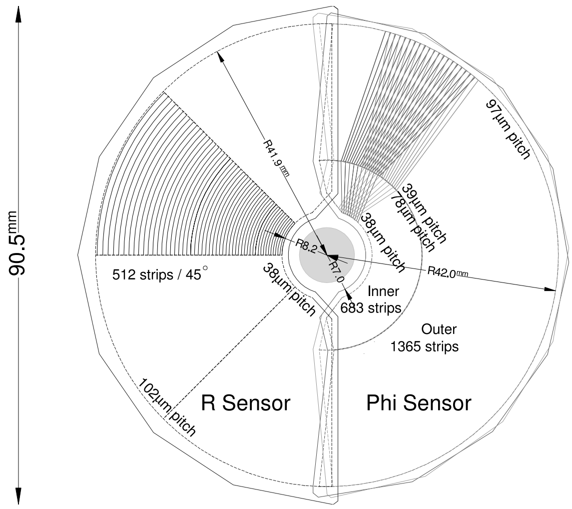

Figure 2.7: The VELO r-measuring sensor and ϕ-measuring sensor geometry. Only a portion of the strips are illustrated for clarity. [13]

as shown in Fig. 2.7. The z coordinate is taken from the knowledge of the position of the sensor. A radial coordinate system was chosen above a rectilinear, as it allows for faster reconstruction of vertices and tracks for use in the trigger. The stations are concentrated near the interaction point, as shown in Fig. 2.8, which reduces the average extrapolation distance from the primary vertex to the first hit and improves impact parameter measurements. The VELO detects particles from primary vertices in the range $|z| < 10.6$cm, with pseudorapidity between $1.6 < \eta < 4.9$, and is designed so that all tracks in this acceptance pass through at least 3 VELO modules.

The VELO is housed in a secondary vacuum, separate from the primary detector vacuum, to protect the primary vacuum against outgassing from the modules. The secondary vacuum is maintained by a thin layer of corrugated aluminium, in order that there is the minimum amount of material in the LHCb acceptance. The layer of aluminium also protects the module electronics against Radio Frequency (RF) pickup from the LHC beams and is therefore termed RF-foil. The RF-foils form the inner faces of the RF-boxes, which house the modules.

In order to operate as close to the beam as possible the VELO has a retractable design. When closed, the minimum distance of the VELO from the beam axis is 7 mm but it can be retracted to a distance of 3 cm, so as to not risk damage during beam injection.

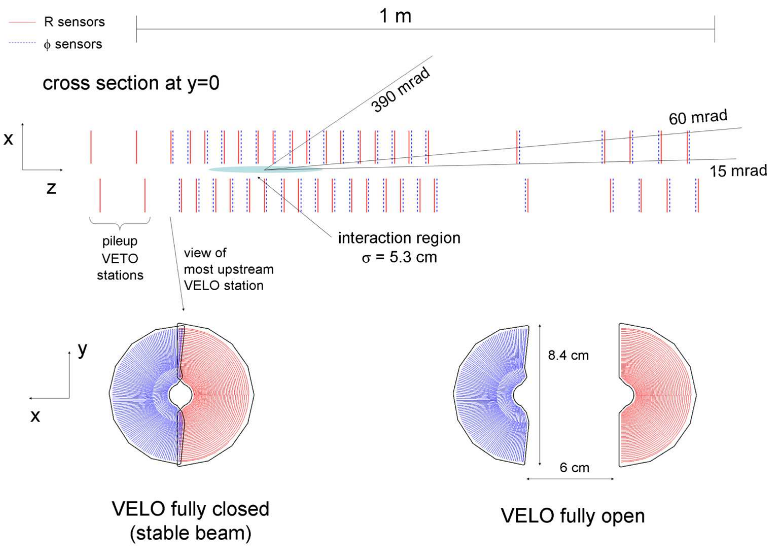

Figure 2.8: VELO cross section in the (x,z) plane, at y=0, with the detector closed. The two pile-up veto stations are located before the VELO sensors in the z direction. A face view of one of the VELO modules in both closed and open position is also shown [13].

To align the two halves of the VELO to the required relative accuracy of 100 μm, the half-stations overlap and are displaced by 1.5 cm in the z direction from each other.

In addition to the VELO modules, there are two stations upstream named the pileup veto system, which measure only radial coordinates. The pileup system provides an estimate of the number of primary proton-proton interactions in each bunch crossing. These stations are used by the L0 trigger in order to remove events with a high number of multiple collisions.

The performance of the VELO was studied in Ref. [49] and Ref. [50]. The vertex resolution along the x and y axis as a function of the number of tracks is shown and compared to MC in Fig. 2.9(a); the performance of data and MC can be seen to be in close agreement. The impact parameter resolution in the x direction as a function of the inverse transverse momentum, (which is almost identical to that in the y direction [50]), is shown in Fig. 2.9(b). In an average event the VELO has a spatial resolution of 4 μm in the z direction and 10 μm in the x and y direction [49]. A proper time resolution of approximately 50 fs was achieved.

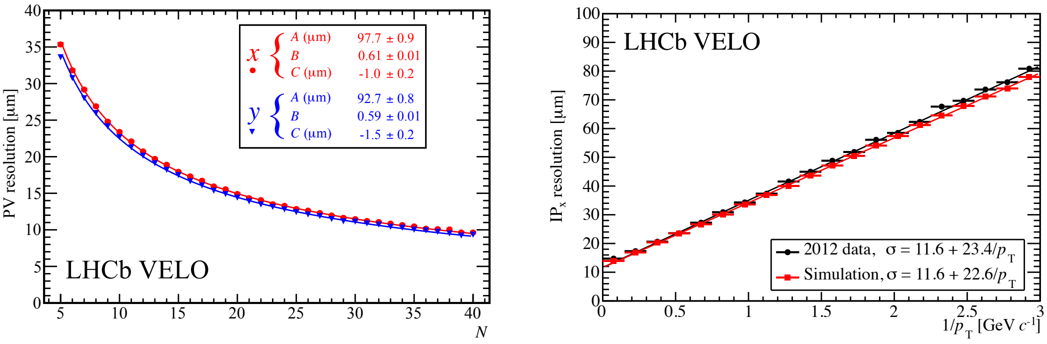

(a) (b)

Figure 2.9: (a) The vertex resolution along the x (red) and y (blue) axis as a function of the number of tracks, for events with one primary vertex, for 2011 data [50]. (b) The impact parameter resolution in the x direction as a function of the inverse transverse momentum, for 2012 data and MC [50].

2.2.1.2 The Trigger Tracker and Tracking Stations

The TT is positioned upstream of the RICH1, immediately before the magnet, and provides fast measurement of momentum for use in the HLT trigger. It also provides information for long lived particles decaying outside the VELO and is the only tracking station for low momentum particles, which the magnet deflects out of the acceptance.

The TT is 150 cm wide and 130 cm high, and covers the full LHCb acceptance with an active area of 8.4 m^2. It uses silicon microstrip sensors with a strip pitch of around 200 μm and is composed of 4 detector layers. There are vertical strips in the first and last layer, measuring the x co-ordinate. In order to allow 3D track reconstruction, the second and third layers are rotated by a small stereo angle, with the second layer, denoted u layer, rotated by -5 °, and the third, v layer, rotated by + 5 °. To aid the track reconstruction algorithm the four layers are arranged into two pairs, $x - u$ and $v - x$, separated by 27 cm along the beam axis. The TT has a single hit spatial resolution of about 50 μm.

The tracking stations T1-T2 are located downstream of the magnet. Two types of detectors make up these stations; Inner Tracker (IT) [51] and Outer Tracker (OT) [52]. The IT is a silicon strip detector with strip pitch of around 200 μm. The IT has an active area of 4.0 m^2 in a cross shaped configuration in the centre of the tracking stations, measuring approximately 120 cm wide and 40 cm high, as shown in Fig. 2.11.

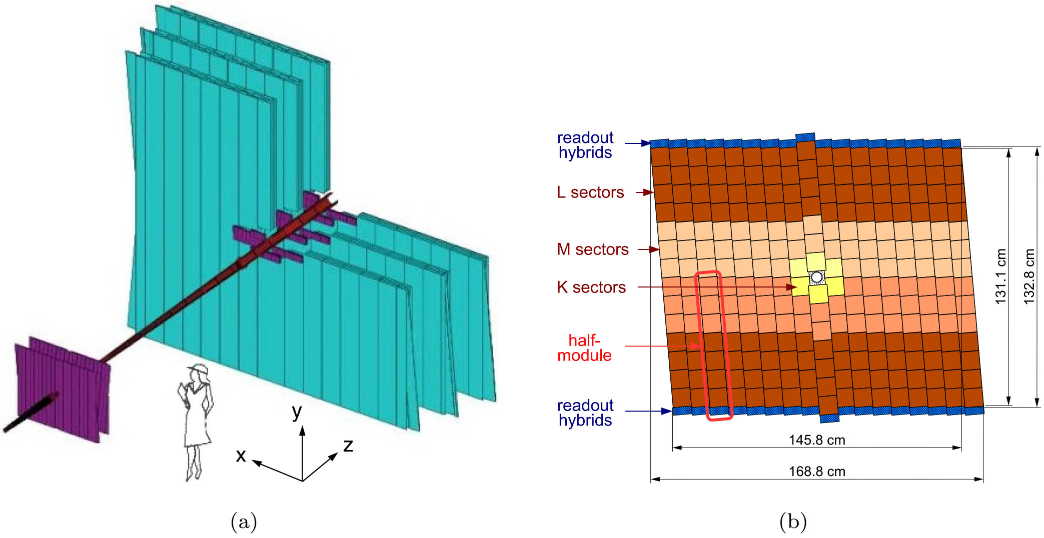

(a) (b)

Figure 2.10: (a) The TT and T1- T2 stations. (b) Layout of the third TT detector layer [13].

The OT consists of straw tube detectors of 4.9 mm diameter and 75 μm thick walls. The detectors are divided in this way due to the very high particle flux close to the beam pipe; the IT has $\sim$ 2 % of the acceptance area but receives 20 % of the tracks.

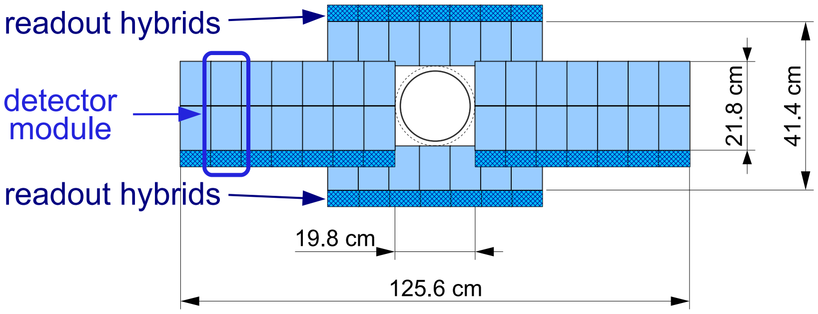

Figure 2.11: Layout of an x detector layer in a IT station [13].

2.2.1.3 Track Reconstruction

Information from the VELO, TT, IT and OT detectors are combined in order to reconstruct the trajectories of charged particles. Tracks are classified into separate categories depending on which tracking subsystems the particles have traversed:

- **Long tracks:** Tracks which have hits in all of the elements that make up the tracking, from the VELO to the T stations, are classified as long tracks. These tracks have the best determination of momentum and are therefore the most important for physics analysis.

- **Upstream tracks:** These tracks only have hits in the VELO and TT stations. Such tracks are normally lower momentum tracks, which the magnetic field has diverted out of the detector acceptance. As these particles pass through the RICH, they may emit Cherenkov photons and are useful in understanding backgrounds in the RICH.
- **Downstream tracks:** Tracks with hits only in the TT and T stations are classified as downstream tracks. These are generally decay products of longer lived particles that decay outside of the VELO.
- **VELO tracks:** Wide angle tracks that only have hits in the VELO are classified as VELO tracks, which are useful for reconstructing the primary vertex.
- **T tracks:** These only have hits in the T stations and normally come from particles that are produced in secondary interactions.

The various track types are illustrated in Fig. 2.12.

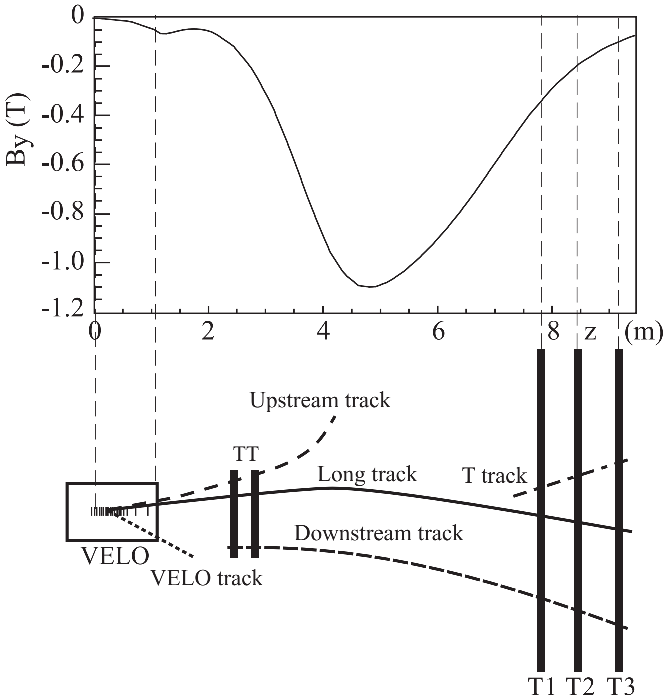

Figure 2.12: Schematic illustration of the LHCb track types, with the main magnetic field component (B_y) plotted above for reference as a function of the z coordinate [13].

2.2.2 The RICH

Particle identification (PID) is paramount for LHCb, particularly the ability to distinguish pions from kaons in B meson decays. Particle identification is carried out with two Ring Imaging Cherenkov Detectors, RICH1 and RICH2 [53] [13], which between them cover the momentum range from 1 GeV/c to approximately 100 GeV/c. The RICH detectors are optimised to distinguish charged pions from kaons but also to discern protons and, in combination with the calorimeter system, electrons, as shown in Fig. 2.13.

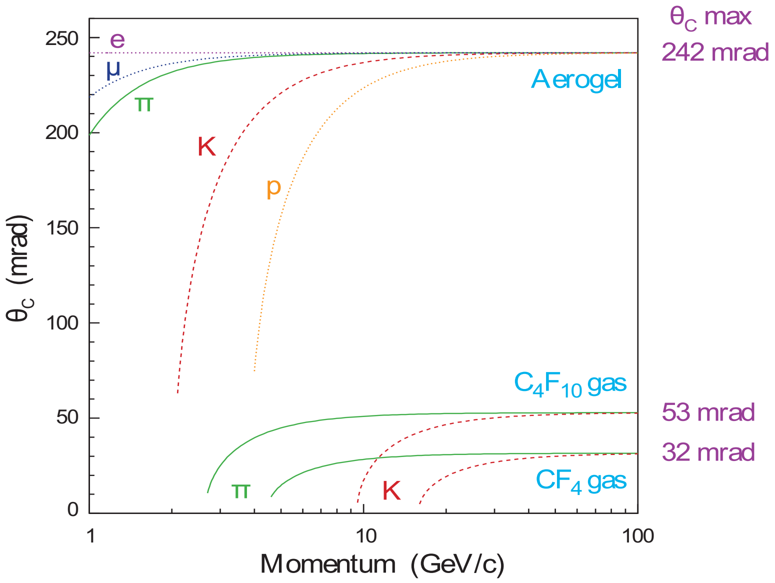

Figure 2.13: Cherenkov angle versus particle momentum for the three RICH radiators [13].

Cherenkov radiation is emitted at a fixed angle, θ_c, when a charged particle passes through a dielectric medium at a velocity greater than the velocity of light in that material. RICH detectors determine the velocity of a charged particle from measurement of the Cherenkov angle. The relation between the Cherenkov angle, θ_c, and the refractive index of the radiative material, n, and β the ratio of the velocity of the particle to that of the speed of light in a vacuum is given by

$$cos(\theta_c) = \frac{1}{n\beta}. \tag{2.1}$$

The above equation can be rewritten in terms of the mass, m, and momentum, p, of the particle

$$cos(\theta_c) = \frac{1}{n}\sqrt{1+\left(\frac{m}{p}\right)^2}. \tag{2.2}$$

From this equation it can be seen that by measuring the Cherenkov angle, refractive index and momentum of a particle, its mass can be calculated and hence the particle type can be determined.

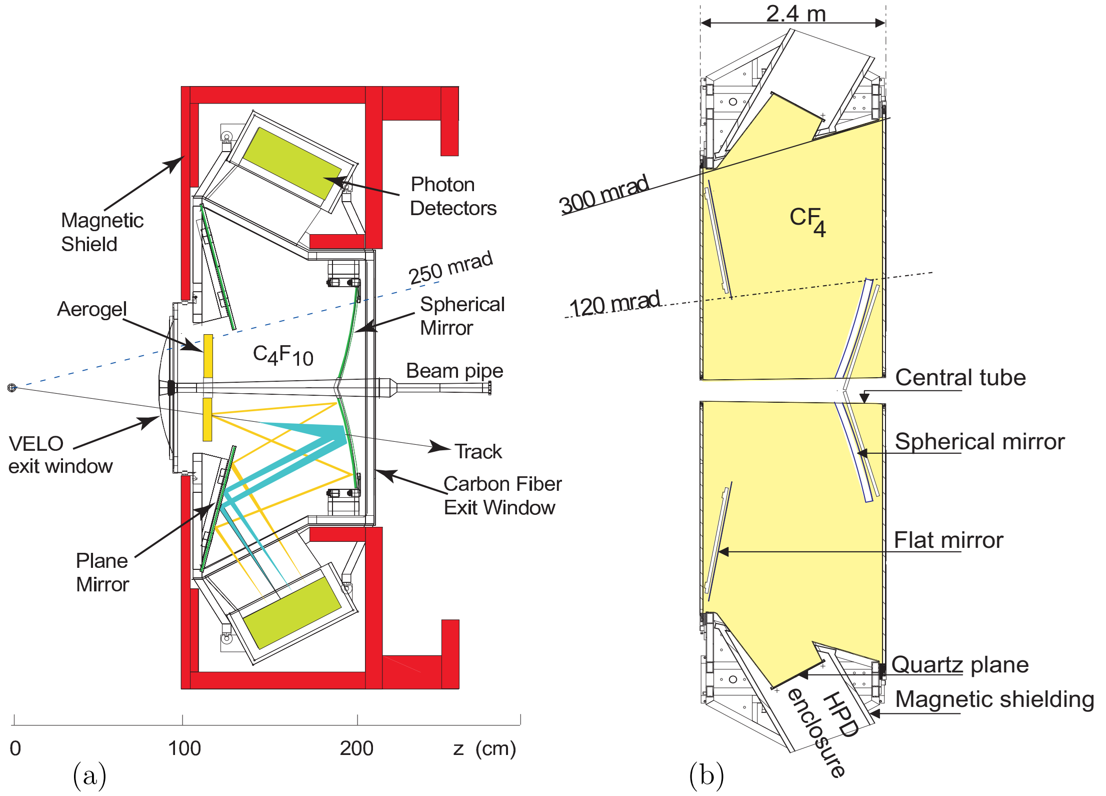

Figure 2.14: (a) The RICH1 and (b) RICH2 detectors [13].

RICH1 covers the low momentum tracks in the range $1 \rightarrow 60$ GeV/c and is the furthest upstream of the RICH detectors. It covers the entire LHCb acceptance from ± 25 mrad to ±300 mrad (horizontal) and ± 250 mrad (vertical). RICH1 uses aerogel and C_4F_{10} radiators. The aerogel has a refractive index of 1.03 at $\lambda = 400$ nm and is composed of hydroscopic silica aerogel. The C_4F_{10} radiator has a refractive index of 1.0014.

RICH2 is placed downstream of the magnet and covers a momentum range of 15 GeV/c to beyond 100 GeV/c. It has a smaller acceptance than RICH1, from ± 15 mrad to ±120 mrad (horizontal) and ± 100 mrad (vertical), which is targeted in the region where high momentum particles are produced, as illustrated in Fig. 2.15. RICH2, uses a CF_4

radiator and CO_2 in order to reduce scintillation light. The CF_4 radiator has a refractive index of 1.0005.

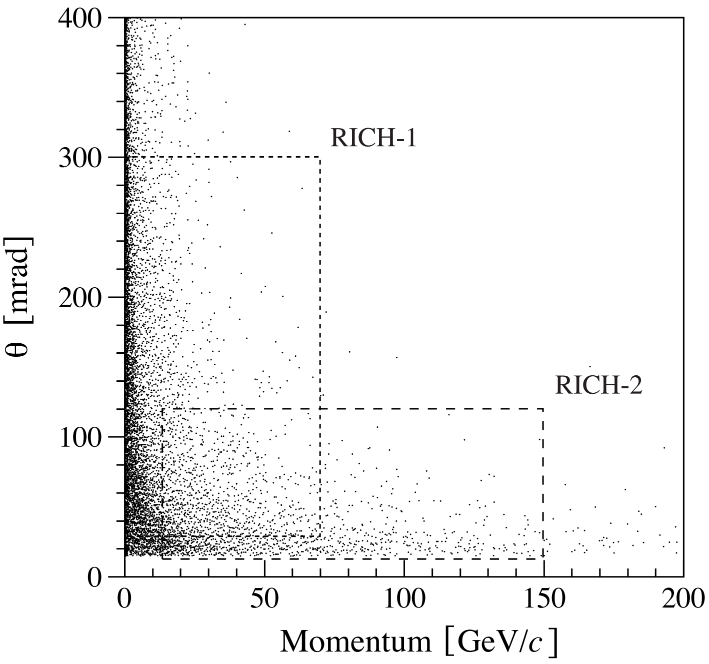

Figure 2.15: Polar angle, θ, versus momentum, for tracks in simulated $B_d^0 \to \pi^+ \pi^-$. The acceptance of the RICH1 and RICH2 detectors is shown [53].

In both RICH detectors the Cherenkov light is focused using a combination of flat and spherical mirrors, as shown in Fig. 2.14. Hybrid Photo Detectors (HPD), which are located outside the LHCb acceptance and protected from high magnetic fields by external iron shields, detect the Cherenkov photons. When the Cherenkov photons hit the HPD photocathode that surrounds the inner vacuum tube, it releases a photoelectron, which is accelerated by an applied voltage of between 10 to 20 kV, onto a silicon detector. The mean number of photoelectrons per track is 6.7 for the aerogel, 30.3 for C_4F_{10} and 21.9 for CF_4. A diagram of a HPD detector is shown in Fig. 2.16.

Particle identification is carried out by comparing the Cherenkov angle distribution with the expected distributions for the different particle hypothesis, using a log-likelihood technique. The hits in the HPD are combined with the reconstructed tracks and knowledge of the RICH geometry, in order to calculate the Cherenkov angle. The potential Cherenkov angle is calculated for all pixel-track combinations that could physically be associated, for all three radiators simultaneously and the likelihood is maximised by varying the particle hypothesis through electron, muon, kaon and proton for all tracks.

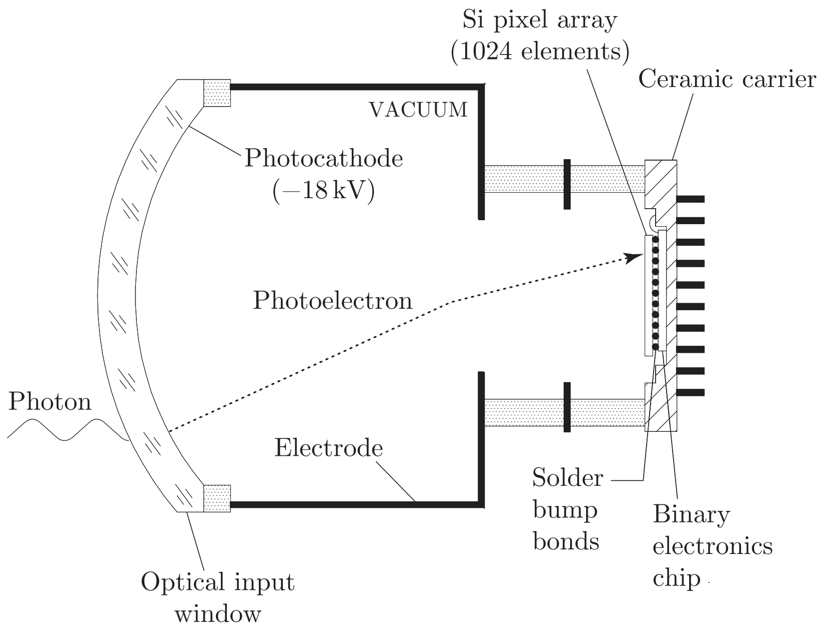

Figure 2.16: Diagram of a pixel HPD [13].

This technique is known as 'global pattern recognition'. The global technique is much more accurate than calculating the likelihood for each track individually, where the main photon background is from neighbouring tracks. Fig. 2.17 shows the reconstructed Cherenkov angles as a function of the track momentum in the RICH1 radiator, with the events of different mass distributed into distinct bands.

The performance of the RICH detectors has been studied using data from 2010 and 2011 [54]. The Cherenkov angular resolution for the RICH1 C_4F_{10} radiator has been found to be 1.618 ± 0.002 mrad, which compares to the expectation from simulation of 1.52 ± 0.01 mrad. The RICH2 CF_4 radiator has an angular resolution of 0.68 ± 0.02 mrad, which is in excellent agreement with prediction from simulation of 0.68 ± 0.01 mrad. In 2010 and 2011 running the aerogel was found to have an angular resolution of about 5.6 mrad, which is around 1.8 times worse than expected from simulation. This degradation in performance was thought to be largely caused by absorption of the RICH1 C_4F_{10} gas by the porous aerogel. In 2012, the aerogel was separated from the RICH1 gas.

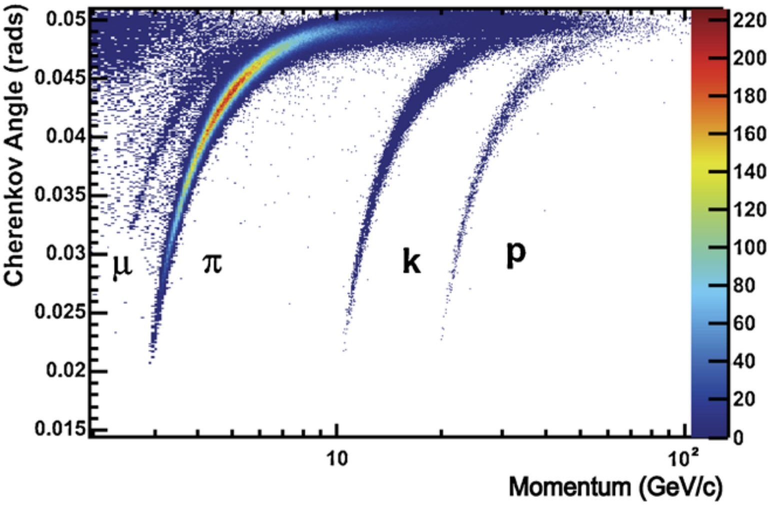

Figure 2.17: Reconstructed Cherenkov angle as a function of track momentum for the C_4F_{10} radiator in RICH1 [54].

2.2.3 The Magnet

In LHCb, the measurement of charged particle momentum is enabled with a warm dipole magnet [55] [13], which bends the tracks of charged particles in the $x - z$ plane. The magnet consists of two identical saddle shaped coils with sloping poles, symmetrically placed along the z plane, as shown in Fig. 2.18. This shape was designed to fit the LHCb acceptance of ±250 mrad vertically and of ± 300 mrad horizontally. Each magnet coil consists of fifteen 'pancakes' arranged in five groups of three. The magnet is cooled by the use of water.

The integrated magnetic field of a particle traversing the 10 m length of the tracking system is 4 Tm. The desired momentum resolution of the magnetic field integral $\int Bdl$ is of the order of 10^{-4}. To achieve this precision, a 3D Hall probe was designed to scan along the z axis of LHCb. From this, a momentum resolution of $\Delta p/p = 0.4$ % up to 200 GeV/c is attained [13].

The magnet polarity can be periodically reversed during data taking, in order to reduce systematic errors from possible left-right asymmetries.

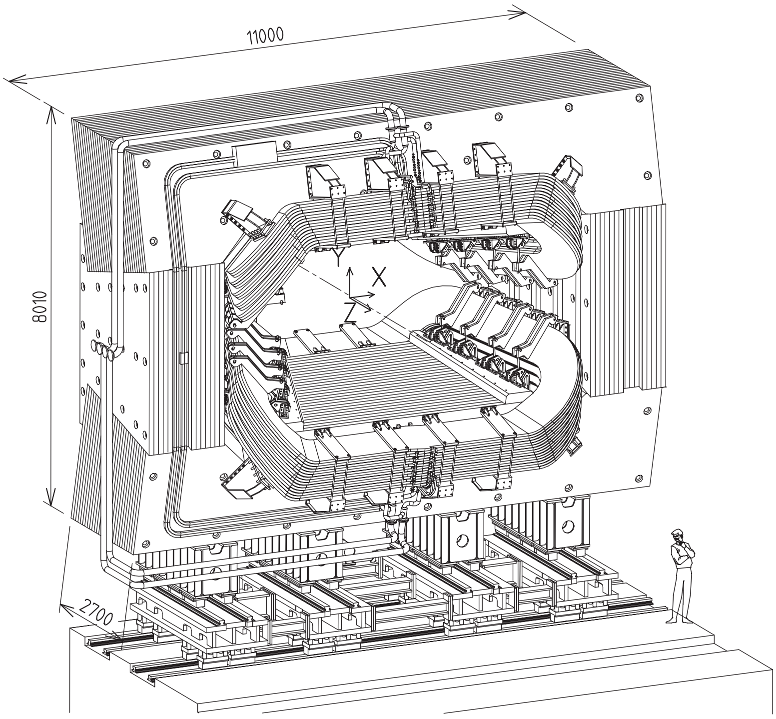

Figure 2.18: Perspective view of the LHCb dipole magnet. Units displayed are in mm [13].

2.2.4 The Calorimeter System

The calorimeter system [56] [13] provides electron, photon and hadron identification, energy and position measurements and is one of the main components of the L0 trigger. The electron L0 trigger, for example, uses the calorimeter system to select events with the highest E_{T}, in order to reject 99 % of inelastic proton proton interactions and enrich the proportion of B hadron events by a factor of 15. In order to carry out these functions a number of different components are combined within the calorimeter system.

The most downstream component of the calorimeter system is a Scintillator Pad detector (SPD). Ionising particles in the SPD cause scintillator light which can be used by the trigger to select charged particles. Upstream of the SPD is a 12 mm lead wall, which initiates electromagnetic showering to be detected by a Preshower detector (PS). The L0 uses this information to distinguish photons, electrons and π^0. The PS is followed by the Electro-magnetic Calorimeter (ECAL) which is succeeded by the Hadron Calorimeter (HCAL).

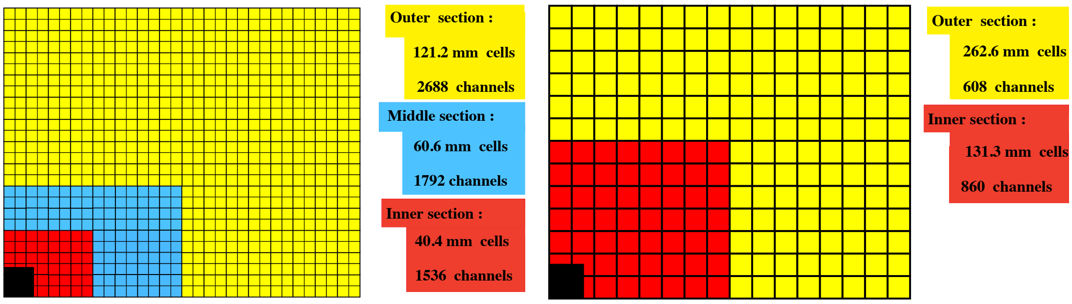

Figure 2.19: The calorimeter lateral segmentation with the SPD, PS and ECAL on the left and HCAL on the right. Only one quarter of the detector front face is displayed [13].

Hit density in the PS, SPD, ECAL and HCAL detectors varies by over two orders of magnitude and therefore they each have variable lateral segmentation, as shown in Fig. 2.19. These calorimeters all work in the same manner; scintillator light is transmitted to a Photo-Multiplier (PMT) by Wavelength-Shifting fibres (WLS), which is then read out. In the SPD and PS system the single WLS fibres are read out with multianode photomultiplier tubes (MAPMT). In the ECAL and HCAL the WLS fibre bunches are read out using individual phototubes.

The ECAL, placed 12 m away from the interaction point, is composed of alternating slices of lead and scintillator material; a design that is known as 'shashlik'. It provides a rapid readout, reliability and radiation resistance but only has a modest energy resolution. The lead slices are 2 mm thick with 4 mm thick scintillator tiles. The ECAL resolution, extracted from fits to test beam data, is given by

$$\frac{\sigma_E}{E} = \frac{10\%}{\sqrt{E}} \oplus 1\% \tag{2.3}$$

where E is in GeV and $\oplus$ means sum in quadrature [13].

The HCAL, situated 13.3 m from the interaction point, is 8.4 m high, 6.8 m wide and 1.65 m deep. It uses a similar design to the ECAL but utilises iron rather than lead. The HCAL has a resolution of

$$\frac{\sigma_E}{E} = \frac{69 \pm 5\%}{\sqrt{E}} \oplus (9 \pm 2)\% \tag{2.4}$$

where E is in GeV [13].

To achieve the expected energy resolution measured in the test environment the components of the calorimeter must be properly calibrated. During 2011 and 2012 the components of the calorimeter system were all calibrated within design requirements [57]. Additionally, effects due to the radiation ageing of the detector must be taken into account. These effects can be compensated for by modifying the photomultipier gains and the calibration constants so that the physics results are unaffected [58].

2.2.5 The Muon System

The muon system [59] [13] provides fast identification of muons and measurement of their p_{T} for use in the trigger. The ability to identify muons cleanly is hugely important for the main physics goals of LHCb, as muons are present in the final states of many B meson decays, which potentially may be sensitive to CP violation and physics beyond the SM. Muons are also very important for the study of quarkonia and are used in this thesis to reconstruct the decay of two J/ψ to four muons.

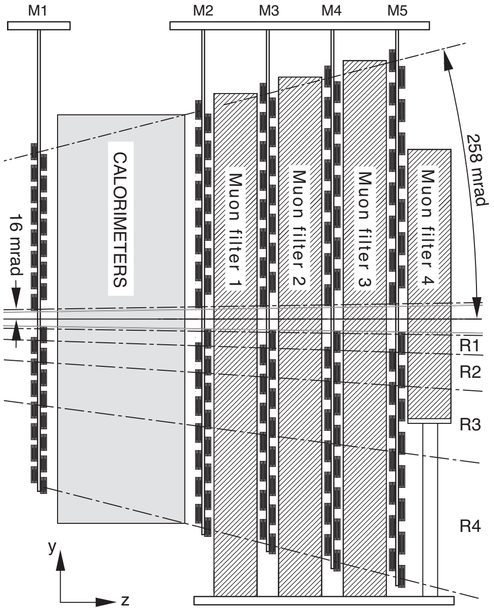

Figure 2.20: The muon system along the y-z plane [13].

The muon system consists of five stations (M1-M5). Station M1 is located just before the calorimeter and stations M2-M5 are the furthest downstream detector elements, as shown in Fig. 2.20. In order to select penetrating muons, 80 cm iron absorbers are placed between stations M2-M5. As such, to cross all five muon stations a muon must have a minimum momentum of about 6 GeV/c.

The muon stations are divided into rectangular 'logical pads' with dimensions being that of the x, y resolution, as shown in Fig. 2.21. The M1-M3 stations have been designed with high spatial resolution in the x coordinate. These stations are used to measure the track direction and calculate the p_T of the muon with resolution of 20%. Additionally M1 is used in the trigger to improve p_T measurement. Stations M4 and M5 have a lower spatial resolution and are used to identify penetrating muons. In order to compensate for the differing particle flux with distance from the beam axis, the detectors are split into four regions R1, R2, R3 and R4, the dimensions of these segments being in the ratio 1:2:4:8, as shown in Fig. 2.21. With this segmentation, the particle flux is approximately equal over the four regions. The transverse dimensions of M1- M5 scale with increasing distance from the interaction point, as displayed in Fig. 2.20.

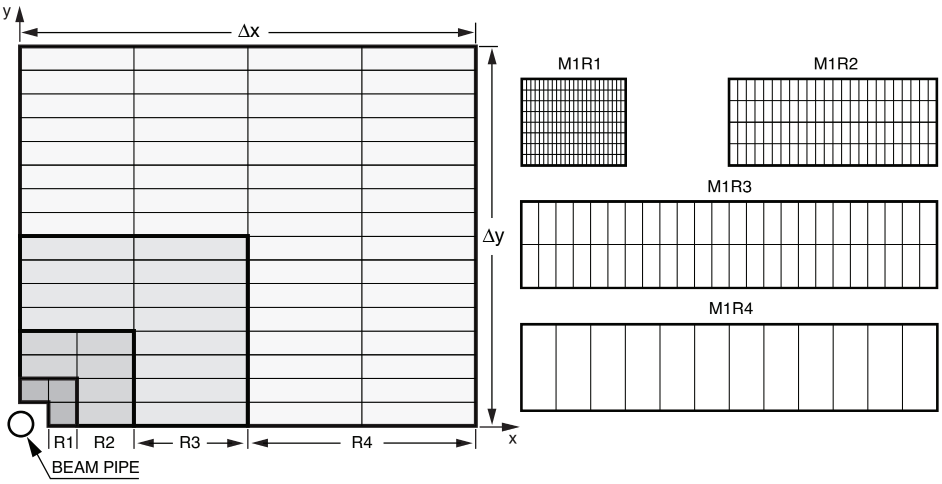

Figure 2.21: Left: Front view of one quadrant of a muon station, with each rectangle representing one chamber. Right: Division into logical pads of four chambers belonging to the four regions of station M1 [13].

The muon system uses Multi Wire Proportional Systems (MWPS) to detect particles in all but the inner section of M1. In this region triple-GEM (Gas Electron Multiplier) detectors are employed, as the particle rate exceeds the safety limits for the ageing of the MWPS detectors. The muon trigger requires aligned hits in each of the five muon detectors within a timescale of less than 25 ns.

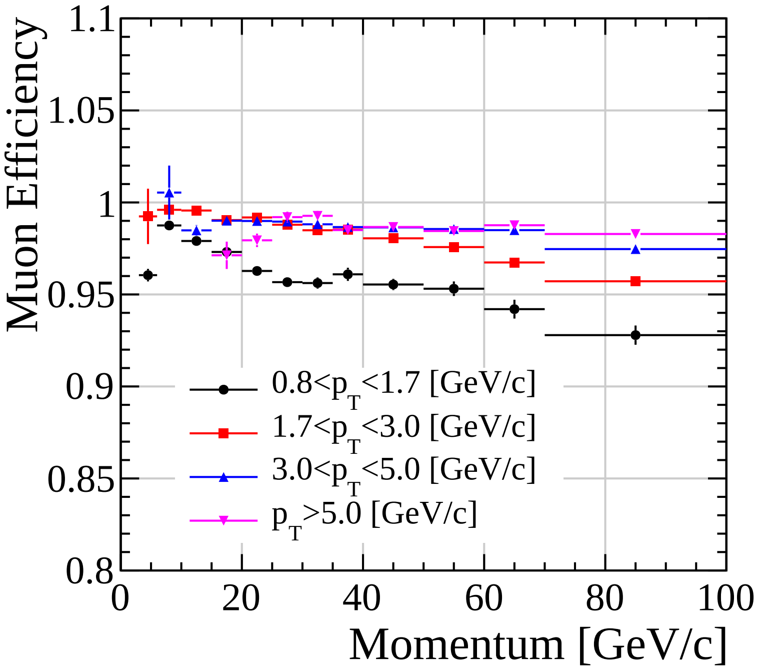

Figure 2.22: The muon efficiency as a function of momentum [60].

The performance of muon identification at LHCb was investigated using 1 fb^{-1} of 2011 data [60]. In Fig. 2.22 the efficiency of finding hits in the muon chambers for tracks extrapolated to the muon system is shown as a function of muon momentum. The average efficiency is 98.13 ± 0.04 % for particles with p greater than 3 GeV/c and p_{T} larger than 0.8 GeV/c. This value is in good agreement with expected values from simulation.

2.2.6 Trigger

The LHCb trigger [13] [61] [62] selects interactions of the most interest so they can be written to storage for further analysis. There are two trigger levels in the LHCb experiment; the Level Zero Trigger (L0) and the High Level Trigger (HLT), which consists of HLT1 and HLT2. Together, the L0 and HLT triggers reduce the rate of visible interactions seen by the LHCb spectrometer from 40 MHz down to 2 kHz.

The L0 trigger reduces the beam crossing rate of 40 MHz to 1 MHz and is implemented in hardware. A L0 Decision Unit (DU) combines information from the pileup system, the calorimeters and the muon chambers to make a decision to accept or reject a bunch crossing.

The pileup system provides an estimate of the number of primary proton-proton interactions in each bunch crossing; if multiple crossings are found then the event is rejected.

The high invariant mass of the B and charm mesons means that the daughter particles generally have high p_{T} and E_{T}. The L0 calorimeter trigger is designed to select high E_{T} hadron, electron and photon clusters, by adding the E_{T} in sets of 2 x 2 cells and selecting those with the highest E_{T}. The muon system provides a rough standalone estimate of the muon p_{T}, with a resolution of the order of 20 %. The L0 muon trigger selects the two muons with the highest p_{T} in each of the muon detector quadrants.

In order to reduce the processing time per event, events which have an excessive multiplicity of tracks are removed, which are identified using the number of hits in the SPD system.

Additionally, events without any visible interactions are removed by requiring a minimum total E_{T} from the HCAL.

HLT1 and HLT2 are implemented in software via a C++ application. Together, the HLT triggers reduce the rate of events to approximately 2 kHz. The HLT has access to the full event data but the system is designed to conserve CPU by rejecting undesirable events without carrying out the full reconstruction.

The events that are selected by the L0 trigger are flagged according to the criteria that selected them; events can belong to the muon, hadron, electron or photon ‘alley’. Approximately 15 % of the L0 events are selected by multiple sources and are therefore assigned to more than one alley. The first part of HLT1 checks the decision made by the L0 trigger, in a process called L0 confirmation. This is carried out by reconstructing the candidate tracks in the VELO and the tracking stations in order to reduce the error on the p_{T}. In the second part of HLT1 additional requirements, for example that tracks have a high p_{T} and impact parameter, reduce the data flow to a rate of approximately 30 kHz.

The rate of events accepted by HLT1 is low enough for HLT2 to use a largely complete track reconstruction to select events using criteria such as the invariant mass and the pointing of momentum towards the primary vertex. Tighter cuts on p_{T} and the impact parameter than previously used are also included. The data are divided into different lines, created using a variety of selection criteria, which are optimised for various LHCb analyses.

The overall trigger data flow is shown in Fig. 2.23.

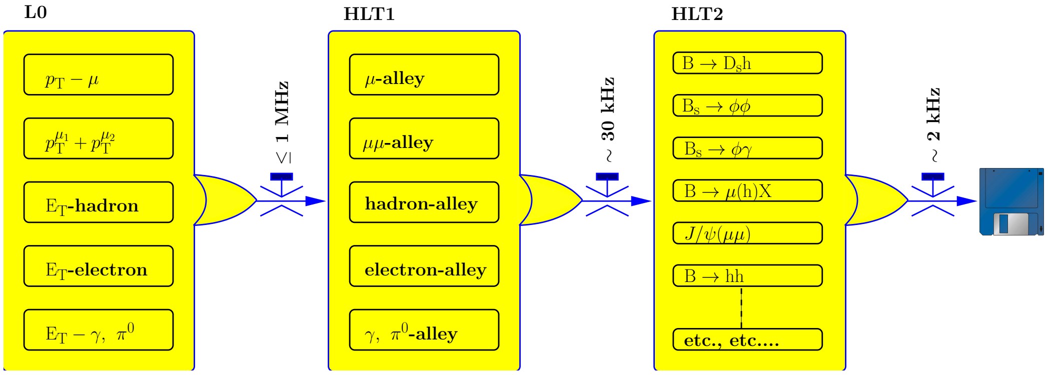

Figure 2.23: Flow diagram of the L0 and HLT trigger sequences [13].

2.2.7 Computing and Software

In order for physics analysis to be performed, the output of the detectors must be reconstructed and the response of the spectrometer simulated. In LHCb these tasks are mostly carried out using the C++ GAUDI [63] [64] [65] framework, of which the main components are GAUSS, BOOLE and BRUNEL.

GAUSS generates particles and simulates their passage through the LHCb detector. Particle generation is carried out with PYTHIA [66], which has been tuned with a specific LHCb configuration. The decays of hadronic particles are described by EVTGEN [67], with the final state radiation generated by PHOTOS [68]. To simulate the interaction of the particles with the detector material and recreate the detector response GEANT4 [69] [70] is used as described in [71].

BOOLE simulates the detector response, including detector imperfections and resolution effects. It also carries out a digitisation process so that simulated data are in the same format as is read out from the experimental sub detectors, although simulation data additionally include the Monte Carlo truth information. After digitisation, MC and data can be treated identically in the trigger, reconstruction and analysis procedures.

Reconstruction of both simulated and experimental data are carried out with Brunel. Analysis is carried out with the DaVinci package, which provides information for event selection, such as kinematic data, decay chains and particle identification.

A schematic view of the Gauss application structure is shown in Fig. 2.24.

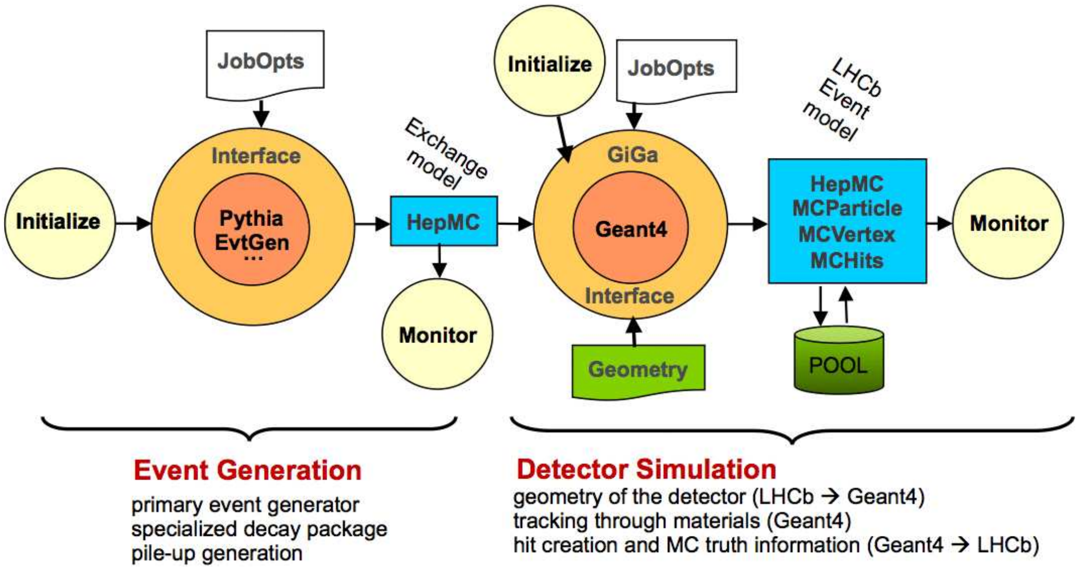

Figure 2.24: Schematic view of the Gauss application structure [65].

Chapter 3

The RICH Alignment System

Ring imaging Cherenkov (RICH) detectors were proposed by J. Seguinot and T. Ypsilantis in 1977 [72] and were first used for particle identification at the E605 experiment at Fermilab in 1981 [73]. They have since been employed at a number of experiments, including HERAb [74] and DELPHI [75]. At LHCb, particle identification is carried out with two such detectors, RICH1 and RICH2.

3.1 RICH Resolution

The LHCb RICH detectors combine the measurement of the Cherenkov angle with an estimate of the momentum from the tracking system in order to determine a particle's identity. The ability to separate particle species is dependant upon the angular resolution of the detector, as is shown below.

In the limit of small Cherenkov angles and for large momentum ($p \gg m$), Eqn. 2.2, describing the relation between the Cherenkov angle, the refractive index of the radiative material and the ratio of the velocity of the particle to that of the speed of light in a vacuum becomes

$$1 - \frac{\theta_c^2}{2} \approx \frac{1}{n}\left(1 + \frac{m^2}{2p^2}\right) \tag{3.1}$$

For two charged particles with the same momentum but different masses, the difference of the square of their Cherenkov angles is given by

$$\theta_2^2 - \theta_1^2 = -\frac{1}{n}\frac{\Delta(m^2)}{p^2} \tag{3.2}$$

where $\Delta(m^2)$ is the difference in the masses of the two particles. Substituting in $\Delta\theta_C \;=\; \theta_2 - \theta_1$

$$\Delta\theta_C \cdot (\theta_2 + \theta_1) = -\frac{1}{n}\frac{\Delta(m^2)}{p^2} \tag{3.3}$$

The maximum value the Cherenkov angle can take for a given refractive index of n is when $\beta = 1$ and therefore Eqn. 2.1 simplifies to

$$cos(\theta^{max}) = \frac{1}{n}. \tag{3.4}$$

When the value of the refractive index is close to 1, i.e. $(n-1) \ll 1$, then Eqn. 3.4 can be approximated using a Taylor expansion to

$$\theta^{max} \approx \sqrt{2(1-\frac{1}{n})}. \tag{3.5}$$

Assuming that θ_1 and θ_2 can be approximated by θ^{max} and therefore substituting Eqn. 3.5 into Eqn. 3.2 we get

$$\Delta\theta_C = -\frac{1}{2n\sqrt{2(n^2-1)}}\frac{\Delta(m^2)}{p^2} \tag{3.6}$$

If the Cherenkov angles follow a Gaussian distribution of width σ_θ, then the number of sigma, n_σ, separating two charged particles of the same momentum but different mass is simply given by

$$n_\sigma = \frac{\Delta\theta_C}{\sigma_\theta} = -\frac{1}{2n\sigma_\theta\sqrt{2(n^2-1)}}\frac{\Delta(m^2)}{p^2} \tag{3.7}$$

This equation makes clear that the particle identification performance is dependant upon the resolution of the Cherenkov angle.

The Cherenkov resolution in the LHCb RICH detector is dominated by four sources of uncertainty [53]:

Table 3.1: Sources of Cherenkov angular uncertainty for each of the three RICH radiators [53].

	$\sigma(\theta_C)(mrad)$		
	Aerogel	C_4F_{10}	CF_4
Emission point	0.4	0.8	0.2
Chromatic dispersion	2.1	0.9	0.5
Pixel size	0.5	0.6	0.2
Tracking	0.4	0.4	0.4
Total	2.6	1.5	0.7

- **Emission point:** When a track traverses a radiative material in the RICH detectors, photons are emitted uniformly along its length. As the emission point of a photon is unknown, the Cherenkov angle is reconstructed assuming that the photon originated from the midpoint of the particle track through the medium. The error in the emission point coupled with the tilted geometry of the spherical mirrors causes the reconstructed Cherenkov angle to differ from the true value, which leads to a smearing of the Cherenkov angle.
- **Chromatic dispersion:** The refractive index of the radiator has a dependence upon the wavelength of the Cherenkov photons. As the wavelength of the photons is unknown, the uncertainty in the refractive index leads to an uncertainty in the Cherenkov angle.
- **Pixel size:** The finite size of the HPD pixels places a limit on the resolution.
- **Tracking:** The Cherenkov angle is measured with respect to tracks, therefore, uncertainty in the track position results in an associated uncertainty in the Cherenkov angle.

The magnitude of these sources of angular uncertainty are listed in Table. 3.1.

3.2 RICH Alignment and Calibration

The performance of the RICH detector depends strongly upon it being properly aligned and calibrated, such that the associated errors are small compared to the errors listed in the previous section.

A number of components are required to be aligned with an accuracy of 0.1 mrad with respect to the tracking system. A sequential process is utilised, starting with aligning the entire RICH detector with the global LHCb coordinates, followed by each detector half, every mirror segment and ending with the alignment of the individual HPD detectors [54]. Misalignment of the RICH detectors with respect to the tracking results in a shift of the track from the centre of the corresponding Cherenkov ring. In addition, a number of components need to be calibrated or monitored:

- **HPD calibration:** The HPD detectors are sensitive to stray magnetic fields from the LHCb magnet. Although the HPD units are encased in magnetic shielding, residual magnetic fields exist of up to 2.4 mT in RICH1 and 0.6 mT in RICH2 [54].

  RICH1 and RICH2 have separate systems in order to calibrate the magnetic field, although both employ a similar method. RICH1 has a dedicated calibration system, the Magnetic Distortion Calibration System (MDCS), which produces a reproducible pattern of light spots in order to illuminate the HPD array, which can be compared with the magnet on and off. As the magnetic field is generally longitudinal with respect to the axis of the tube, it tends to cause a rotation and slight increase in size of the image. RICH2 employes a similar technique using a commercial light projector. Using these methods the distortion due to the magnetic field is reduced so that it is smaller than the irreducible uncertainty due to the finite pixel size [13].

  In addition, the magnetic field strength inside the HPD can change on the timescale of hours, therefore additional corrections are calculated. This is carried out for each HPD using a procedure which fits a circle to the HPD image.

- **Refractive index calibration:** The refractive index of the gas radiators has a dependence upon the ambient temperature and pressure, which requires corrections be applied on the timescale of hours. High momentum charged particle tracks are used to calculate the difference between the expected and measured

Cherenkov angle, the distribution of which peaks at zero for an aligned system. The refractive index of the aerogel does not change as a function of time [54].

Additionally, the purity of the gas radiators is monitored by measuring the speed of sound in the gas. The purity is also periodically checked with the aid of a gas chromatograph [13].

- **Mirror alignment:** The individual mirror segments that make up the primary and secondary mirrors of RICH1 and RICH2 are aligned to the tracking system. The mirror alignment procedure is detailed in the next section.

  Additionally, a selection of mirror segments in RICH1 and RICH2 are monitored for stability using a laser beam and cameras, which detects movement of reference mirrors [13].

3.3 RICH Mirror Alignment Procedure

In the RICH detectors, Cherenkov radiation is focused onto HPD detectors, which lie outside of the LHCb acceptance, using a combination of spherical ‘primary’ mirrors and flat ‘secondary’ mirrors. Due to their large size, the primary and secondary mirror planes are subdivided into a number of smaller segments, with RICH1 consisting of 4 primary and 16 secondary mirrors, and RICH2 having 56 primary and 40 secondary mirrors. The mirrors are classified, depending on which side of the beam pipe they lie, into ‘left-hand side’ and ‘right-hand side’ mirrors. The division and numbering of the RICH2 mirrors are shown in Fig. 3.1.

A change in alignment of the RICH mirrors results in a shift of the Cherenkov photons in the HPD plane as shown in Fig. 3.2. However, the reconstructed extrapolated position of the associated track on the HPD plane will not change. This results in a displacement of the track from the centre of the associated Cherenkov ring.

The RICH mirror alignment procedure is carried out with collision data, using a method based on that developed by the HERAb experiment [74]. A misaligned mirror can be discerned by analysing the difference between the measured Cherenkov angle, θ_C, and

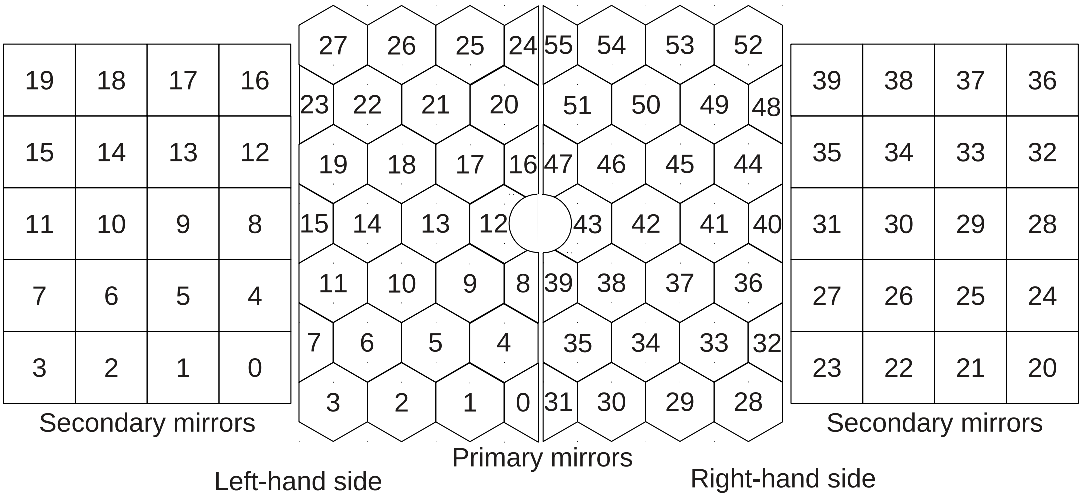

Figure 3.1: The RICH2 mirror segmentation and numbering schema, viewed in x, y plane with the beampipe at the centre [76].

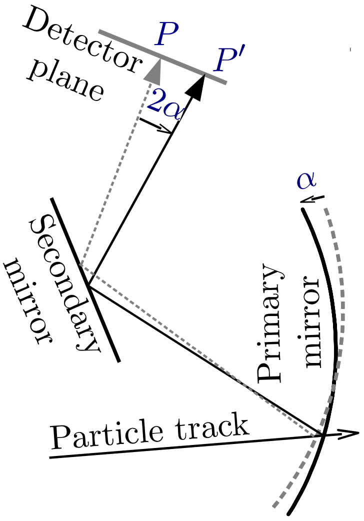

Figure 3.2: Schematic illustration of the effect of a misaligned mirror segment. A small tilt of the primary mirror causes a shift of the Cherenkov photons on the HPD plane [76].

the expected Cherenkov angle for an aligned system, θ_0, as a function of the azimuthal angle, ϕ, around the ring. This difference can be written as

$$\Delta\theta = \theta_C - \theta_0 \tag{3.8}$$

In a misaligned system $\Delta\theta$ will have a dependence on ϕ, as shown in Fig. 3.3(a), whereas in an aligned system there will be no dependence, as in Fig. 3.3(b).

The mirror alignment is carried out with high momentum tracks. At high momentum the Cherenkov angles of the different particles tends to the same value, as shown in Fig. 2.13,

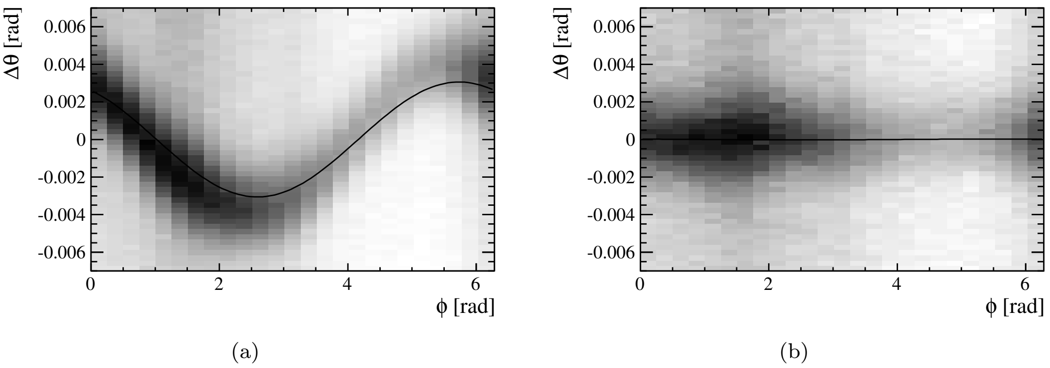

(a)

(b)

Figure 3.3: $\Delta\theta$ vs. ϕ for a mirror pair in the RICH1 detector (a) before alignment (b) after alignment [76].

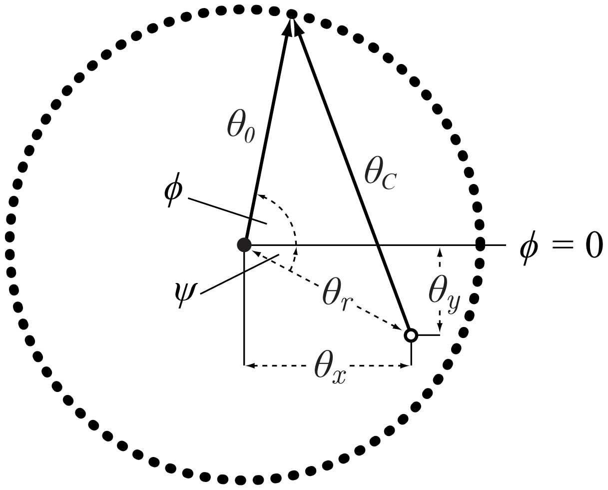

Figure 3.4: Schematic illustration of Cherenkov ring misalignment, with the misalignment exaggerated for illustrative purposes.The actual Cherenkov ring centre is displaced by a distance θ_r from the reconstructed track trajectory, which is shown as an empty circle. The reconstructed Cherenkov angle is shown by θ_C and the expected Cherenkov angle is θ_0. The horizontal and vertical displacements are given by θ_x and θ_y. [77].

and the particles are said to be ‘saturated’. All particles can then be approximated as pions, and the mass can be assumed to be that of a pion. In RICH2 a minimum momentum of 40 GeV is used for alignment.

The horizontal and vertical components of the translation between the expected ring centre and misaligned, θ_x and θ_y as shown in Fig. 3.4, can be related to $\Delta\phi$. The relationship between θ_C, θ_0 and the displacement of the ring centre with respect to the track, θ_r is derived, following the example in Ref. [77], firstly using the cosine rule

$$\theta_C^2 = \theta_0^2 + \theta_r^2 - 2\theta_0\theta_r\cos(\phi + \psi) \tag{3.9}$$

where ψ is the angle of the right handed triangle that is formed by the displacement components of θ_x and θ_y. Adding in Eqn. 3.8 the expression becomes

$$(\theta_0 + \Delta\theta)^2 = \theta_0^2 + \theta_r^2 - 2\theta_0\theta_r \cos(\phi + \psi) \tag{3.10}$$

which can be rearranged to

$$\Delta\theta + \frac{1}{2\theta_0}(\Delta\theta^2 - \theta_r^2) = -\theta_r \cos(\phi + \psi) \tag{3.11}$$

Expanding the cosine of the summed angles leads to

$$\Delta\theta + \frac{1}{2\theta_0}(\Delta\theta^2 - \theta_r^2) = -\theta_r(\cos\phi\cos\psi - \sin\phi\sin\psi) \tag{3.12}$$

which, using trigonometric relations for $\sin\phi$ and $\cos\phi$, becomes

$$\Delta\theta + \frac{1}{2\theta_0}(\Delta\theta^2 - \theta_r^2) = \theta_y \sin\phi - \theta_x \cos\phi \tag{3.13}$$

This can be approximated for small misalignments to

$$\Delta\theta = \theta_y \sin\phi - \theta_x \cos\phi. \tag{3.14}$$

where θ_x and θ_y represent the combined tilts of the primary and secondary mirrors in the x and y direction. They therefore incorporate factors that relate the displacement of the Cherenkov rings to actual physical mirror tilts, called ‘magnification coefficients’. The individual mirror tilts in the y direction are given by

$$l_{tot}\theta_y \approx l_{pri}2\alpha_y - l_{sec}2\beta_y \tag{3.15}$$

where l_{tot} is the total path of the photons to the photodetectors, l_{pri} is the total length from the primary mirror and l_{sec} is the length from the secondary mirror and α_y and β_y represent the tilt in the y direction of the primary and secondary mirrors respectively. The factor 2 arises, as a rotation of a mirror by an angle θ results in a deflection of the mirrors by 2θ in the HPD plane, as shown in Fig. 3.2. Rearranging Eqn. 3.15 gives

$$\theta_y \approx \frac{l_{pri}}{l_{tot}} 2\alpha_y - \frac{l_{sec}}{l_{tot}} 2\beta_y \approx A_y \alpha_y + B_y \beta_y \tag{3.16}$$

where A_y and B_y are the magnification coefficients in the y direction. Similarly, the tilts in the x direction are given by

$$\theta_x \approx \frac{l_{pri}}{l_{tot}} 2\alpha_x + \frac{l_{sec}}{l_{tot}} 2\beta_x \approx A_x \alpha_x + B_x \beta_x \tag{3.17}$$

In RICH2, in order to calculate the misalignment of the individual mirrors, a system of equations of primary and secondary 'mirror pairs' is used. The pairs are chosen so that each secondary mirror is paired with at least two primary mirrors, such that all the mirrors are linked together on each side of the beam pipe. One primary mirror is fixed in position on the left hand side (primary mirror 12, as shown in Fig. 3.1) and right hand side (primary 43) of the mirrors, which allows the misalignment of the associated secondary mirror to be found with respect to the fixed mirror. In turn, the now aligned secondary mirror's position is fixed to enable the next primary mirror in the chain to be aligned. This process is repeated until all mirrors have been aligned. The system and sequence of mirror pairs for the left hand side mirrors is illustrated in Fig. 3.5. The mirror pairs chosen are from the strongest pair populations in each primary mirror.

For each mirror pair, the distribution of $\Delta\theta$ versus ϕ is plotted in 20 bins of ϕ. Inside each of the 20 bins, the $\Delta\theta$ distribution is fitted with a Gaussian for the signal, and the background is fitted with a second order polynomial, in order to extract the peak value of $\Delta\theta$, as shown in Fig. 3.6. The peak value of $\Delta\theta$ for each of the 20 bins in ϕ is plotted and is fitted with an equation of the form of Eqn. 3.16, as is shown in Fig. 3.3(a), in order to extract the misalignment coefficients.

As it is not known where along a track's path in the radiator a photon is emitted, it is assumed all photons are emitted at the path's midpoint. In order to reduce the background in the alignment, only photons where the reconstruction results in it being reflected by the same primary and secondary mirror pair regardless of where it was emitted along the track, are used. Such photons are known as 'unambiguous' photons.

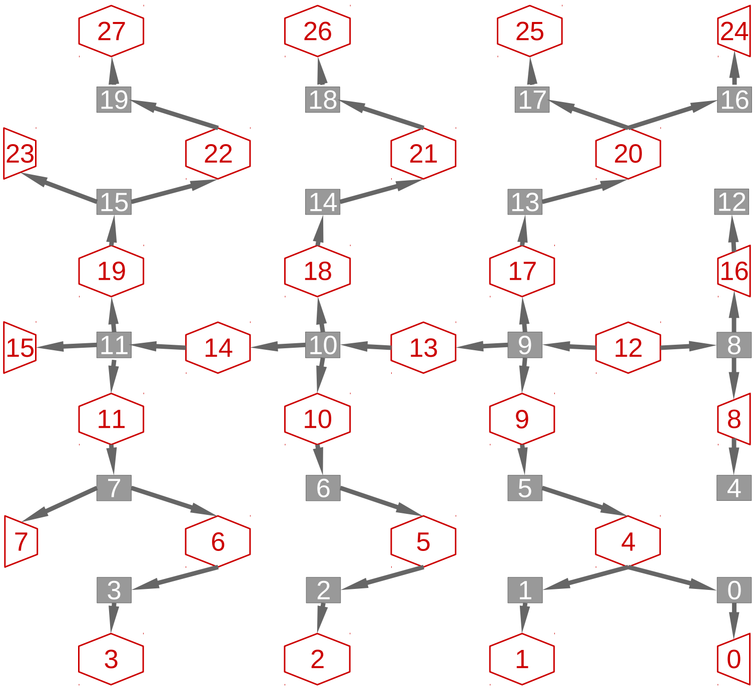

Figure 3.5: Schematic diagram illustrating the system of equations linking all primary mirrors (red hexagon and half-hexagon) and secondary mirrors (grey squares) on the left hand side of the beam pipe, with numbering corresponding to Fig 3.1. Arrows indicate the sequence in which the misalignments are solved, starting from the fixed primary mirror 12 [76].

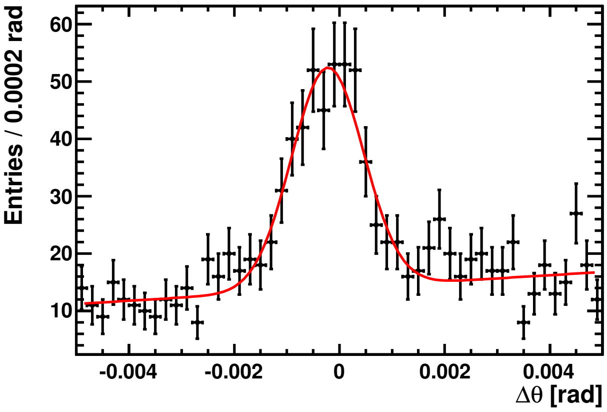

Figure 3.6: $\Delta\theta$ distribution in ϕ bin between 162° and 180° for RICH2, fitted with a Gaussian for the signal and a second order polynomial for the background [78].

Conversely, ‘ambiguous’ photons are those where the mirror pair changes depending on where it was emitted along the track.

The alignment is an iterative process because the magnification coefficients are slightly altered after the mirrors are adjusted. Therefore, the same data are re-reconstructed with the results of the previous alignment incorporated and the distributions of $\Delta\theta$

versus ϕ are fitted again in order to extract new alignment parameters. The process is repeated until the remaining misalignments are less than 0.1 mrad.

The number of Cherenkov photons required to adequately fill the $\Delta\theta$ vs ϕ plot for all of the RICH2 mirror pairs is approximately 500 thousand. However, in order to achieve these populations it is necessary to reconstruct approximately 5 million events [76]. The main reasons for the high number of events that need reconstructing are

- **Particle density:** The density of particles in the LHCb detector is very much higher towards the beam pipe, as is shown in Fig. 3.7, therefore it is difficult to fill the lower populated 'outer' mirror pairs.
- **Non-uniform ϕ distribution:** Tests show that for the $\Delta\theta$ versus ϕ plots to converge, at least 16 of the 20 bins in ϕ require at least 300 photons [76]. The ϕ distribution can be very non-uniform and therefore it can be difficult to sufficiently populate the required number of ϕ bins.
- **Ambiguous photons:** Data samples used for alignment are composed of approximately 25 % ambiguous photons, which cannot be used.
- **Mirror pairs:** Photons that do not reflect off the selected mirror pairs can not be used for alignment.

3.4 RICH2 HLT Track Pre-selection

The LHC will restart after Long Shutdown 1 (LS1) in 2015. After LS1, HLT1 and HLT2 will be decoupled and events will be temporarily buffered after they are accepted by HLT1 [79]. Whilst the events are buffered, the detector alignment and calibration will be performed and this information will be used when data are processed at HLT2. This will allow the HLT2 selections to be tightened, which will increase the purity of the data written to disk for analysis.

The RICH2 mirror alignment procedure uses a significant amount of CPU time, due to the large amount of data that needs to be reconstructed. The changes to the structure

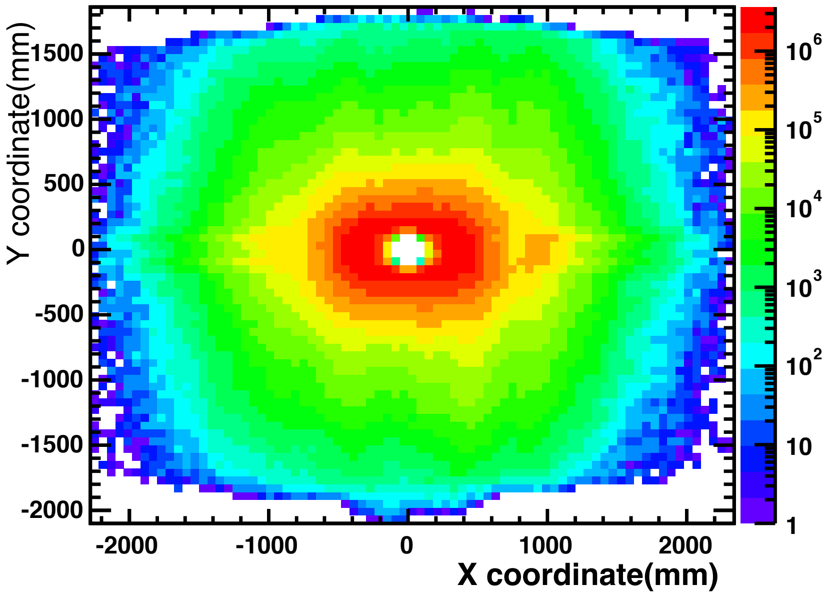

Figure 3.7: Photon hits in the x, y coordinates in the z plane of the RICH2 primary mirror, with the beampipe at the origin, units in mm.

of the HLT necessitate that the RICH2 mirror alignment procedure is sped up, due to the limited time that the data can be buffered.

It was proposed that suitable alignment data for each mirror pair could be pre-selected in HLT2 using only the track position in the plane of the RICH2 primary mirror (as RICH photons are not reconstructed in HLT2). This process requires that within every primary mirror 'sub-areas' are found such that the tracks, and therefore the associated Cherenkov photons, reflect primarily on a specific secondary mirror.

Two considerations suggest that it may be possible to select such sub-areas. Firstly, in RICH2, each primary mirror reflects on only a limited number of secondary mirrors, as is shown in Fig. 3.8. Secondly, Cherenkov rings are mostly reflected by only one primary mirror; the probability for a Cherenkov ring being imaged by only one primary mirror segment is

$$p_{1mirr} \approx 1 - \frac{r_C}{r_m} \approx 78\% \tag{3.18}$$

where r_m is the radius of a circle of circumference 251 mm, which can inscribe the hexagonal mirror segments and r_C is the maximum base radius of the Cherenkov cones, which is 55 mm [80].

HLT pre-selection could significantly reduce the amount of data that is reconstructed for the mirror alignment. Additionally, as the selection only depends on the HLT track information, it should not be a large additional CPU overhead on the HLT processing. Reducing the number of events to be reconstructed, from $\sim$ 5 million to 50 thousand, means the HLT pre-selection could speed up the RICH2 alignment by approximately two orders of magnitude.

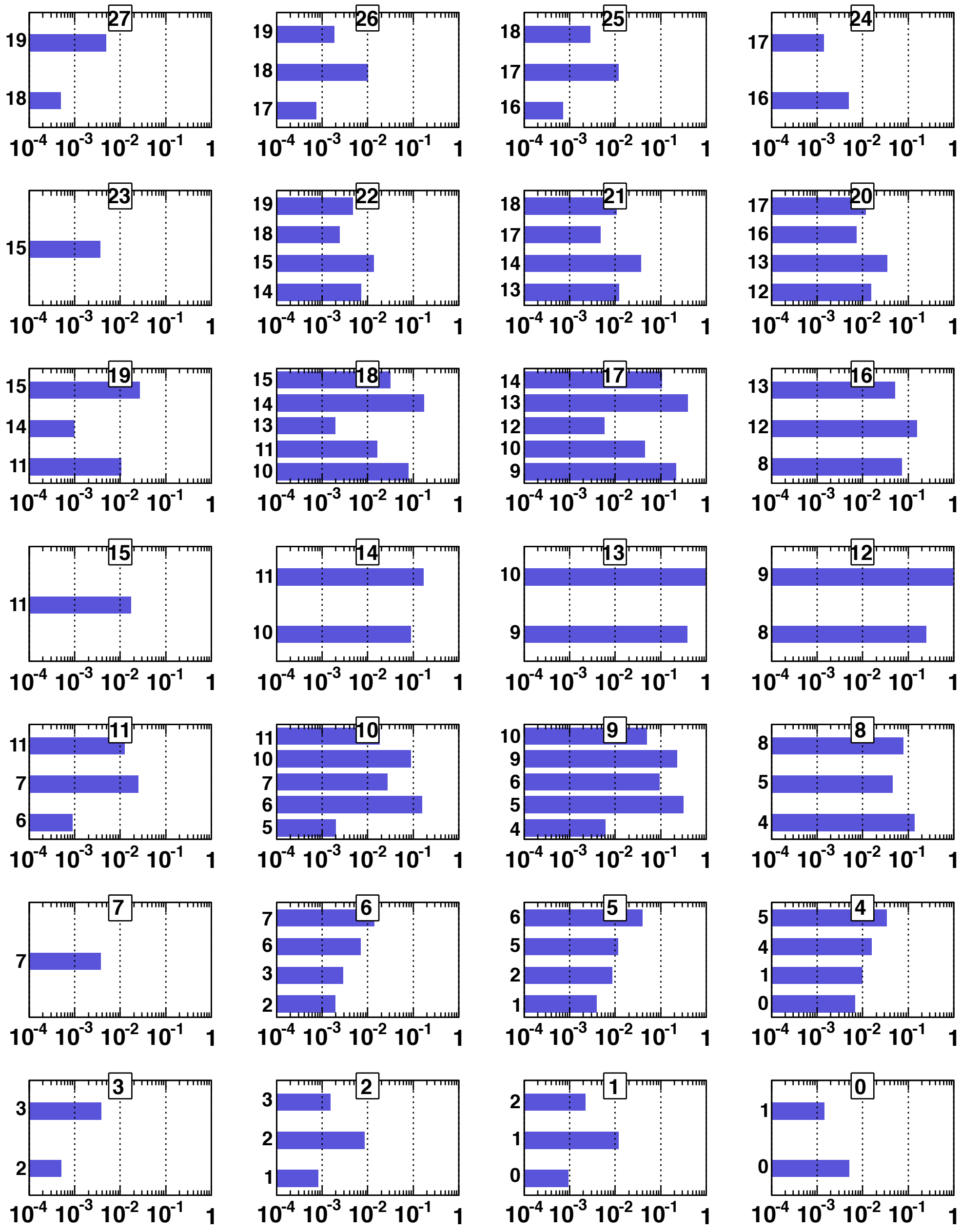

Figure 3.8: Strongest population of mirror pairs in the left hand of the RICH2, normalised to the largest population. Histogram titles show the primary mirror number, and the y-axis label show the secondary mirror number [78]

3.5 HLT Track Pre-selection

The aim of the HLT track pre-selection is to minimise the amount of data that needs to be reconstructed to run the RICH2 mirror alignment. However, the data required to populate the pre-selection cannot exceed the data available in the period over which the alignment is to be run, which for the RICH mirrors is approximately 5 hours [81] and is termed a ‘fill’.

In order to select suitable sub-areas of each primary mirror, the efficiency of reconstructing suitable photons from tracks over each primary mirror was investigated. Using this ‘reconstruction’ efficiency, sub-areas with the highest efficiency were selected that could populate the mirror alignment with the data available from a fill.

Tests were carried out using data from the 2012 ‘min bias’ line, which best replicates the minimal selections on the data in HLT2. Near-saturated tracks, with a minimum momentum of 40 GeV, were used, in line with the requirements for alignment.

The feasibility of the pre-selection is studied in Sec. 3.6 and two separate methods of obtaining suitable sub-areas are examined in Sec. 3.7 and Sec. 3.8

3.6 Test Reconstruction Efficiency

As a test of the viability of the HLT pre-selection, an exercise was carried out using only unambiguous RICH2 photons to examine if sub-areas exist within each primary mirror where the Cherenkov photons reflect only onto a particular secondary mirror.

For each mirror pair the reconstruction efficiency was calculated as

$$\epsilon_{\gamma}^{reco} = \frac{N_{\gamma}^{pair}}{N_{\gamma}^{primary}} \tag{3.19}$$

where N_{γ}^{pair} is the number of photons reflecting only on the relevant mirror pair and $N_{\gamma}^{primary}$ is the number of photons that reflect on the relevant primary mirror and onto any secondary mirror. An ansatz binning of size 30 mm in the x and y direction was used.

An example reconstruction efficiency for mirror pair primary mirror 12 and secondary mirror 9 (p12s9) is shown in Fig. 3.9. The right hand side of the mirror has an efficiency of ~ 1, which means that this region is hit by photons which then have a strong probability to be reflected by secondary mirror 9. This suggests that it may be possible to choose a sub-area of this primary mirror that could then be used to select tracks that have p12s9 photons.

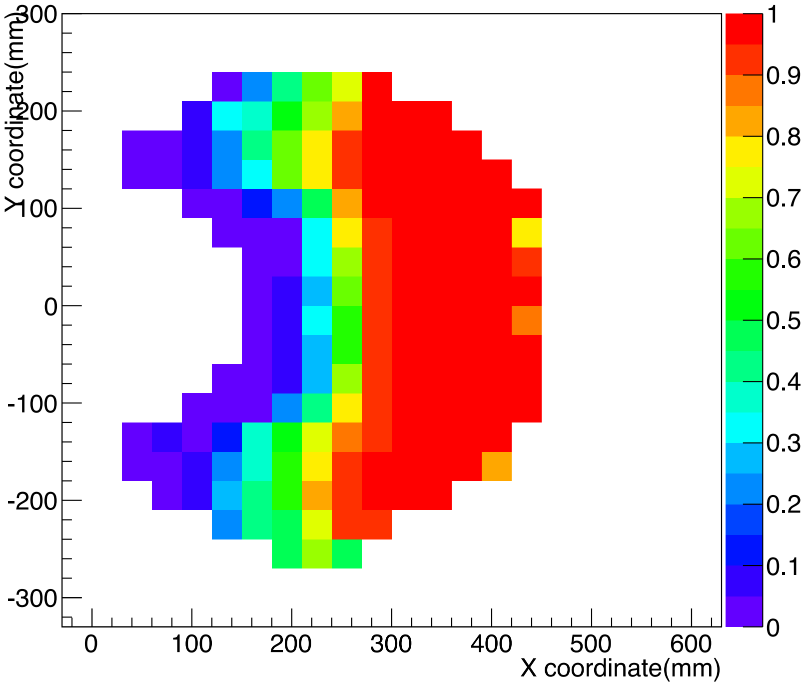

Figure 3.9: Efficiency for photons reflected off primary mirror 12 and secondary mirror 9 as a function of the x, y co-ordinates of primary mirror 12. The beam pipe is at the origin.

3.7 Track Reconstruction Efficiency

The test exercise in the previous section was carried out using photons without using track information. However, in order to pre-select suitable tracks by their position, the relationship between the photons and the tracks must be examined.

The amount of data to be reconstructed by the pre-selection will be minimised if all the associated Cherenkov photons from a selected track are suitable for alignment. Additionally, this will lead to the pre-selected photons having an approximately uniform ϕ distribution. This means the 20 ϕ bins used in the alignment will approximately be uniformly filled, which will also minimise the amount of data to be reconstructed. Therefore, for each mirror pair the ‘track reconstruction’ efficiency was calculated as

$$\epsilon^{reco} = \frac{N^{pair}}{N^{primary}} \tag{3.20}$$

where N^{pair} is the number of tracks where all of the associated photons are classed as ‘unambiguous’ and reflect from a particular mirror pair and $N^{primary}$ is the total number of tracks that reflect off the relevant primary mirror. An ansatz binning of size 30 mm in the x and y direction was used.

The reconstruction efficiency for p12s9 can be seen in Fig. 3.10(a); regions in the right hand side of this mirror pair have an efficiency greater than 0.8. However, approximately half of all the mirror pairs had an efficiency ≈ 0, as is shown for p17s9 in Fig. 3.10(b).

Although only 25 % of photons are ambiguous and are largely distributed along the edges of the mirrors, as can be seen in Fig. 3.11(a), tests show that approximately 84 % of tracks have at least one ambiguous photon, with the position of such tracks distributed over a much larger area, as displayed in Fig. 3.11(b). Additionally, approximately 84 % of tracks have photons that reflect on more than one primary or secondary mirror. Overall, 90 % of tracks have at least one ambiguous-photon or one photon that reflects off more than one primary or secondary mirror, which would therefore be excluded from contributing to N^{pair}, leading to low efficiencies.

As such, the requirement that all of the Cherenkov photons are unambiguous and are reflected off the same mirror pair is not suitable to be used as a selection criteria for at least half of the mirrors. An alternative method is examined in the next section.

3.8 ϕ Weighted Reconstruction Efficiency

In the previous section, entire tracks were assigned to either the numerator and/or denominator of the efficiency. As this method was found to be unsuitable, the ‘ϕ weighted’ reconstruction efficiency was calculated by considering individual photons, rather than whole tracks. However, as the desired aim is to pre-select data by track position, the

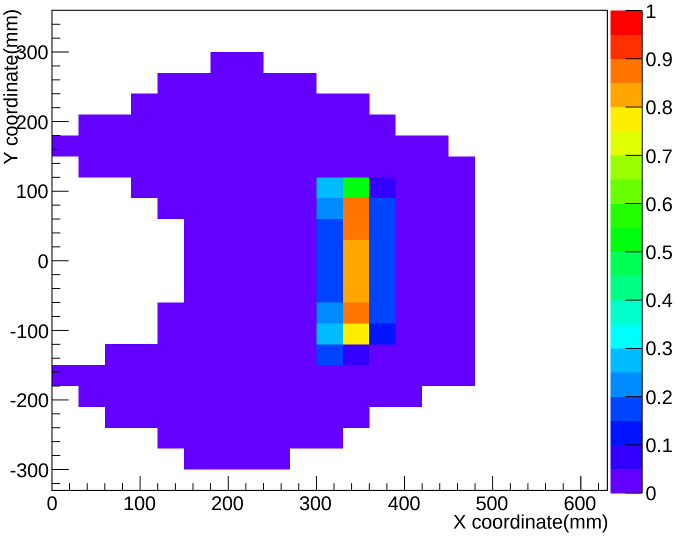

(a)

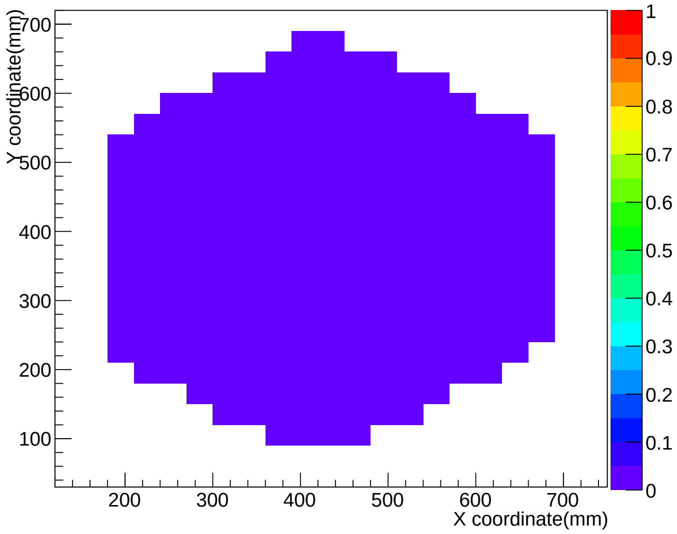

(b)

Figure 3.10: Efficiency for tracks where all photons reflected off (a) primary mirror 12 and Sec 9 and (b) primary mirror 17 and Sec 9, as a function of the x, y co-ordinates in the plane of the primary mirror. The beam pipe is at the origin.

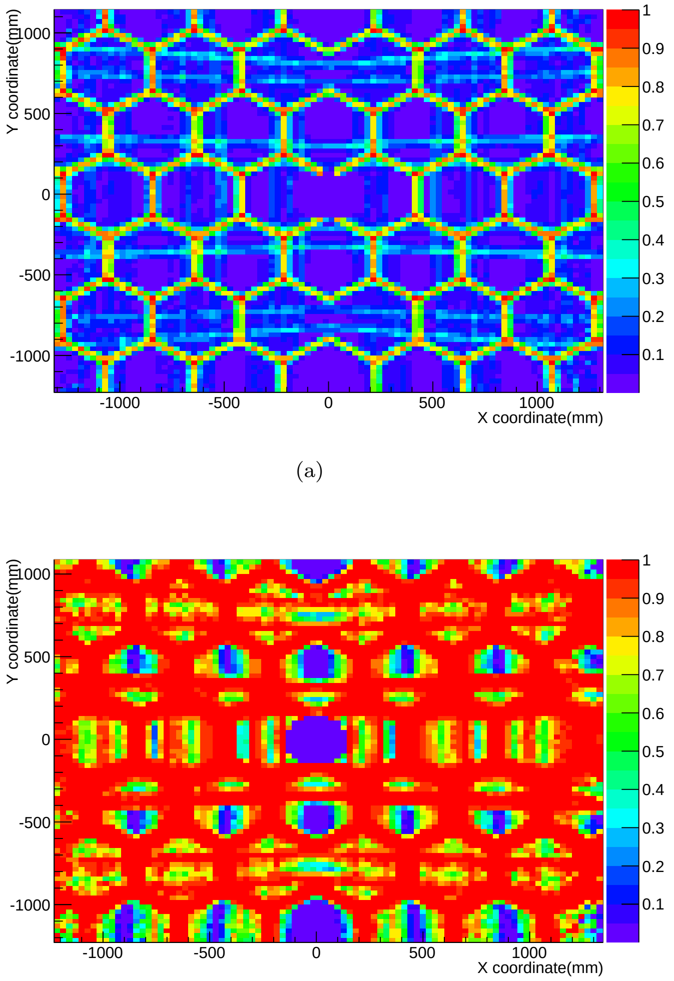

(a)

(b)

Figure 3.11: Efficiency for (a) unambiguous photons (b) tracks containing at least one unambiguous photon, as a function of the x, y co-ordinates in the plane of the primary mirror. The beam pipe is at the origin.

track position in the primary mirror plane was used in place of the photon position in the calculation of the efficiency.

Tests showed that sub-areas with non-uniform ϕ distributions can require orders of magnitude more data to be reconstructed in order to populate at least 16 of the 20 bins in ϕ sufficiently. Therefore, the reconstruction efficiency was weighted by a factor, W_ϕ, which accounts for how much extra data must be reconstructed due to the non-uniform ϕ distribution. The reconstruction efficiency was therefore calculated as

$$\epsilon_\phi^{reco} = \frac{N_\phi^{pair}}{N_\phi^{primary}} \times W_\phi \tag{3.21}$$

Table 3.2: Example mirror pairs, showing the reconstruction efficiency, the selected sub-areas' x and y co-ordinates in the plane of the RICH2 primary mirrors in mm and the number of events required to pass through the RICH2 to find the requisite data to carry out the alignment for that mirror pair ('Events required').

Mirror pair	ϵ_{ϕ}^{reco}	X_{start}	X_{end}	Y_{start}	Y_{end}	Events required
p12s9	0.71	330	360	-100	100	3800
p17s9	0.18	400	425	136	221	295831
p12s8	0.5	125	150	115	117	140000
p16s12	0.59	50	150	388	424	63000
p20s12	0.47	92	138	626	662	970000
p24s16	0.71	50	75	840	870	4200000

where N_{ϕ}^{pair} is the number of unambiguous photons that reflect on a particular mirror pair and $N_{\phi}^{primary}$ is the total number of photons that reflect off the relevant primary mirror, including ambiguous photons.

In order to select sub-areas of optimum position and dimension a 'variable binning' procedure was used on the ϕ weighted efficiency. This process calculated the reconstruction efficiency, varying the bin size from a minimum in x or y of 25 mm up to a maximum of 250 mm, in steps of 5 mm. The minimum bin size was chosen so that bins were sufficiently populated, even in the low occupancy mirrors. The highest efficiency bin out of all possible combinations was selected, provided that the selected area could populate the mirror alignment with the data available from a fill.

The ϕ weighted efficiency distribution with the binning containing the highest efficiency bin (shown in red) for mirror pair p12s9 is shown in Fig. 3.12. As displayed in Table. 3.2, the selected sub-area was of size 30 mm in the x direction and 200 mm in the y direction. The reconstruction efficiency for this sub area is 0.71, which means that for tracks selected because they pass though this area, approximately 70 % of the associated photons are suitable for alignment of p12s9. For this mirror pair, the number of events required to pass through the entire RICH2 detector in order to populate 16 out of 20 ϕ bins, with at least 300 photons via this sub-area is approximately 3800 (termed 'events required'). The corresponding ϕ weighted efficiency for p17s9 can be seen in Fig. 3.13, with details also displayed in Table. 3.2. Information about further example mirror pair sub-areas are displayed in Table. 3.2, with all mirror pairs shown in Appendix A.

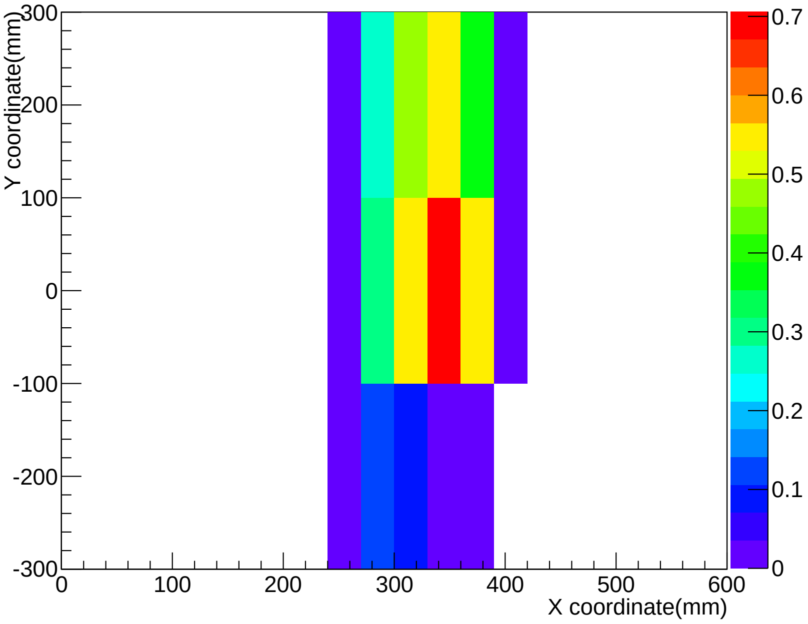

Figure 3.12: Phi weighted efficiency for p12s9 as a function of the x,y co-ordinates of primary mirror 12. The beam pipe is at the origin.

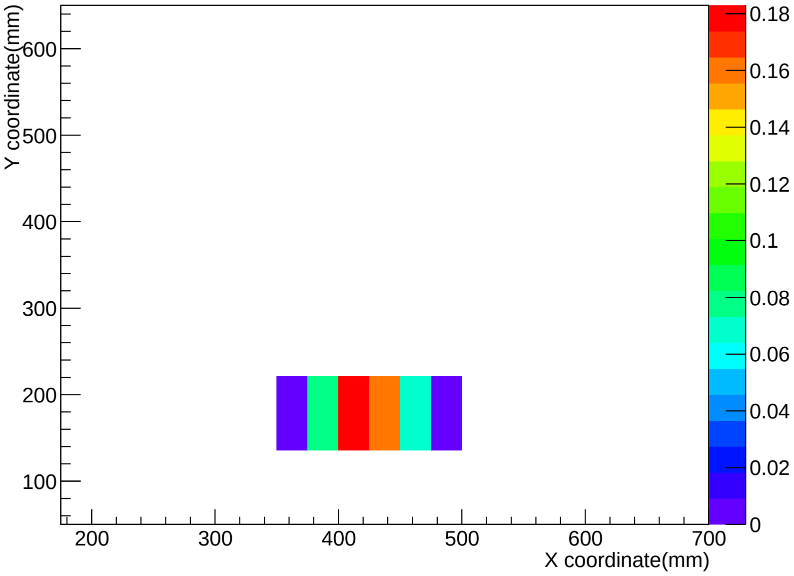

Figure 3.13: Phi weighted efficiency for p17s9 as a function of the x,y co-ordinates of primary mirror 12. The beam pipe is at the origin.

3.9 Conclusions

A procedure to pre-select data by utilising track position, for use in the RICH2 mirror alignment, has been developed. It will be used in the HLT2 to pre-select tracks to evenly populate the mirror pairs that are used for alignment of the RICH2 mirrors, reducing greatly the amount of data that must be reconstructed. This will allow the RICH mirror alignment to be carried out in a timely manner whilst the collision data are temporarily buffered on disk and will also save CPU resources.

The average ϕ weighted reconstruction efficiency using this procedure is ~ 50 %. To populate the RICH2 alignment requires a minimum of ~ 550 thousand photons, or approximately 10 thousand appropriate tracks and associated photons. Using the selection procedure only 20 thousand tracks and associated photons will need to be reconstructed. This potentially represents a reduction in the amount of data that needs to be reconstructed of around two orders of magnitude.

Work is ongoing to turn the selection criteria into a HLT2 line.

Chapter 4

Double J/ψ Production

This chapter will present the analysis of double J/ψ production, reconstructed from $J/\psi \to \mu^+\mu^-$ decays. Possible muon tracks are first identified and are selected by the LHCb trigger. Stripping lines reconstruct muon vertices and apply loose selection criteria. Further selection criteria are applied to the dataset, in order to more fully separate signal from background. A yield of signal double J/ψ events is extracted from fitting an appropriate distribution to the invariant mass distribution of the double J/ψ pair. Efficiencies are calculated, in order to correct for events lost in the collection and selection of the dataset. An sPlot technique [82] is utilised, which uses the invariant mass fit of the double J/ψ pair, to give a statistical weight to each of the signal candidates for it to be signal. This statistical weight is then divided by the efficiency for each candidate, in order to obtain a weighted yield of events. This method of obtaining a corrected yield can be sensitive to background, particularly in low efficiency areas of phase space, therefore the selection criteria and stripping lines are chosen so as to minimise background noise. The cross-section is calculated using the weighted yield, the measured luminosity of the sample and the branching fraction of J/ψ to $\mu^+\mu^-$. Finally, the differential cross-sections as a function of various kinematic quantities are calculated and compared to theoretical predictions.

Table 4.1: The muon stations with hits in the FOI required for the IsMuon decision as a function of muon momentum range [60].

Track momentum range GeV/c	Muon Station
$3 < p < 6$	M2 + M3
$6 < p < 10$	M2 + M3 + (M4.or.M5)
$p > 10$	M2 + M3 + M4 + M5

4.1 Muon Identification

In this study, J/ψ particles are reconstructed from their decay to two oppositely charged muons. As described in Sec. 1.2, the J/ψ particle has a relatively high di-lepton branching ratio, which is of the same order as the hadronic. The decay to muons is utilised as it is the most cleanly identifiable; unlike hadrons or even electrons, muons can penetrate through the entire spectrometer into dedicated muon detectors, which can determine precisely the charge, momentum and direction and thus allow the narrow J/ψ resonance to be precisely reconstructed.

In order to identify muons in the LHCb detector, the muon finding procedure [60] [83] is carried out on 'long' or 'downstream' tracks (as defined in Sec. 2.2.1.3). Such tracks are extrapolated linearly to the muon detector and a field of interest (FOI) is built around the extrapolated position. The FOI's size depends on the momentum of the track, the muon station and region within the station where the hits are found. Hits in the muon station are searched for in the FOI and the information is used to calculate the muon candidate condition, IsMuon. The number of hits required in different stations for this variable are a function of the track p_{T}; hits in the FOI of stations M2 and M3 are required for tracks with $3 < p < 6$ GeV/c, in the FOI for three stations out of M2, M3, M4, M5 for tracks with $6 < p < 10\,\mathrm{GeV}/c$, and in the stations M2 - M5 for $p_{\mathrm{T}} > 10$ GeV/c, as summarised in Table. 4.1. The IsMuon condition removes non-muons down to the level of approximately 4 %.

4.2 Trigger

As described in Sect. 2.2.6, the LHCb trigger selects interactions of the most interest so they can be written to storage for further analysis. The trigger requirements can change over the course of data taking, with different conditions identified by a Trigger Configuration Key (TCK). Datasets are further subdivided depending on the polarity of the magnet during data taking, into positive polarity (Magnet Up) and negative polarity (Magnet Down). Small datasets ($<5\ \mathrm{pb}^{-1}$) were not used in this study, in order to reduce variation in data taking conditions. The TCK lines used in this analysis are presented in Table 4.2. A scaling factor, which rejects 80 % of the events with $p_{\mathrm{T}} < 2$ GeV, was applied at HLT level to approximately two thirds of the dataset (TCK 0x760037, 0x790038, 0x790037).

Two L0 trigger lines were used to select events for this analysis; a dedicated muon line (**L0Muon**) and di-muon line (**L0DiMuon**), which both select only tracks that have hits in the muon stations. High p_{T} tracks are required, as such tracks come predominately from high mass resonances such as the J/ψ; the **L0Muon** line requires one muon candidate with a p_{T} greater than 1.5 GeV/c, and the **L0DiMuon** line requires that the product of the two muon's p_{T} must be larger than 1.3 GeV^2/c^2 [61].

The HLT1 lines used in this study comprise the **Hlt1SingleMuon**, **Hlt1DiMuon** and **Hlt1MuTrack** lines. The HLT1 lines require that the relevant L0 lines were fired and that there are either one (SingleMuon and MuTrack) or two (DiMuon) well reconstructed tracks that have hits in the muon system. The SingleMuon and MuTrack triggers exploit the p_{T}, impact parameter and track quality to separate signal from background. The DiMuon triggers use the mass of the di-muon candidates and the separation of the di-muon vertex, as well as the track quality, p_{T} and total momentum [84].

The HLT2 lines utilised consist of the **Hlt2SingleMuon**, **Hlt2DiMuon**, **Hlt2MuTrack**, **Hlt2DoubleDiMuon** and **Hlt2ExpressJpsi**. These lines confirm the HLT1 decision with a higher precision. A number of muon HLT trigger lines that had a high scaling

Table 4.2: List of TCK used in the measurement of the double J/ψ cross-section.

TCK	Polarity	Lumi pb^{-1}
0x5A0032	Down	28.3 ± 1.0
0x5A0032	Up	33.0 ± 1.2
0x6D0032	Down	96.5 ± 3.4
0x730035	Down	58.0 ± 2.0
0x730035	Up	129.0 ± 4.5
0x760037	Down	186.8 ± 6.5
0x760037	Up	102.9 ± 3.6
0x790038	Down	203.7 ± 7.1
0x790038	Up	121.6 ± 4.3
0x790037	Up	37.7 ± 1.3

factor that accepts less than 1 % of events, which could potentially give rise to excessively large re-weighting of individual events, were excluded. These lines consisted of **Hlt1SingleMuonNoIP**, **Hlt2DiMuonDY1** and **Hlt2DiMuon**.

To remove very high multiplicity events, which would take excessively long to reconstruct, Global Event Cuts (GEC) were applied after the L0 trigger during data taking. The main GEC requirement for lines used in this study is a selection on the number of hits in the SPD detector, known as the 'SPD multiplicity'. The **L0Muon** excludes events with a SPD multiplicity above 600, the **L0Dimuon** excludes events with a SPD multiplicity above 900.

4.3 Data

The data used in this report consist of 998 ± 35 pb^{-1} of *pp* collisions, collected during 2011 by the LHCb experiment at a centre of mass energy of $\sqrt{s} = 7$ TeV. The dataset was selected using the **DiMuonDiMuonInc** stripping line. This line reconstructs muon vertices from two oppositely charged muons, using BRUNEL v43r2p3, and applies a number of loose selections using DAVINCI v32r2p3 (Reco14 Stripping20r1).

In the reconstruction, a selection is made in order to remove tracks that share information, known as clone tracks, which are created when the LHCb software reconstructs more than one track from a single particle. If tracks share hits in the tracking system,

Table 4.3: Summary of selection criteria carried out in the reconstruction and DimuonDimuon stripping line.

Selection Criterion
$\Delta_{KL}^{min} > 5000$
IsMuon = true
$3\ \mathrm{GeV}/c^2 < Mass_{J/\psi}$
${p_\mathrm{T}}^{\mu} > 650\ \mathrm{MeV}/c$
$\chi^2_{tr}/nDoF < 3.0$
$\chi^2_{VX} < 20$

they may be removed by a pattern recognition algorithm, with the lower quality track being excluded [85]. However, clone tracks do not necessarily share hits in the tracking stations; for example, clone tracks can be created when the algorithm splits up VELO tracks into hits from the forward stations and hits from the remaining stations [86]. Such clone tracks will, however, have similarities post reconstruction; for example the momentum will be approximately the same. Therefore, clones can be excluded using the Kullback-Liebling divergence, KL^{min}, which measures the difference in information between two tracks [86]. Only tracks with a divergence greater than 5000 are selected. The tracks must also pass the IsMuon requirement. Two oppositely charged tracks that pass these requirements are fitted into a *J/ψ* vertex. Good quality muon tracks and *J/ψ* vertexes are obtained using a selection criteria of $\chi^2_{tr}/nDoF < 3$ and $\chi^2_{VX} < 20$, respectively, where χ^2_{tr} is the reduced χ^2 from the track fit and χ^2_{VX} is the reduced χ^2 of the *J/ψ* vertex. The mass of the dimuon pairs must be at least 3 GeV/c^2, and each muon must have a p_T greater than 650 MeV/c. The reconstruction and **DiMuonDiMuonInc** line selection criteria are summarised in Table. 4.3.

4.3.1 Luminosity Measurement

The LHCb experiment uses two methods to measure luminosity; the 'Van der Meer scan' method (VDM) and the 'Beam Gas Imaging' method (BGI) [87].

The VDM method utilises the LHC's ability to move the beams with high precision to measure the number of visible *pp* interactions as a function of the position offsets of the two colliding beams, in order to directly determine the effective cross-section.

Due to the fact the beam is bunched it must be scanned in both transverse directions. The measurement depends on the assumption that the density distributions in the two transverse directions can be factorised.

The BGI method employs the high resolution of the VELO subdetector and the close proximity of the detector to the beam to directly measure vertices from beam-beam collisions and from the interactions of beam particles with residual gas in the machine, which consist mainly of relatively light elements such as hydrogen, carbon and oxygen. The distribution of these vertices allows the transverse bunch profile to be determined.

In combination, the two techniques allow the luminosity to be measured with an error of 3.5 % over the data taking period used in this analysis [87].

4.3.2 Monte Carlo Samples

In this study three Monte Carlo (MC) samples were utilised, generated with Gauss v45r3 [65]. The Gauss simulation software uses Pythia 6.427 [66] to produce *pp* collisions using a NRQCD framework that includes CS and CO components, and the EvtGen v13r6 [67] package to generate the subsequent decays. Events were generated separately for Magnet Up and Magnet Down polarities, assuming that the J/ψ is unpolarised. The three MC samples are

- A J/ψ to $\mu^+\mu^-$ sample, with both the J/ψ and its daughter muons inside a cone of opening angle 400 mrad ('daughters in acceptance'). The J/ψ includes prompt J/ψ, produced directly in the *pp* interaction or from feed down from charomonia, and non-prompt J/ψ, produced from B-hadrons and Upsilon. It was generated to reflect the running conditions carried out in 2011, using $\sqrt{s} = 7$ TeV with an average number of interactions per beam crossing, ν, of 2.5. The sample consisted of ~ 20 M events, evenly split between the Magnet Up and Down polarities. This MC was used to calculate the reconstruction efficiency.
- A J/ψ generator level sample, generated with identical parameters as the above sample, but without the daughters in acceptance requirement. This sample is used

to calculate a correction factor associated with the J/ψ being inside the acceptance but the decay products being produced outside, not allowing the decay chain to be reconstructed.

- A double J/ψ to $\mu^+\mu^-$ sample. It was generated using the LO CS model to also reflect the running conditions carried out in 2011. The sample consisted of ~ 2 M events, split between the Magnet Up and Down polarities. This MC was used to calculate the efficiency of selection criteria involving J/ψ pairs, and also to cross-check factorisation when using single J/ψ MC.

4.4 Fiducial Volume

The LHCb detector covers a rapidity range between 2 and 5. However, in the region of rapidity near the beam pipe the J/ψ are poorly reconstructed, and a correct measurement of the reconstruction efficiency and associated errors is difficult. Therefore, the fiducial volume was reduced to a rapidity between 2 and 4.2. The fiducial region was also reduced to only measure J/ψ with a p_{T} between 0 and 10 GeV/c, due to the limited number of events with a p_{T} greater than this value.

4.5 Event Selection

In order to separate signal from background, a number of selection criteria were applied to the dataset. The selection criteria were initially optimised to maximise the statistical significance on a single J/ψ data sample of 1 M events, collected with a TCK of 0x5A0032, as outlined in Appendix B. However, the sPlot efficiency weighted procedure used to calculate a corrected yield in this study was sensitive to background, especially in areas of phase space where the efficiency is low. Therefore, instead of using selection criteria that optimised the statistical significance, the selection criteria were selected to reduce background.

Dimuon pairs with a mass between 3.0 and 3.2 GeV/c^2, were initially selected. To ensure that well identified muons were obtained, a neural network variable, P_{NNMu} [88], trained to differentiate between real and background muons, was utilised. A selection of $\mathrm{P}_{NNMu} > 0.5$ was made on this variable, which combines information from the muon system, the RICH and calorimeter systems. The requirement on the quality of the tracks was increased from the loose selection used in the **DiMuonDiMuonInc** stripping line of $\chi^2_{tr}/nDoF < 3.0$, to $\chi^2_{tr}/nDoF < 1.7$. A selection was made on the pseudorapidity, η, of the muons requiring them to be in the range $2 < \eta < 5.0$, in order to remove poorly measured tracks in the outer reaches of the detector.

Due to the high track densities in the LHCb detector, fake tracks can also be reconstructed from a pseudorandom combination of hits; such tracks are called ghost tracks [89]. In order to remove ghost tracks, a selection is made by a neural network trained to differentiate between real and fake tracks [88]. A requirement of $\mathrm{P}_{ghost} < 0.05$ is made on the output of this neural network, which uses information from the tracking and particle identification systems and outputs the probability that the track is a ghost.

Muons with a momentum below 5 GeV/c and a momentum above 200 GeV are removed, due to the track reconstruction efficiency, which measures the probability that a charged particle that passes through the full tracking system is reconstructed, being poorly measured outside these regions [90]. In order to remove a region with a significant amount of background, muons with a momentum below 6 GeV/c were additionally removed.

Candidate muon pairs that survive all selections are combined to create double muon pairs, $(\mu^+\mu^-)_1(\mu^+\mu^-)_2$, which are required to originate from a common vertex that is compatible with one of the reconstructed primary vertices. To carry out this constraint, the vertex of the four muons and each of the two muon vertices is globally refitted using a ‘decay tree fitter’ (DTF) with a ‘primary vertex constraint’ [91]. The DTF is an alternative method to reconstruct a decay chain of an event; usually, decay chains are started by fitting the vertices from the final state particles with the information being propagated ‘upstream’ towards the primary interaction. The DTF takes a complete decay chain, parameterises it in terms of vertex positions, momentum parameters and decay lengths and refits these parameters simultaneously using a least squares method, taking into account all the relative constraints. To exclude events that do not come

Table 4.4: Summary of selection criteria.

Selection Criterion
$3.0 < Mass_{J/\psi} < 3.2$ GeV/c^2
$2 < \eta_\mu < 5.0$
$p^\mu > 6$ GeV/c
$\chi^2_{tr}/nDoF < 1.7$
$\mathrm{P}_{NNMu} > 0.5$
$\mathrm{P}_{ghost} < 0.05$
$6 < \mathrm{p}_\mu < 200$ GeV/c
$\chi^2_{DTF-J/\psi}/nDoF < 11.0$
$\chi^2_{DTF-2\times J/\psi}/nDoF < 5$

from the primary pp collision, such as $B \to J/\psi$ events, a selection was made on the two muon vertex of each J/ψ of $\chi^2_{DTF-J/\psi}/nDoF \ < \ 11.0$. This selection relies on the long lifetime of the B mesons, which means non-prompt J/ψ are produced a significant distance from the primary production vertex. To exclude J/ψ candidates from different pp collisions, a similar selection was also made on the quality of the DTF four muon vertex $\chi^2_{DTF-2\times J/\psi}/nDoF \ < \ 5$.

The selection criteria are summarised in table 4.4.

4.6 Signal Yield

In order to extract the yield of double J/ψ events, a two dimensional unbinned extended maximum likelihood fit to the J/ψ invariant mass has been used. The di-muon pairs are randomly classified as either J/ψ_1 or J/ψ_2 and fitted accordingly. A double sided Crystal Ball (DCB) function is used to model the signal, which is defined as

$$f^{J/\psi}_{CB}(x) = \begin{cases} e^{-\frac{1}{2}\alpha_L^2}\left(\frac{n_L}{n_L-\alpha_L^2-|\alpha_L|\delta_\sigma x}\right)^{n_L} & \delta_\sigma x < -|\alpha_L| \\ e^{-\frac{1}{2}\delta_\sigma x} & -\alpha_L < \delta_\alpha x < |\alpha_R| \\ e^{-\frac{1}{2}\alpha_R^2}\left(\frac{n_R}{n_R-\alpha_R^2+|\alpha_R|\delta_\sigma X}\right)^{n_R} & \delta_\sigma x > |\alpha_R| \end{cases} \tag{4.1}$$

where $\delta_\sigma x = \frac{x-m_0^{J/\psi}}{\sigma^{J/\psi}}$, $m_0^{J/\psi}$ is the peak value of the invariant mass distribution, $\sigma^{J/\psi}$ is the standard deviation of the distribution and α_L, n_L and α_R, n_R are the parameters of the left and right tail, respectively. The left tail component $\delta_\sigma x < -|\alpha_L|$ models the bremsstrahlung emission. The right tail $\delta_\sigma x > |\alpha_R|$ has been added to describe the non-Gaussian tail in the distribution. Combinatorial background is modelled by an exponential function.

The line shape was initially studied and parametrized using a Monte Carlo sample of ∼20 M single *J/ψ* events. A DCB function was used to fit the signal and an exponential function used for the combinatorial background. The parameters $\alpha_L = 1.7$, $\alpha_R = 1.85$, $\mathrm{n}_L = 2.7$, $\mathrm{n}_R = 3.0$ were initially fixed to values determined as optimum from a MC study in Ref. [10]. The mass and width of the *J/ψ* peak were left free, as they depend on the kinematic range of the *J/ψ* mesons due to material effects in the detector. Optimisation of the quality of the line fit, as characterised by the χ^2, did not give a subsequent improvement in the quality of the fit on data. The line shape was also studied on a data sample of 1 M single *J/ψ* events. New optimum fit parameters of $\alpha_L = 1.42$, $\alpha_R = 1.74$, $\mathrm{n}_L = 3.0$, $\mathrm{n}_R = 4.67$ ('Optimum') were extracted. However, these also did not improve the quality of the fit on the double *J/ψ* sample; therefore the values of $\alpha_L = 1.7$, $\alpha_R = 1.85$, $\mathrm{n}_L = 2.7$, $\mathrm{n}_R = 3.0$ from Ref. [10] were used in this study.

Alternative fit models to the DCB were also studied. A single Crystal Ball (CB) function was tested

$$f(M_{\mu\mu}) = \begin{cases} e^{\left(-\frac{M_{(\mu\mu}-\mu)^2}{2\sigma^2}\right)} & \text{for } \frac{M_{\mu}\mu-\mu}{\sigma} > -a \\ A \cdot \left(B - \frac{M_{\mu\mu}-\mu}{\sigma}\right)^{-n} & \text{for } \frac{M_{\mu}\mu-\mu}{\sigma} < -a \end{cases} \tag{4.2}$$

where

$$A = \left(\frac{n}{|a|}\right)^n \cdot e^{\left(-\frac{|a|^2}{2}\right)} \tag{4.3}$$

$$B = \frac{n}{|a|} - |a| \tag{4.4}$$

with n=1 and α as a function of σ, $\alpha = 1.975 + 0.01\ \sigma$ - $0.00018\sigma^2$, as used in Ref. [92]. Additionally, the 'Hypatia' [93] function was also tested, an altered CB shape that takes into account the fact the per event mass error is not constant. This function has a new core for the CB, that corresponds to a Gaussian with a variance having the shape of the per event mass error squared. The alternative fit shapes failed to improve the quality of the fit compared to the DCB.

The muons from each event in the data were combined in all viable opposite charge combinations to create two J/ψ. After all selection criteria were applied to the data, 21 double J/ψ events had two viable combinations of muons that were mutually exclusive. The signal yield including all 'multiple candidate' events was 1816 ± 52, with a background of 878 ± 24; removing one of the pairs of multiple candidate events at random gave a signal yield of 1811 ± 50, with a background of 867 ± 24. The 21 multiple candidate events were all left in the final selection, and the small difference in resulting cross-section between the two choices was assigned as a systematic uncertainty. The choice was made to keep all multiple candidates, as removing one of the combinations at random meant that on average half of the multiple candidate 'real' events may be replaced with 'false', background, events, whereas keeping all combinations kept the 'real' events but added events that may be fitted as background events.

The projection of the two dimensional invariant mass distributions with both J/ψ events in the fiducial range and at least one of the muons explicitly selected by the trigger lines outlined in Sec. 4.7.4 are displayed in Fig. 4.1(a) and Fig. 4.1(b).

4.7 Efficiency

The total efficiency for double J/ψ production, ϵ^{tot}, can be factorised into

$$\epsilon^{tot} = \epsilon^{reco} \times \epsilon^{geo} \times \epsilon^{\mu ID} \times \epsilon^{trg} \tag{4.5}$$

where ϵ^{reco} is the efficiency due to the reconstruction and selection of the J/ψ, ϵ^{geo} is the geometric acceptance efficiency, which accounts for events where the J/ψ are outside the acceptance but they can be reconstructed from di-muon pairs that are not, $\epsilon^{\mu ID}$ is the efficiency of the muon identification variable, P_{NNMu} and ϵ^{trg} is the efficiency of the selection of the J/ψ by the trigger.

The total efficiency, ϵ^{tot}, is used to calculate a weighted yield of events, which accounts for inefficiencies in the detection and reconstruction of the double di-muon pairs, where

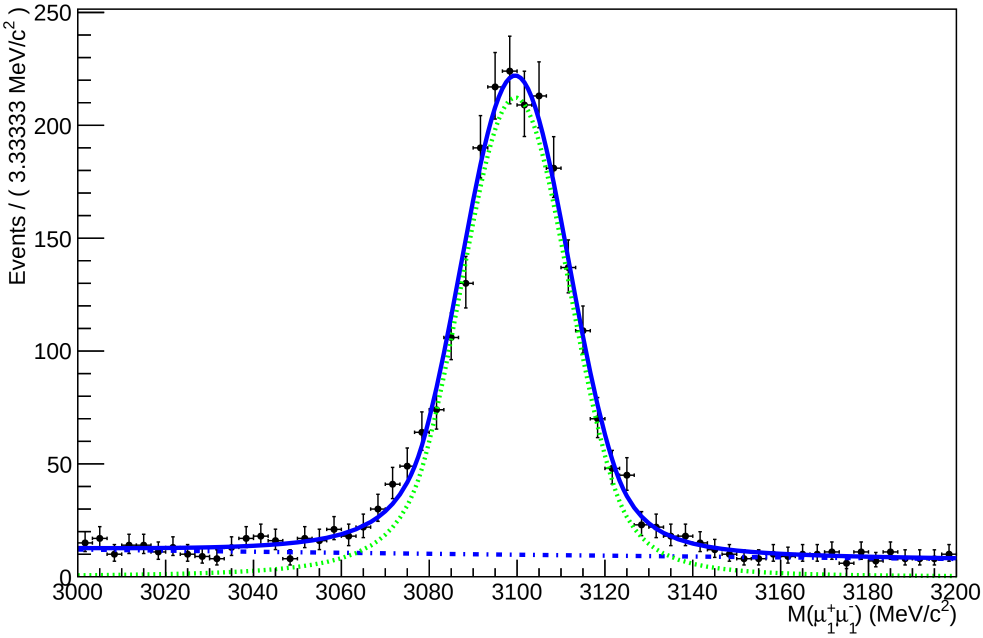

(a) J/ψ_1

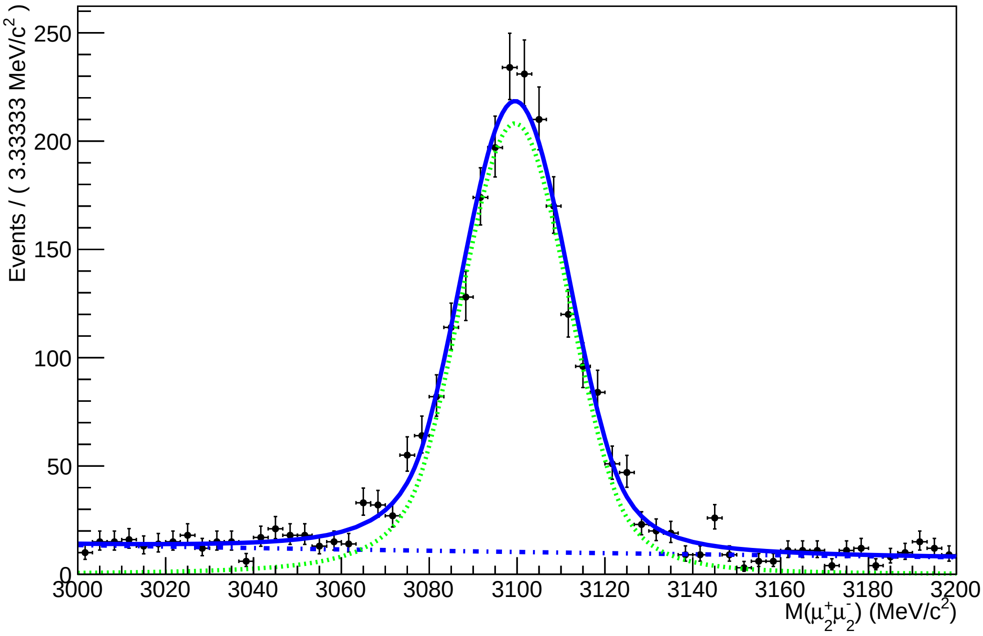

(b) J/ψ_2

Figure 4.1: Projection of two dimensional invariant mass distribution with a double sided Crystal Ball function for the signal and an exponential function for the background. The number of signal J/ψ is shown with the dotted green line, the background is shown with the dotted blue line, with the total shown with the solid blue line.

the weighting factor is given by

$$w^{-1} = \epsilon^{tot}. \tag{4.6}$$

4.7.1 Reconstruction and Selection Efficiency

The loss of efficiency due to the requirements that both J/ψ are reconstructed and selected, ϵ^{rec}, was evaluated on a single J/ψ MC sample using the factorisation

$$\epsilon^{reco} = \epsilon^{reco}_{J/\psi_1} \times \epsilon^{reco}_{J/\psi_2}. \tag{4.7}$$

The validity of this factorisation was verified with a double J/ψ MC sample, which was used to check that the total unbinned reconstruction and selection efficiency was consistent between the two methods. The reconstruction and selection efficiency for a single J/ψ was evaluated with

$$\epsilon^{reco}_{J/\psi} = \frac{N^{acc}_{J/\psi}}{N^{tot}_{J/\psi}} \tag{4.8}$$

where $N^{acc}_{J/\psi}$ is the number of events that remain after the reconstruction and selection criteria are applied and $N^{tot}_{J/\psi}$ is the number of events initially. The muon identification variable, P_{NNMu}, and the selection of four muons into the same primary vertex, $\chi^2_{DTF-2\times J/\psi}/nDoF < 5$ were not applied in the evaluation of $\epsilon^{reco}_{J/\psi}$.

To account for differences between the data and MC, which can cause significant variations in the efficiency, the MC was re-weighted with respect to the data for the p_{T}, rapidity and the number of tracks in each event ('best track multiplicity'). In order to extract normalised distributions, the **DimuonDimuonInc** stripping line selections were applied to both the data and the MC. In order to remove background from data, an sPlot technique [82] was employed, which used the invariant mass distribution fitted with a DCB function for the signal and an exponential function for the background. The normalised p_{T} and rapidity distributions can be seen in Fig. 4.2 and Fig. 4.3, for a TCK of 0x5A0032.

The track reconstruction efficiency, which measures the probability that a charged particle that passes through the full tracking system is reconstructed, is known to differ

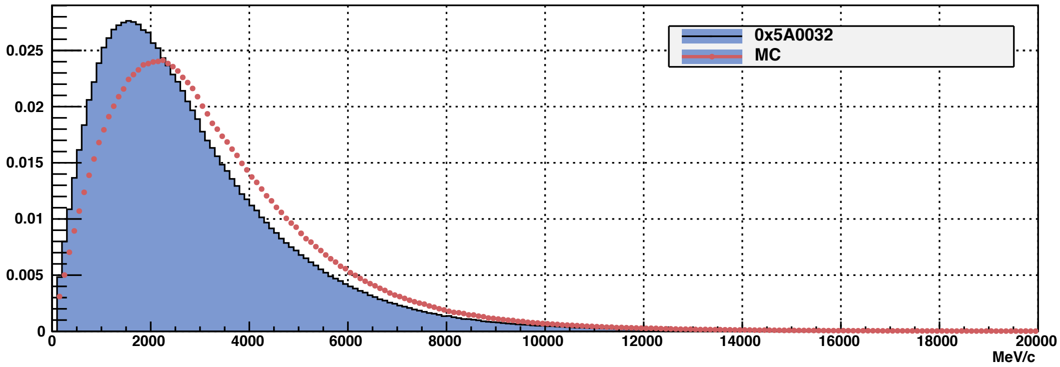

Figure 4.2: Normalised and sWeighted single J/ψ p_{T} distribution of data (blue) and MC (red). The data sample was collected with a TCK of 0x5A0032.

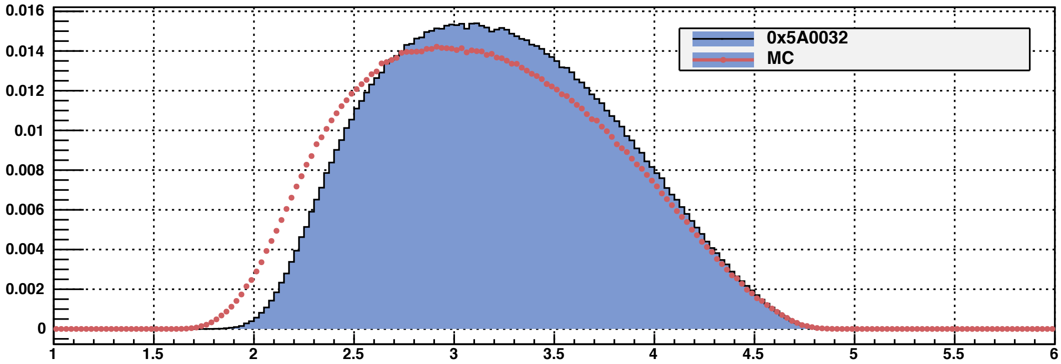

Figure 4.3: Normalised and sWeighted single J/ψ rapidity distribution of data (blue) and MC (red) J/ψ . The data sample was collected with a TCK of 0x5A0032.

between data and MC [90]. A correction table used to account for the difference in efficiency of the track reconstruction between data and MC is shown in Fig. 4.4. This table was evaluated on 2011 data and compared to MC samples generated using 2011 conditions. Additionally, the IsMuon selection criteria efficiency is also known to differ between data and MC [60] and therefore a further correction table was used to account for this, as shown in Fig. 4.5. The white area shows a region which could not be assessed due to low statistics and the binning of the efficiency was driven by statistics. For regions of phase space where the table is not defined, the last bin value is used.

The unknown polarisation of the J/ψ pair can affect the reconstruction and selection efficiency by changing the opening angle between the produced muons. This efficiency was therefore initially calculated as a function of p_{T}, rapidity and 'polarisation angle', the angle between the direction of the positive muon and the Lorentz boost from the lab frame to the J/ψ centre of mass frame. (This reconstruction efficiency is referred to as

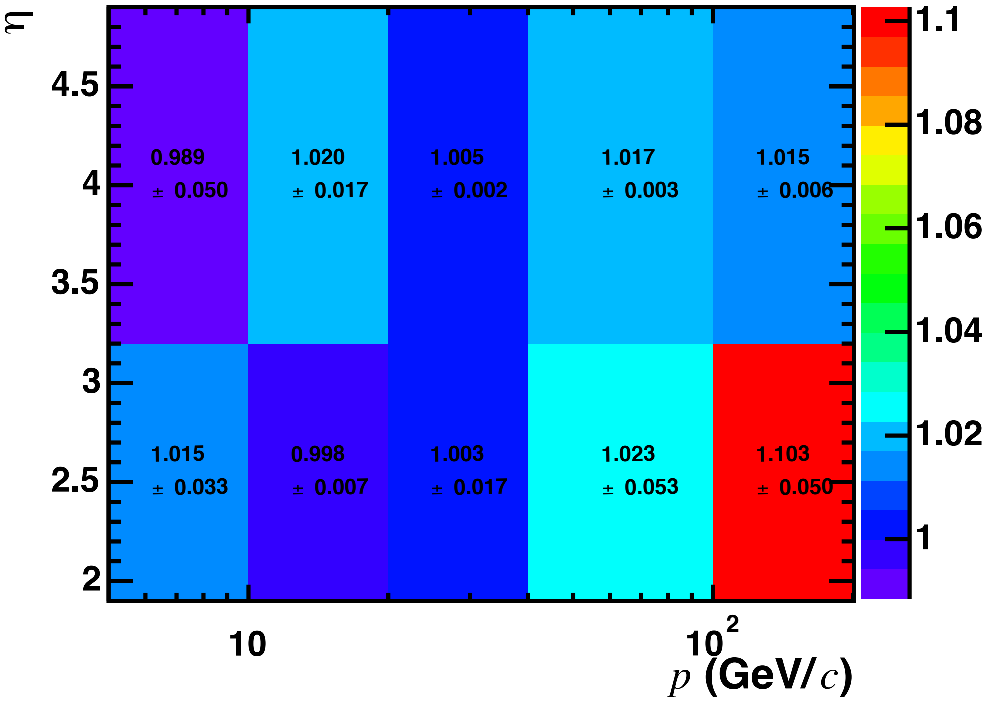

Figure 4.4: Tracking efficiency ratio between data and MC as a function of particle momentum and pseudorapidity [90].

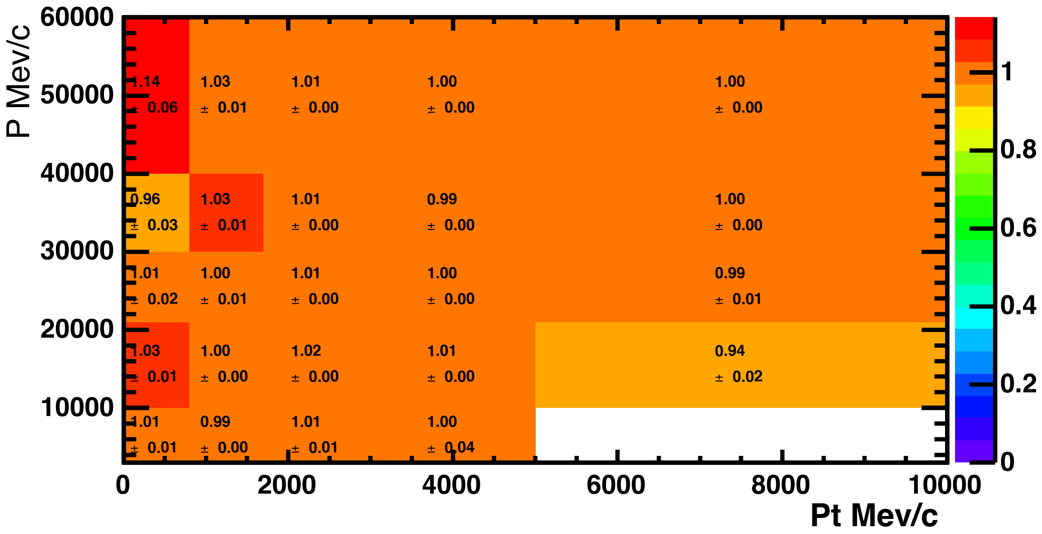

Figure 4.5: IsMuon ratio between data and MC as a function of particle p_T and momentum [60].

'3D'). However, the selection criteria used in this study resulted in a 3D efficiency, shown in Fig. 4.6, that did not measure all of the phase space, particularly for large values of polarisation angle. Therefore, an efficiency as a function of only p_T and rapidity ('2D') was used in this study. The uncertainty due to the unknown polarisation was estimated using a weighting procedure, which is described in Sec. 4.9.8.

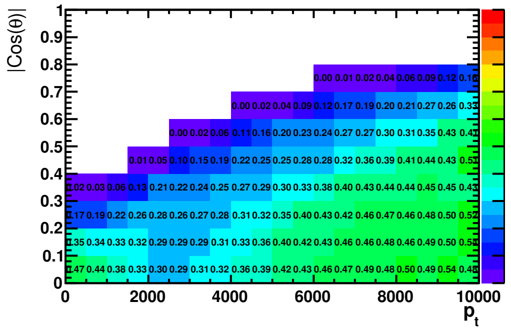

(a) $2.0 \leq y < 2.44$ (b) $2.44 \leq y < 2.88$

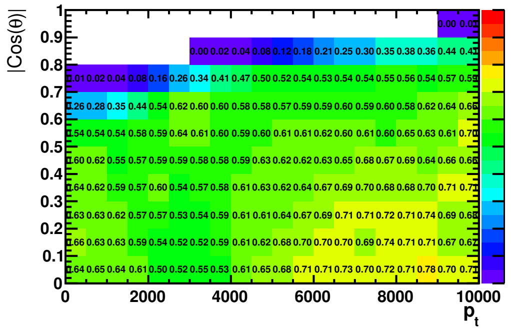

(c) $2.88 \leq y < 3.32$ (d) $3.32 \leq y < 3.76$

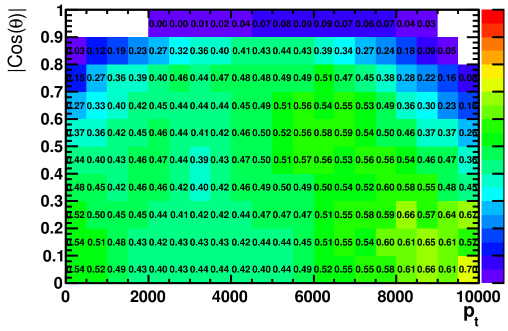

(e) $3.76 \leq y < 4.2$

Figure 4.6: The '3D' reconstruction and selection efficiency as a function of the rapidity, p_{T} and polarisation angle, for the Magnet Up data sample. Bins with no data are shown in white.

The reconstruction and selection efficiency was evaluated with 20 p_{T} bins in the range 0 - 10 GeV, and 15 y bins in the range 2 - 4.2. The reconstruction and selection efficiency for TCK 0x5A0032 can be see in Fig. 4.7, the remaining TCK efficiencies can be seen in Appendix C.3. The efficiencies of the two magnet polarities do not significantly differ.

The efficiency of the selection of four muons matched to the same primary vertex,

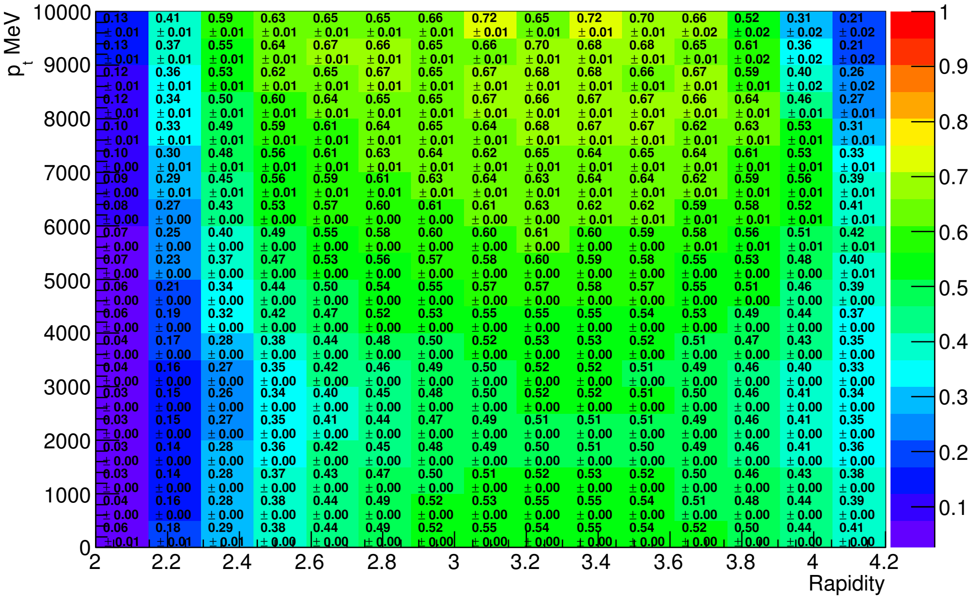

(a) Magnet Up

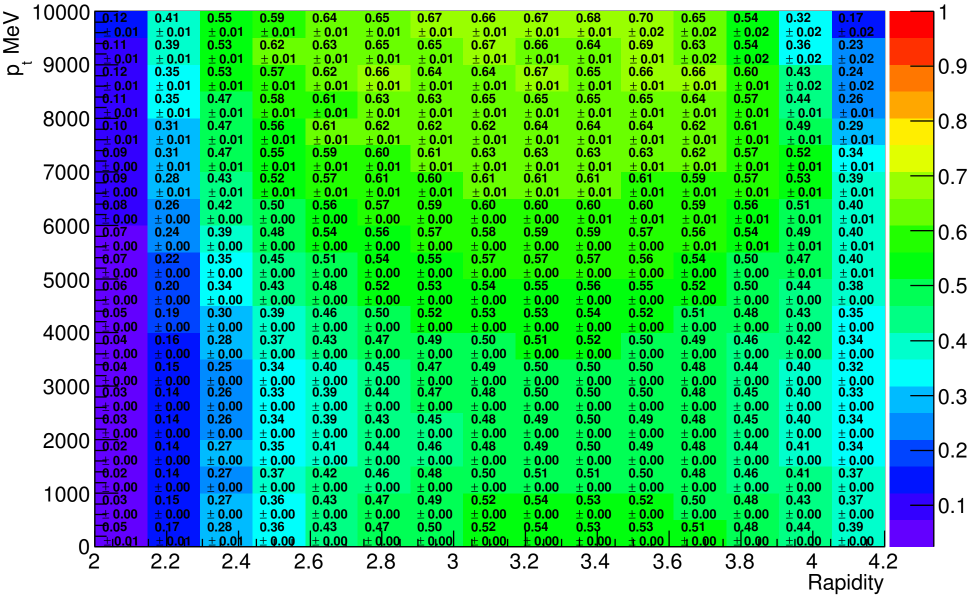

(b) Magnet Down

Figure 4.7: The reconstruction and selection efficiency for TCK 0x5A0032.

$\chi^2_{DTF}/nDoF < 5$ could not be simply evaluated on the single J/ψ MC sample. Instead, this efficiency was estimated on a MC sample of 2 M double J/ψ events. The decay tree fitter efficiency as a function of the selection on the four muon vertex can be seen in Fig. 4.8. The efficiency of the selection of $\chi^2_{DTF}/nDoF < 5$, used in this analysis, was calculated to be 0.9865 ± 0.0003.

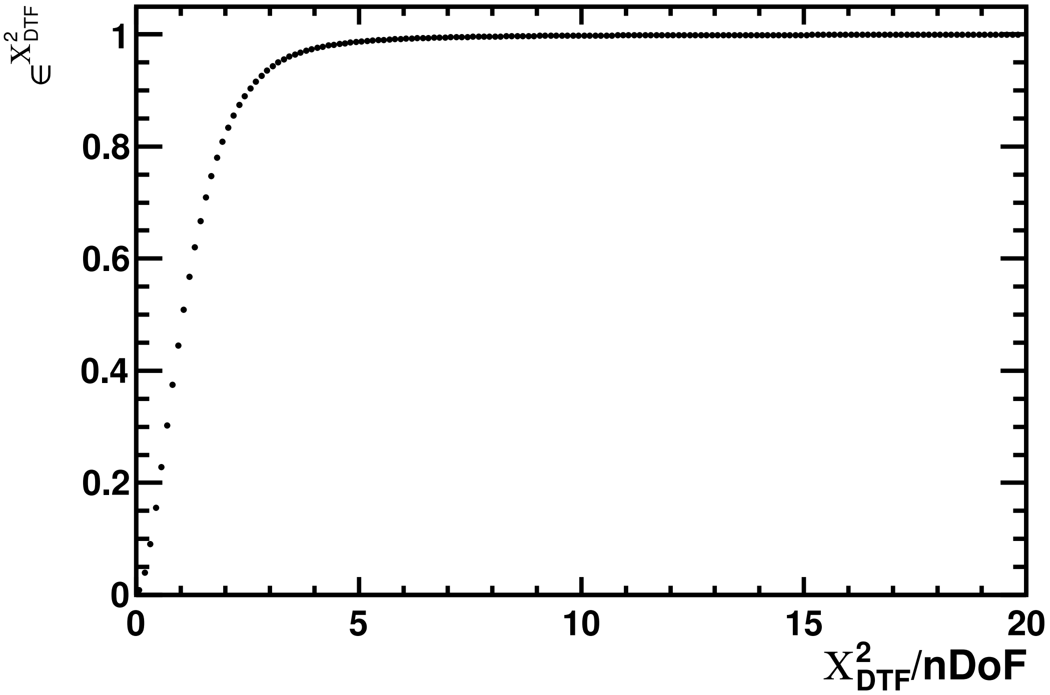

Figure 4.8: The decay tree fitter efficiency as a function of the selection on the two *J/ψ* vertex, calculated using MC.

4.7.2 Geometric Acceptance Efficiency

The *J/ψ* Monte Carlo sample used in the calculation of the reconstruction and selection efficiency is generated with the *J/ψ* and daughters inside a cone of opening angle 400 mrad. In order to account for events where the *J/ψ* are inside the acceptance but the di-muon pairs are outside, not allowing the decay chain to be reconstructed, an efficiency must be introduced, ϵ^{geo}.

A generation level MC sample of *J/ψ* → *μ μ*, described in section 4.3.2, was used to estimate the correction factor using

$$\epsilon^{geo} = \left(\frac{N^{geo}_{acc}}{N^{geo}}\right) \tag{4.9}$$

where N^{geo}_{acc} is the number of *J/ψ* with daughters in the LHCb acceptance, and N^{geo} is the number of events generated in the generation level sample, which includes those events where the *J/ψ* is inside the acceptance but the muons are not. The geometric acceptance efficiency is shown in Fig. 4.9, with 5 bins in rapidity between $2 < y < 4.5$ and 20 bins in p_{T} between 0 and 10 GeV.

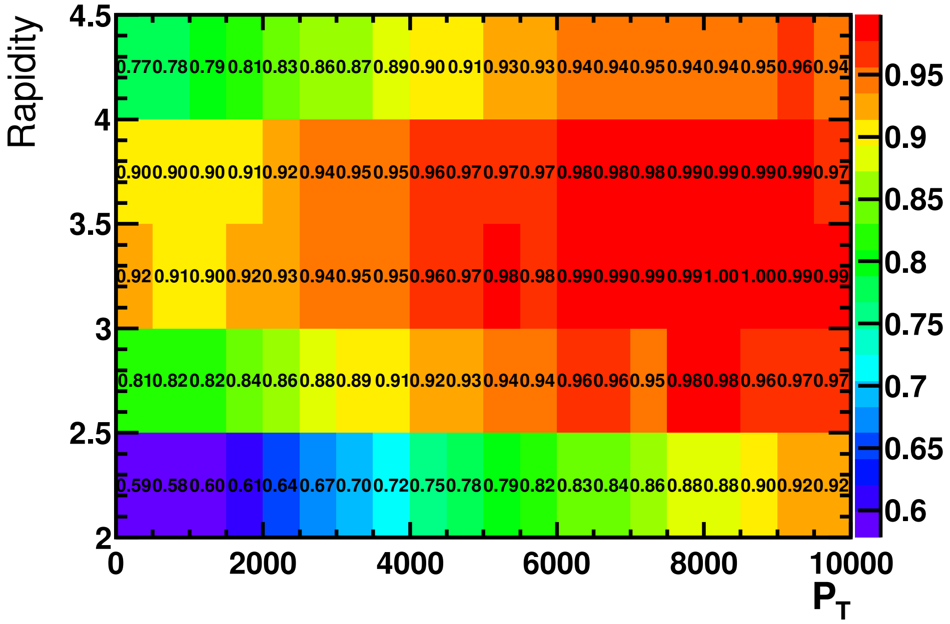

(a) Magnet Up

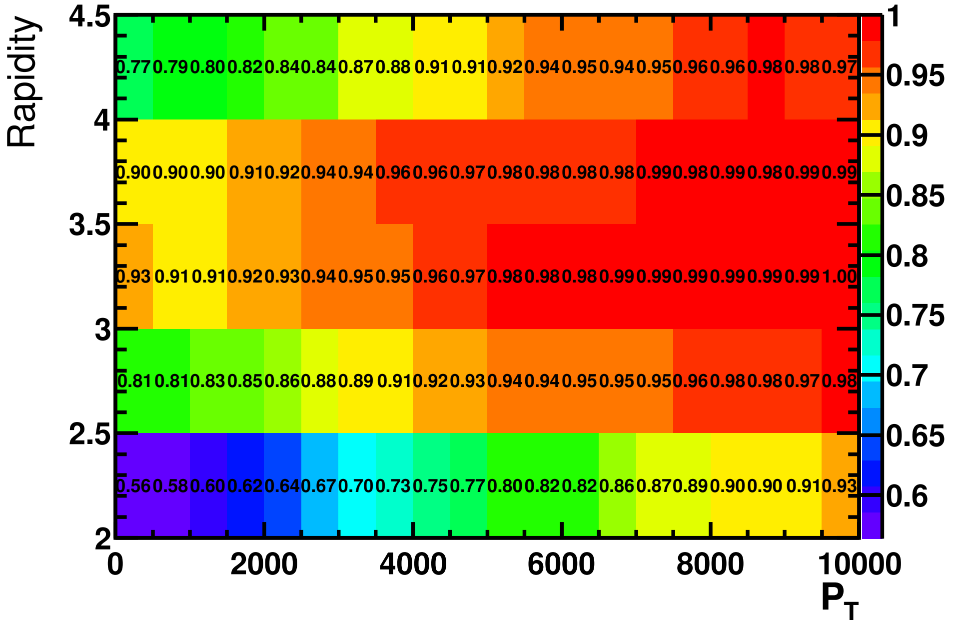

(b) Magnet Down

Figure 4.9: The geometric acceptance efficiency as a function of rapidity and transverse momentum.

4.7.3 Muon Identification Efficiency

The efficiency of the selection of candidate muons, $\epsilon_{1\mu}^{\mu ID}$, was estimated from an inclusive J/ψ data sample as a function of the muon identification variable, P_{NNMu}, and calculated individually for μ^+ and μ^-. All selection criteria for obtaining individual J/ψ candidates were applied as described in Sec. 4.5, apart from P_{NNMu}, which was varied in the interval 0 to 1. The muon identification efficiency was calculated using

$$\epsilon_{1\mu}^{\mu ID}(\alpha) = \frac{N^{P_{NNMu}>\alpha}}{N^{TOT}} \tag{4.10}$$

where $N^{P_{NNMu}>\alpha}$ is the number of J/ψ where either the positive or negative muon passes $\mathrm{P}_{NNMu} > \alpha$ and N^{TOT} is the total number of J/ψ. The numerator and denominator were obtained from a fit to the J/ψ invariant mass, using a double Crystal Ball for the signal and an exponential for the background. The DCB parameters were set to the same values as outlined in Sec. 4.6. The mean and width of the denominator DCB were left free, whilst the mean and the width of the numerator were fixed to those of the denominator. The muon identification efficiency as a function of P_{NNMu} is shown in Fig. 4.10, with an efficiency of 0.94 calculated for the selection of $\mathrm{P}_{NNMu} > 0.5$.

This study used a muon ID efficiency calculated as a function of muon p_{T} and rapidity for each individual TCK. The efficiency is calculated with a variable binning, chosen so that the number of entries in each bin is the same. The μ^+ muon ID efficiency for a TCK of 0x5A0032 can be seen in Fig. 4.11; the full set of muon identification efficiency plots can be seen in Appendix C.2.

4.7.4 Trigger Efficiency

There are two trigger levels in the LHCb experiment; the Level-0 trigger (L0) and the High Level trigger (HLT), consisting of HLT1 and HLT2, as described in Sec. 2.2.6. The trigger efficiency, $\epsilon_{J/\psi}^{trg}$, for the selection of $J/\psi \to \mu^+\mu^-$ events that pass the L0 and HLT triggers has been determined on data using the TISTOS [94] method. This method initially defines two categories; if the presence of the signal alone in the event is sufficient to generate a trigger decision then the event is 'Triggered On Signal' (TOS) and events

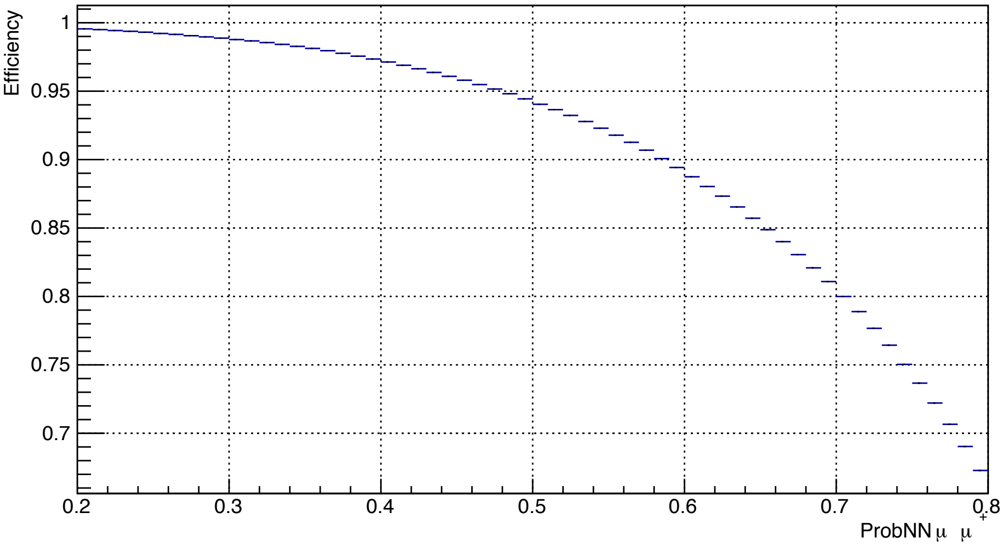

Figure 4.10: The single muon identification efficiency as a function of the P_{NNMu} selection criteria for μ^+.

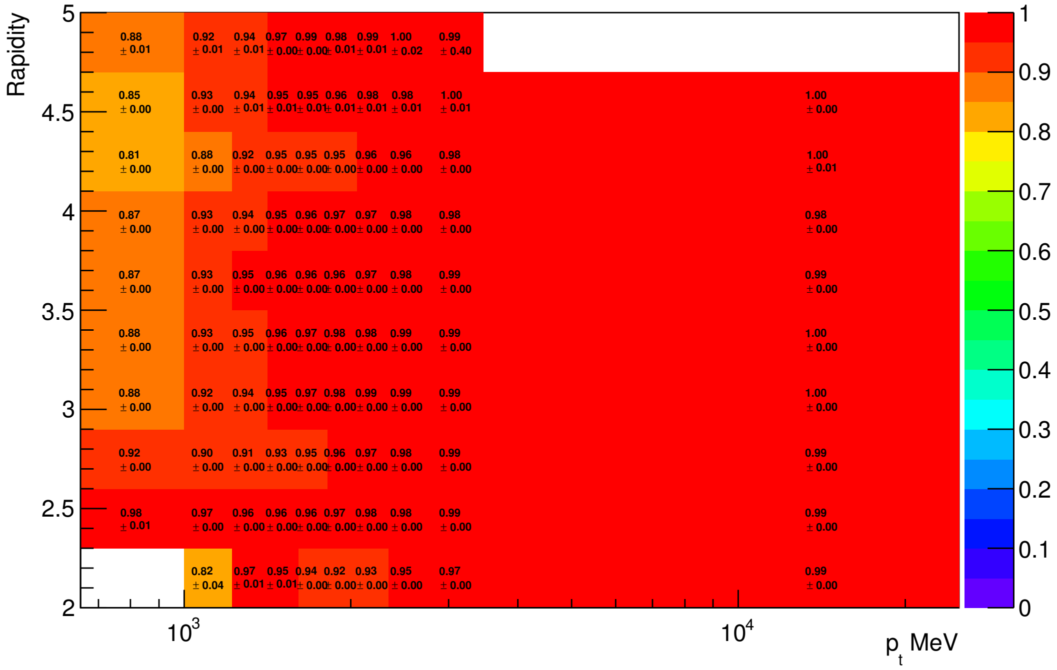

Figure 4.11: The single μ^+ identification efficiency for $P_{NNMu} > 0.5$ as a function of muon p_{T} in MeV and muon rapidity, for TCK 0x5A0032 magnet up. Two bins for which no values were able to be calculated due to low statistics are shown in white.

where the 'rest' of the event apart from the signal are sufficient to generate a positive trigger signal are 'Triggered Independent of Signal' (TIS). Using these two categories, events only triggered by signal are described as $\cancel{TIS}\&TOS$, events only triggered by the rest of the event are $TIS\&\cancel{TOS}$, events triggered by both are $TIS\&TOS$ and if both the signal and the rest of the event is required for a positive trigger then the event is classified as $\cancel{TIS}\&\cancel{TOS}$. These classifications mean that TIS events define an unbiased sample from which the TOS trigger efficiency for selecting single J/ψ events can be calculated using

$$\epsilon^{trg}_{J/\psi} = \left(1 + \frac{N^{TIS\&\cancel{TOS}}}{N^{TIS\&TOS}}\right)^{-1}. \tag{4.11}$$

The trigger efficiency for double J/ψ events has been evaluated using the factorisation

$$\epsilon^{trg} = 1 - (1 - \epsilon^{trg}_{J/\psi}) \times (1 - \epsilon^{trg}_{J/\psi}). \tag{4.12}$$

The L0 TOS lines utilised in the calculation of the trigger efficiency were the muon and di-muon trigger lines. The L0 TIS lines consisted of the muon and di-muon lines and all the electron, photon and hadron lines. For HLT1, the TOS lines used were all the di-muon, single muon and muon track lines and the TIS category used all the HLT1 decision lines. For HLT2 the TOS lines included all di-muon, single muon and track muon and the TIS used all the HLT2 decision lines.

The trigger efficiency was calculated individually for each TCK, as the selection criteria and data taking conditions can change over time. The single J/ψ trigger efficiency was evaluated in 20 bins of p_{T} and 5 of rapidity. The number of J/ψ events for each trigger category, in each bin, was extracted from a fit to the invariant mass distribution of the muon pair, using a double sided Crystal Ball function for the signal and an exponential for the background. The $\cancel{TIS}\&TOS$ category mass distribution was fitted and the width and position of the J/ψ peak was allowed to vary and these values were used to fix the parameters in the fit of the TISTOS categories required by Eqn. 4.11.

The trigger efficiencies for a TCK of 0x5A0032 are shown in Fig. 4.12; there is no significant difference in distribution between the two magnet polarities. The trigger efficiencies for the remaining TCK are displayed in Appendix C. The limiting factor in the calculation of the trigger efficiency is the small size of the $TIS\&\cancel{TOS}$ sample, which can lead to significant errors in the trigger efficiency. A possible improvement to the estimation of the trigger efficiency, in order to negate the effect of the small size of the

$TIS\&\cancel{TOS}$ sample, is to calculate the trigger efficiency as

$$\epsilon^{trg}_{J/\psi} = \left(\frac{N^{TIS\&TOS}}{N^{TIS}}\right) \tag{4.13}$$

where N^{TIS} is the total number of events categorised as TIS. Calculation of the trigger efficiency using this method can significantly reduce the associated statistical error.

4.7.5 Global Event Cut Correction

To remove very high multiplicity events, which would take excessively long to reconstruct, Global Event Cuts (GEC) were applied after the L0 trigger, during data taking. The main requirement on the GEC is a selection on the number of hits in the SPD detector, known as the SPD multiplicity. The **L0Muon** line excludes events with a SPD multiplicity above 600, the **L0Dimuon** line excludes events with a SPD multiplicity above 900.

The effect of GEC has been studied using data; the SPD distribution of the **L0Dimuon** line was fitted and extrapolated to infinity. The integral up to a SPD multiplicity of 600, 900 and infinity was calculated, and the ratio of these values were used to estimate the GEC for the **L0Muon** and the **L0DiMuon** line. The background subtracted SPD distribution was obtained with an sPlot technique [82] using the invariant mass of the J/ψ distribution. The background subtracted SPD distribution was modelled by the sum of two Γ-functions, which was empirically found [92] to describe the distribution, where the Γ-function is defined for n, a positive integer, as

$$\Gamma(n) \ = \ (n-1)! \tag{4.14}$$

In this study, a single Γ-function was also tested, but did not fit the distribution as successfully, as measured by the χ^2 of the quality of the line fit. The GEC efficiency was estimated separately for differing numbers of primary vertices ('nPV') measured in the event, due to the dependance of the SPD distribution upon this quantity, and was calculated for each TCK and magnet polarity.

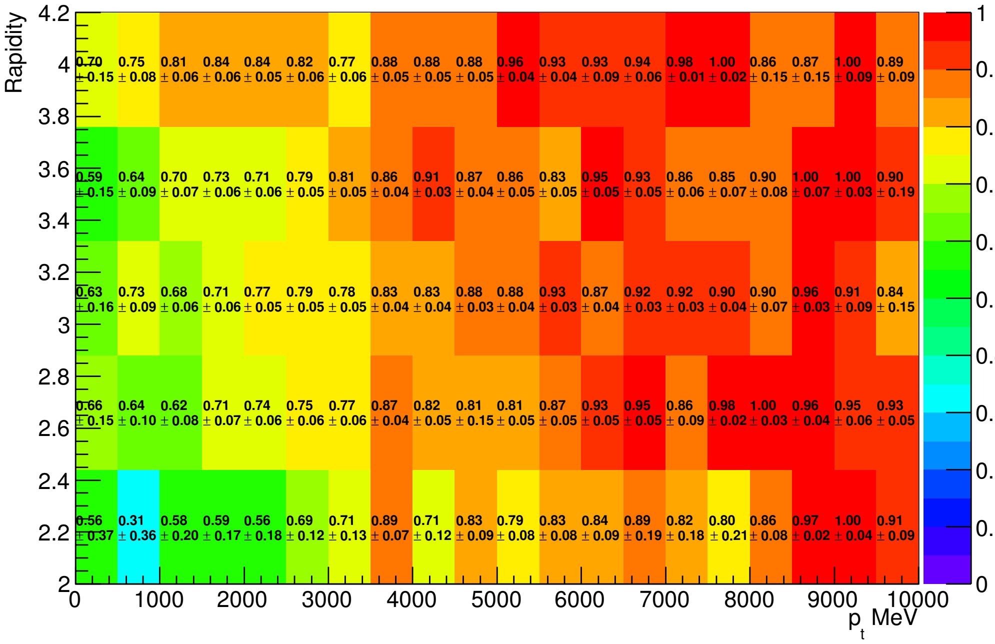

(a) Magnet Up

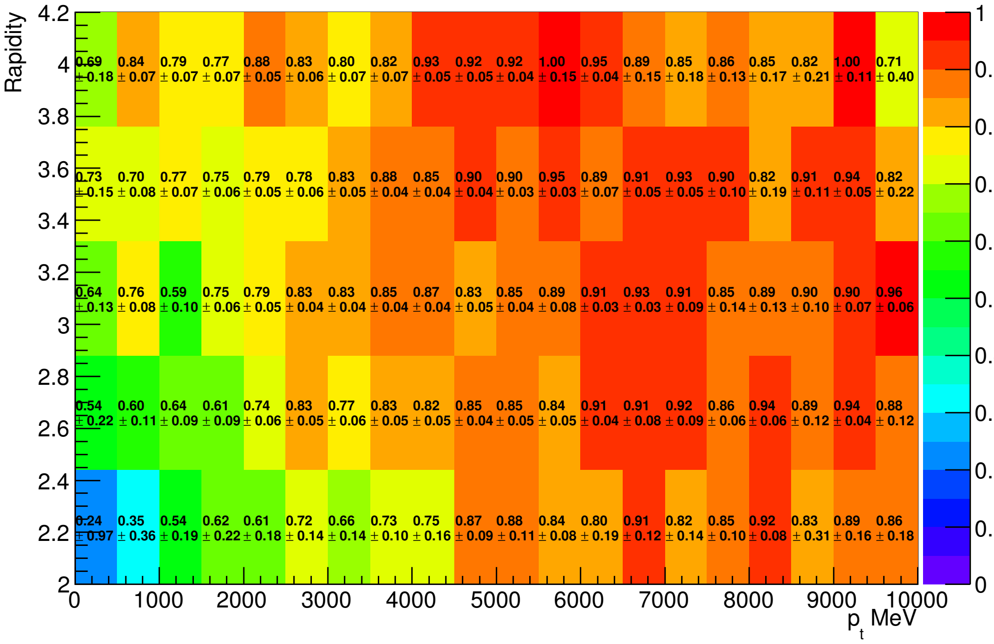

(b) Magnet Down

Figure 4.12: Trigger efficiency as a function of rapidity and transverse momentum for TCK 0x5A0032.

The SPD distribution for the **L0DiMuon** line for TCK = 0x760037 for events with 1 nPV can be seen in Fig. 4.13(a) and for 2 nPV in Fig. 4.13(a). A full set of SPD

Table 4.5: GEC efficiency as a function of number of primary vertices, for the muon and dimuon stripping line with a TCK of 0x5A0032, Magnet Up.

NPV	L0Muon	L0Dimuon
1	1.00 ± 0.00	1.00 ± 0.00
2	0.97 ± 0.00	1.00 ± 0.00
3	0.90 ± 0.00	1.00 ± 0.00
4	0.76 ± 0.01	1.00 ± 0.00
5	0.62 ± 0.01	1.00 ± 0.00
6	0.47 ± 0.16	0.98 ± 0.00
7	0.38 ± 0.31	0.98 ± 0.08

distributions as a function of nPV can be seen in Appendix D. The GEC efficiency as a function of nPV for a TCK of 0x5A0032 is shown in Fig. 4.14(a) for the **L0Muon** line and in Fig. 4.14(b) for the **L0DiMuon** line, with the values displayed in Table. 4.5. The full set of GEC efficiencies by TCK are shown in Appendix. D. It can be seen that for the **L0DiMuon** line, the GEC efficiency is approximately constant at a value of ∼1. The **L0Muon** line has an efficiency which reduces from ∼1 for nPV = 1 to ∼0.4 for nPV = 7. The difference in the GEC efficiencies between the two lines is caused by the difference in the value of the SPD multiplicity where GEC are imposed. It should be noted that in the final selection of double J/ψ events, only 6 % have more than 3 nPV, and none have nPV = 7.

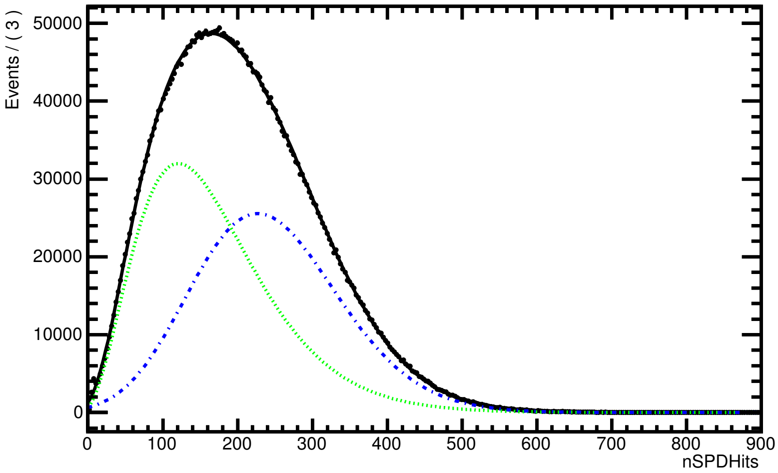

(a) Number of primary vertices = 1.

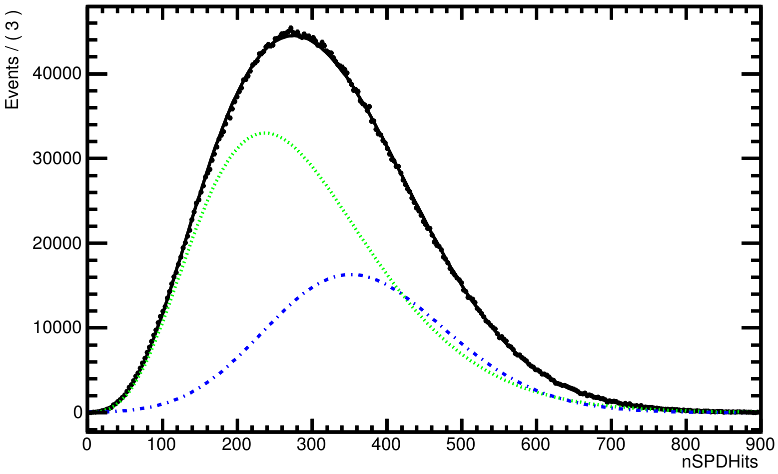

(b) Number of primary vertices = 2.

Figure 4.13: The **L0Dimuon** SPD background subtracted multiplicity distribution fitted with the sum of two gamma functions for a TCK of 0x760037, with the individual gamma functions shown in the dotted and dashed blue and green lines and the sum of the two gamma functions shown by the solid black line.

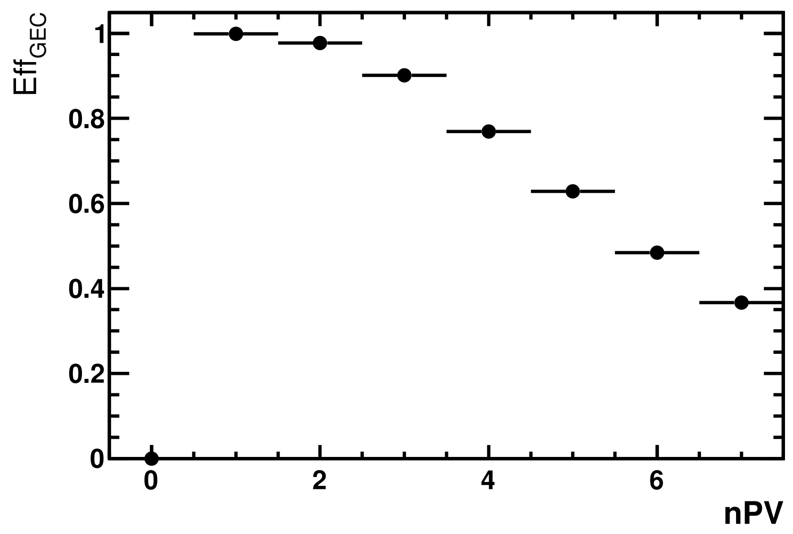

(a) L0Muon.

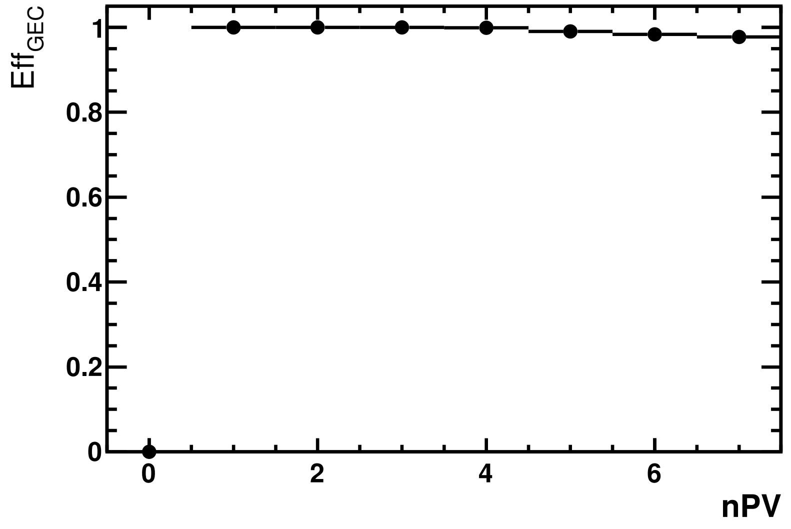

(b) L0DiMuon.

Figure 4.14: The GEC efficiency as a function the number of primary vertices for a TCK of 0x5A0032, Magnet Up.

4.8 Efficiency Corrected Yield

In order to extract the efficiency corrected yield, N^{corr}, an sPlot technique [82] is utilised. Using the invariant mass fit of the double J/ψ pair, each of the signal candidates is given a statistical weight, w_i, for it to be signal. The corrected yield is given by

$$N^{corr} = \sum_{i=0}^{n} \frac{w^i}{\epsilon_i^{tot}} \tag{4.15}$$

where ϵ_i^{tot}, the total efficiency for that event, is given by equation 4.5. This gives a weighted yield of 21517 ± 1400 double J/ψ events.

4.9 Systematic Uncertainty

A number of sources of systematic uncertainty have been studied and their effect upon the cross-section has been evaluated.

4.9.1 Track Reconstruction

The track reconstruction efficiency, which measures the probability that a charged particle that passes through the full tracking system is reconstructed, differs between data and MC, as described in Sec. 4.7.1. A systematic uncertainty of 0.4 % per track was calculated from a process of re-weighting a number of parameters of the MC, such as the number of primary vertices or the number of tracks in different sub-detectors [90]. The uncertainties associated with the tracking efficiency were included in the evaluation of the reconstruction efficiency uncertainty, as described in Sec. 4.9.2.

4.9.2 Efficiency Weighting

The systematic uncertainty associated with the efficiency event weighting was evaluated by the use of a ‘toy’ Monte Carlo study. For each toy, a random efficiency was generated, distributed as a Gaussian of mean equal to the measured efficiency and error equal to the efficiency error. This random efficiency was used to weight the signal events using equation 4.6. The difference between this toy cross-section and the nominal cross-section was plotted, with the sigma of this distribution taken as the uncertainty. This process was carried out using 1000 toys for each of the muon identification, trigger, geometric and selection and reconstruction efficiency. The uncertainties arising from the IsMuon and tracking efficiency corrections, as described in Sec. 4.7.1, were evaluated with the reconstruction efficiency.

The plots from the toy MC study are shown in Fig 4.15. The uncertainty for the selection and reconstruction efficiency, $\delta\epsilon^{sel\&rec}$, was estimated to be 0.21 %, for the trigger efficiency, $\delta\epsilon^{trg}$, to be 2.1 %, for the muon ID efficiency, $\delta\epsilon^{\mu ID}$, to be 0.13 %, and for the geometric efficiency, $\delta\epsilon^{geo}$, to be 0.19 %. The trigger efficiency error is approximately an order of magnitude larger that the other efficiency weighting errors; as described in Sec. 4.7.4, the small size of the $TIS\&\cancel{TOS}$ sample leads to large statistical errors in the trigger efficiency. This can be negated by using an alternative form of the trigger efficiency, as shown in Eqn. 4.13, which can significantly reduce the statistical errors on the trigger efficiency and therefore the systematic errors in the efficiency weighting.

4.9.3 Global Event Cuts

The effect of global event cuts, applied in order to remove very high multiplicity events, has been studied in Sec. 4.7.5. The error on the GEC efficiency was estimated by use of a toy MC study. The parameters of the fit of the SPD distribution were smeared by a Gaussian with width equal to the errors on those parameters. These smeared parameters were then used to calculate a new GEC efficiency, and the difference between this value and the nominal signal was plotted, with the sigma of this distribution taken as the error. This process was carried out for 1000 toys. As shown in Table. 4.5 the uncertainty associated with the GEC is small and can be ignored.

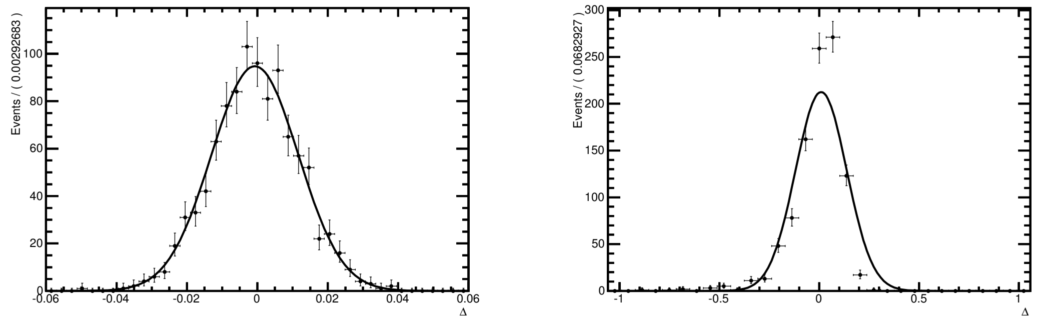

(a) Reconstruction and selection efficiency toy error. (b) Trigger efficiency toy error.

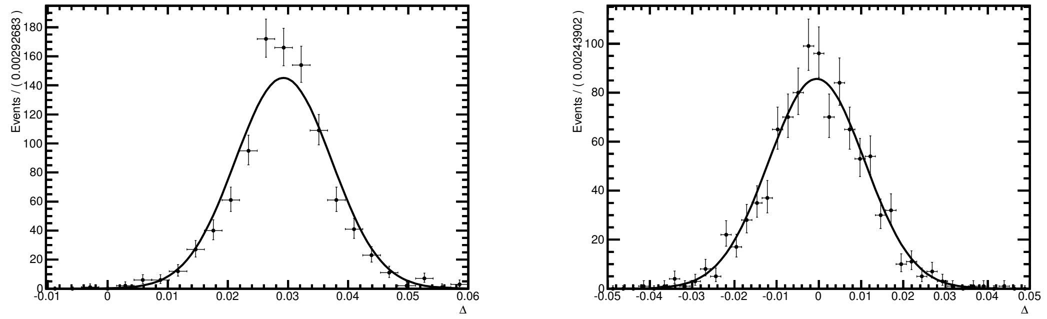

(c) Muon identification efficiency toy error. (d) Geometric acceptance efficiency toy error.

Figure 4.15: Efficiency weighting uncertainty, showing the difference between the nominal cross-section and the toy cross-section, which is randomly generated with a Gaussian of mean equal to the measured efficiency and error equal to the efficiency error.

4.9.4 Decay Tree Fitter

The effect of the selection of the decay tree fitter upon the four muon vertex was examined in Sec. 4.7.1. An efficiency of 0.9865 ± 0.0003 was found. The uncertainty associated with the decay tree fitter is small and can therefore be ignored.

4.9.5 Fit Model

The systematic uncertainty associated with the choice of fit model was estimated by studying the impact on the total cross-section of altering the fit parameters and fit model, as described in Sec. 4.6. Table 4.6 summarises the fit yield and cross-section obtained from using alternative fit models and a systematic error of 2.0 % was associated with the fit model.

Table 4.6: Raw yields and cross-sections calculated using various fit models.

Model	Fit Yield	Cross-section nb
DCB	1816 ± 50	6.08 ± 0.40 (stat) ± 0.29 (syst)
DCB 'Optimum'	1856 ± 50	6.19 ± 0.40 (stat) ± 0.30 (syst)
Hypatia	1831 ± 51	6.13 ± 0.40 (stat) ± 0.30 (syst)
CB	1778 ± 50	5.95 ± 0.40 (stat) ± 0.29 (syst)

4.9.6 Multiple Candidate Events

The muons from each event were combined in all viable opposite charge combinations to create two J/ψ. 21 events had two viable combinations of muons that survived all selection criteria. All of these 'multiple candidate' events were included in the final selection, as explained in Sec. 4.6. The percentage difference in the resulting cross-section between removing one of the multiple candidate events at random and keeping all of the multiple candidate events was 0.5 %, which was taken as the associated systematic uncertainty.

4.9.7 Cross Feed

Due to resolution effects, J/ψ candidates can potentially be assigned to the wrong p_T or y bin. The p_T and y resolution was previously studied in Ref. [95] using a J/ψ MC sample and the p_T resolution estimated to be 12.7 ± 0.2 MeV/c and the y resolution to be $(1.4 \pm 0.1) \times 10^{-3}$. The size of the y resolution is negligible compared to the y bin width and can therefore be ignored. The more significant effect of the p_T resolution was studied in Ref. [95] and a systematic of 0.5 % per bin assigned.

4.9.8 Uncertainty Due to the Unknown Polarisation

Unpolarised MC samples are used in this study, however, the J/ψ pair may be polarised. Polarisation of the J/ψ pair would change the opening angle between the produced muons, which would lead to to a distortion in the reconstruction and selection and geometric efficiency distributions. In order to calculate the maximum uncertainty due to the unknown polarisation, the reconstruction and selection efficiency was re-calculated

Table 4.7: Cross-sections calculated using polarisation weighted reconstruction and selection efficiencies. The efficiency is a function of p_{T} and rapidity with 20 bins in p_{T} and 10 in rapidity.

Polarisation State	$\sigma_{J/\psi\, J/\psi}$
No Polarisation	6.08 ± 0.40 (stat) ± 0.29 (syst)
Transversely Polarised	7.38 ± 0.50 (stat) ± 0.34 (syst)
Longitudinally Polarised	4.54 ± 0.30 (stat) ± 0.24 (syst)

for maximally longitudinally and transverse polarisations and the cross-section also recalculated. Each event is weighted with the normalised two dimensional angular decay distribution

$$f_p = \frac{d^2N}{d\cos\theta d\phi} = (\frac{3}{4\pi(3+\lambda_\theta)})(1 + \lambda_\phi \cos^2\theta + \lambda_{\theta\phi}\sin 2\theta\cos\phi + \lambda_\phi \sin^2\theta\cos 2\phi) \quad (4.16)$$

where θ, the polarisation angle, is the angle between the direction of the positive muon and the Lorentz boost from the lab frame to the J/ψ centre of mass frame. ϕ is the azimuthal angle, measured with respect to the plane formed by the momenta of the colliding hadrons in the J/ψ rest frame. λ_θ, $\lambda_{\theta\phi}$ and λ_ϕ are the polarisation parameters. When the polarisation is completely longitudinal the polarisation parameters (λ_θ, $\lambda_{\theta\phi}$, λ_ϕ) have values (-1, 0, 0); when the polarisation is completely transverse the parameters have value (1, 0, 0). The reconstruction and selection efficiency was evaluated by reweighting on an event by event basis

$$\epsilon_{rec} = \frac{\sum_{i=1}^{N_{Rec}} f_p(\theta,\phi)}{\sum_{i=1}^{N_{Tot}} f_p(\theta,\phi)} \quad (4.17)$$

A totally transversely polarised J/ψ pair would mean that the measured cross-section was increased to ∼7.4 nb, whereas, a totally longitudinal polarisation could reduce the cross-section to be ∼4.5 nb, as is shown in Table 4.7. The uncertainty due to the unknown polarisation is therefore approximately 30%, although it should be noted that if the J/ψ polarisation is zero, then the cross-section measured in this study will be correct.

Table 4.8: Relative systematic errors on cross-section measurements.

Source	Systematic uncertainty
$\delta\epsilon^{sel\&rec}$	0.21 %
$\delta\epsilon^{trg}$	2.1 %
$\delta\epsilon^{\mu ID}$	0.13 %
$\delta\epsilon^{geo}$	0.19 %
Fit model	2.0 %
Double Counted events	0.5 %
Cross Feed	0.5%
J/ψ polarisation	30 %
Luminosity	3.5%
J/ψ to $\mu^+\mu^-$ branching ratio	2 × 1%

4.9.9 Additional Sources of Uncertainty

The luminosity is measured with an error of 3.5 % over the data taking period used in this analysis [87]. Additionally, the branching ratio of J/ψ to μ^+ μ is 5.93 ± 0.06 [17].

4.9.10 Summary

A summary of the systematical uncertainties, which are assumed to be uncorrelated, is contained in Table 4.8. The uncertainty due to the unknown polarisation of the J/ψ pair is almost an order of magnitude larger than other sources of uncertainty. Aside from this uncertainty, the uncertainty due to the luminosity measurement, the error on the trigger efficiency and the error on the fit model dominate the remaining uncertainties. The errors due to the uncertainty on the mu PID, geometric and selection and reconstruction efficiencies are small, as are the errors due to cross feed and double counted events.

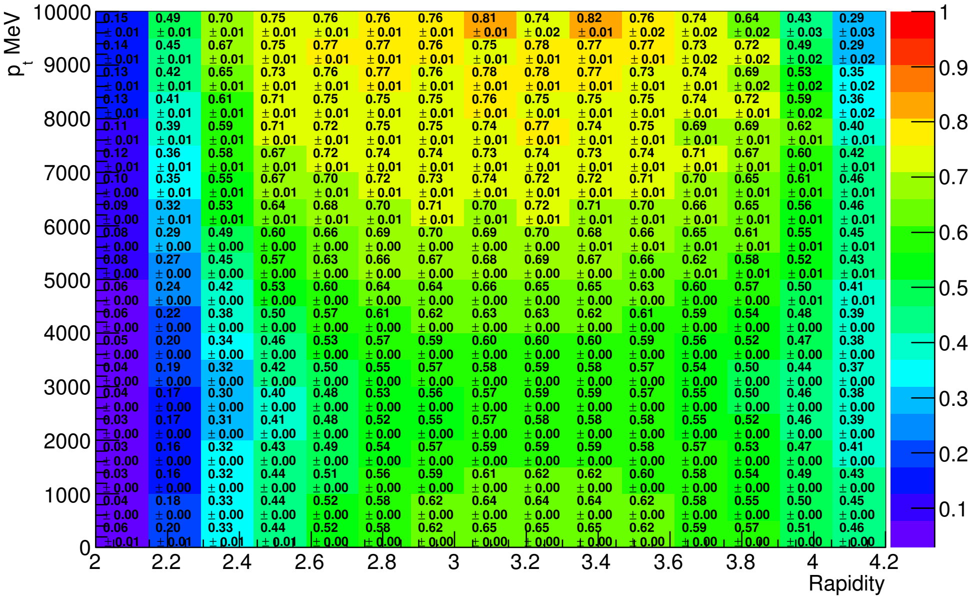

(a) Longitudinally reweighted.

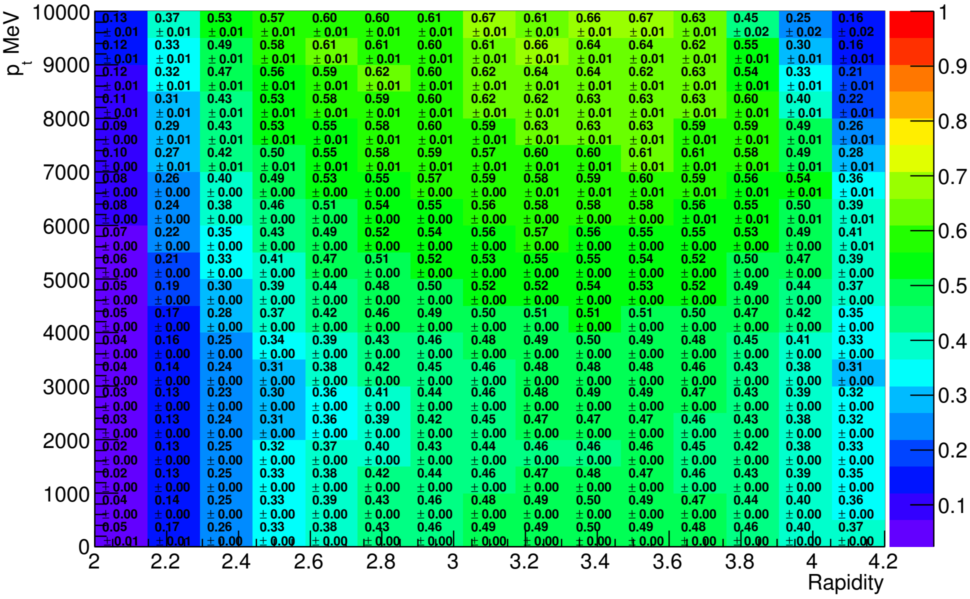

(b) Transversely reweighed.

Figure 4.16: The reweighed reconstruction and selection efficiency for TCK 0x5A0032, magnet up polarity.

4.10 Results

4.10.1 Cross-section

The cross-section for the production of double J/ψ pairs is estimated from

$$\sigma = \frac{1}{\mathcal{L} \times \mathcal{B}^2_{\mu^+\mu}} \times N^{corr} \tag{4.18}$$

where $\mathcal{L}$ is the integrated luminosity, $\mathcal{B}_{\mu^+\mu}$ is the branching ratio of J/ψ to μ^+ μ^- (5.93 ± 0.06 [17]) and N^{corr} is the efficiency corrected number of events.

The cross-section at a centre of mass energy of $\sqrt{s} = 7$ TeV in the LHCb rapidity range of $2 < y < 4.2$ with $p_{\mathrm{T}} < 10$ GeV has been calculated using an integrated luminosity of 998 ± 35 pb^{-1} to be

$$6.08 \pm 0.40 \text{ (stat)} \pm 0.29 \text{ (syst) nb.}$$

where the errors do not include the uncertainty due to the unknown polarisation of the double J/ψ, which is estimated to be up to 30 %.

Ref. [10] reported a double J/ψ production cross-section of 5.1 ± 1.0 (stat) ± 1.1 (syst) nb, made on 37.5 pb^{-1} of data collected at LHCb at $\sqrt{s} = 7$ TeV. This measurement was carried out with a larger rapidity fiducial volume of $2 < y < 4.5$, so cannot be directly compared, but appears to be compatible with the result from this study. The cross-section calculated in this study will be compared to selected theoretical models in Sec. 4.10.4.

4.10.2 Cross-section stability

The double J/ψ cross-section was also calculated for each individual TCK, which can be seen in Table. 4.9. The cross-section is consistent between individual TCK datasets.

Table 4.9: Double J/ψ cross-section by TCK.

TCK	σ nb
0x5A0032	4.56 ± 0.53 (stat) ± 0.24 (syst)
0x6D0032	5.82 ± 0.68 (stat) ± 0.28 (syst)
0x730035	5.41 ± 0.57 (stat) ± 0.27 (syst)
0x760037	7.09 ± 0.98 (stat) ± 0.33 (syst)
0x790038	6.08 ± 0.72 (stat) ± 0.29 (syst)
0x790037	4.50 ± 1.08 (stat) ± 0.23 (syst)

4.10.3 Differential Cross-Sections

A number of differential cross-sections have been calculated and compared to theoretical models. In order to extract each differential cross-section, the double J/ψ sample was binned in 10 equal sized bins in the relevant variable of interest, except for the absolute difference in rapidity distribution, which used 5 bins due to problems with fitting the tail of the distribution. The number of double J/ψ events within each bin was estimated using a two dimensional maximum likelihood fit method with a double sided Crystal Ball function for the signal and an exponential function for the background, as described in Sec. 4.5. The efficiency corrected yield was extracted, using an sPlot technique, as described in Sec. 4.8.

The transverse momentum spectra for the J/ψ pair in the region 0 - 10 GeV/c, with a bin width of 1 GeV/c, is displayed in Fig. 4.17, which shows the distribution peaks in the region around 1.5 GeV/c. The total invariant mass spectra for the J/ψ pair between 6 - 14 GeV/c^2, with a bin size of 0.8 GeV/c^2, is shown in Fig. 4.18; the distribution is at a maximum in the low mass range between 6 - 7.5 GeV/c^2. The absolute difference in rapidity between the J/ψ pair, in the region of $|\Delta y|$ of 0 - 2, with bin size of 0.4, is displayed in Fig. 4.19; for smaller values of $|\Delta y|$ the distribution is at its maximum, which falls away as the rapidity difference increases. Fig. 4.20 shows the difference in azimuthal angle between the two J/ψ with ten bins in the region 0 - π; this distribution is approximately flat. The error bars show the statistical and systematic uncertainty combined in quadrature, excluding the uncertainty due to the unknown polarisation.

Table 4.10: Sum of the differential cross-sections for the transverse momentum spectra (total p_{T}). the total invariant mass (Total Inv. Mass), the absolute difference in rapidity distribution (Δy) and the difference in azimuthal angle ($\Delta\phi$).

Differential Distribution	$\sigma_{J/\psi\, J/\psi}$ nb
Total p_{T}	6.02 ± 0.93 (stat) ± 0.52 (syst)
Total Inv. Mass	6.06 ± 0.91 (stat) ± 0.39 (syst)
$\lvert\Delta y\rvert$	6.09 ± 0.84 (stat) ± 0.57 (syst)
$\Delta\phi$	6.11 ± 1.18 (stat) ± 0.43 (syst)

The integrals of the differential cross-sections are shown in Table. 4.10, which are in good agreement with the total measured cross-section. The measured cross-section in each differential distribution bin is tabulated in Appendix. E.

4.10.4 Comparison with Theoretical Models

The total and differential cross-sections, calculated in the previous sections, are compared with two different LO CS SPS models and a NRQCD DPS prediction in this section. The theoretical predictions have been made using the same fiducial volume as this study.

The first LO CS SPS [34] model, ('BLLN-SPS') includes feed-down from $\psi(2s)$ states but not χ_c states. Initial State Radiation (ISR) is taken into account with the Pythia MC generator, with the hard subprocess scale set at the J/ψ transverse mass, $m_T^{J/\psi}$, which is equal to $\sqrt{m^2_{J/\psi} + {p_{\mathrm{T}}}^2}$, where $m_{J/\psi}$ is the physical J/ψ mass. The second LO CS SPS [44] model, ('KKS-SPS') does not include feed-down from higher charmonium states. The hard subprocess scale is also set at the J/ψ transverse mass and ISR and the intrinsic p_{T} of the partons are implemented in the MC event generator Herwig++ v2.4.2 [96]. The NRQCD DPS prediction, also from Ref. [44], doesn't explicitly include feed-down from higher states, but this is implicitly included by approximating the matrix element for production of a prompt J/ψ through a fit to experimental p_{T} differential cross-section distributions. The result is calculated in Herwig++, with ISR and intrinsic p_{T} of the partons switched off, as these are taken into account in the approximated matrix element.

The BLLN-SPS model predicts a total cross-section of 3.2 nb with an uncertainty of approximately 30 %, the KKS-SPS model predicts a cross-section of 1.7 nb and the DPS predicts a value of 3.3 nb. The two LO CS SPS models cannot be directly compared, as the KKS-SPS model does not include feed-down, which accounts for approximately 25 % of the KKS-SPS cross-section. Additionally, uncertainties on the LO CS SPS models are significant, which are dominated by the choice of scale of the hard subprocesses [34]. The DPS prediction also contains significant uncertainties, one of the main sources of which is the value of the effective cross-section, used in the factorisation of the two independent scatterings. The KKS-SPS predicted cross-section only accounts for approximately half of the measured value. The BLLN-SPS and DPS model together predict a cross-section of approximately 5 nb, which, accounting for no feed-down in the BLLN-SPS model and potential uncertainties, is in reasonable agreement with the measured value.

The BLLN-SPS and DPS predictions are compared to the measured differential cross-sections in Fig 4.17(a), 4.18(a), 4.19(a) and 4.20(a). The DPS prediction is shown by a dashed purple line, the SPS with ISR is shown with a red dashed line, the blue dashed line indicates the SPS with ISR and intrinsic p_{T} of the partons, and the solid green line shows the sum of the SPS with ISR and intrinsic p_{T} and the DPS distribution. There is no significant difference between the two SPS distributions, which will be referred to together as BLLN-SPS. The KKS-SPS model is shown alongside the experimentally determined values in Fig 4.17(b), 4.18(b), 4.19(b) and 4.20(b). The dotted line shows the prediction of the model, with the red band showing the uncertainty that arises from varying the scale at which the hard subprocesses occur from 0.5 $m_T^{J/\psi}$ to 2 $m_T^{J/\psi}$.

In addition to theoretical uncertainties in the total predicted cross-section, theoretical uncertainties also affect the shape of the predicted differential distributions. As the model dependent ISR and intrinsic p_{T} effects in the two LO CS SPS models give rise to the transverse momentum spectrum of the *J/ψ* pair, this causes large theoretical uncertainties in the transverse momentum distribution and also the azimuthal correlation distributions. In particular, the shape of the azimuthal correlation distribution is model dependent [44]. However, the invariant mass spectrum is largely insensitive to these uncertainties, and is therefore a better indication of the underlying LO CS model. The difference in rapidity distribution is also more stable against model dependent effects, as compared to the difference in azimuthal angle [34].

In Fig. 4.17(a), the DPS contribution to the transverse momentum spectrum in the low p_{T} region is approximately double that of the KKS-SPS. For values of p_{T} above 5 GeV/c the KKS-SPS and DPS contributions are approximately the same. The experimental cross-section for values of p_{T} larger than 3 GeV/c is well described by the combined KKS-SPS and DPS models. However, for low values of p_{T}, the combined distribution only makes up around half of the measured cross-section and fails to predict the peaked experimental distribution around ~1.5 GeV/c. The BLLN-SPS model shown in Fig. 4.17(b) again fails to model the peak in the experimental distribution and substantially underestimates the magnitude of the entire distribution.

The DPS total invariant mass spectrum for the *J/ψ* pair distribution, shown in Fig. 4.18(a), has a broader shape than the KKS-SPS model. The experimental total invariant mass spectrum is in good agreement with the combined KKS-SPS and DPS distribution, particularly for values above 10 GeV/c^2, where the DPS contribution dominates. The shape of the BLLN-SPS theoretical distribution in Fig. 4.18(b) largely matches the shape of the measured distribution, although underestimating the size of it.

The DPS and KKS-SPS difference in rapidity distribution between the two *J/ψ* mesons, shown in Fig. 4.19(a) are approximately the same size for small $|\Delta y|$, however, the DPS contribution becomes increasingly dominant for increasing rapidity separation; above a value of $|\Delta y|$ of $\sim$ 1.2, the KKS-SPS is insignificant compared to the DPS. For small values of rapidity difference the combined KKS-SPS and DPS distribution describes the experimental distribution well. For larger $|\Delta y|$ values, which are thought to contain little or no contribution from LO CS SPS, the DPS contribution is well matched to the experimental results. The BLLN-SPS model in Fig. 4.19(b) increasingly underestimates the distribution for increasing $|\Delta y|$.

In Fig. 4.20(a) the DPS azimuthal angle correlation distribution is shown to be flat, which is due to the *J/ψ* being produced in independent scattering events. The KKS-SPS distributions are peaked towards $\Delta\phi = 0$, whereas, the BLLN-SPS is completely flat, with the uncertainty bands becoming increasingly large away from the centre of the distribution. The difference in shape of the $\Delta\phi$ distribution between the two LO CS models is due to the fact that the shape of the LO CS $\Delta\phi$ distribution is model dependent [34]. The LO CS SPS $\Delta\phi$ distributions are therefore not a useful variable to discriminate between the models. The experimental distribution is reasonably well described by the combined DPS and KKS-SPS distribution in Fig. 4.20(a), although the theory tends to underestimate the experiment for larger values of $\Delta\phi$. The BLLN-SPS model from 4.20(b) estimates the shape better, but underestimates the magnitude.

4.10.5 Summary

The cross-section for double J/ψ production at a centre of mass energy of $\sqrt{s} = 7$ TeV in the LHCb rapidity range of $2 < y < 4.2$ with $p_{\mathrm{T}} < 10$ GeV has been calculated to be 6.08 ± 0.40 (stat) $\pm$ 0.29 (syst) nb. The uncertainty due to the unknown polarisation is estimated to be up to 30 %, although the measured cross-section will be correct in the absence of polarisation.

LO CS SPS models predict a cross-section which at most is approximately half the value measured in this study [44] [34]. Double parton scattering contributions to the cross-section may be as large, or larger than LO CS SPS contributions [44]. However, next to leading order CS contributions may also be significant [22] as could be NRQCD LO and NLO predictions [35], which therefore could reduce the need for a substantial DPS component. Colour octet contributions to production are thought to be negligible in the LHCb acceptance [35]. At present, significant theoretical uncertainties exist in all of these predictions, although, it appears that the LO CS SPS model alone cannot account for the measured cross-section.

The theoretical differential distributions are similarly affected by theoretical uncertainties, although the invariant mass distribution and difference in rapidity distribution are less affected by the model dependent effects. These two differential distributions could indicate there is a significant DPS component to double J/ψ production; the Δy distributions show signal in a region of large rapidity difference where there is expected to be little or no contribution from LO CS SPS, as does the total invariant mass spectrum for values above 10 GeV/c^2.

The results calculated in this study appear to indicate contributions other than the LO CS SPS are required to explain the total cross-section of double J/ψ production, and selected differential cross-sections may indicate a DPS component is present, but further work both theoretical and experimental, primarily measuring the polarisation of the J/ψ pair, is required to more fully elucidate this.

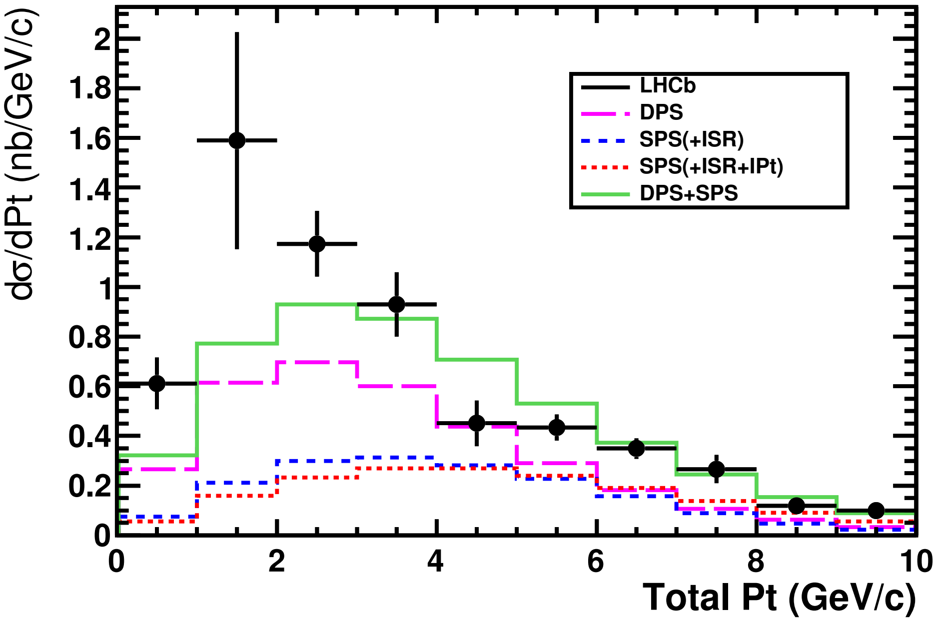

(a) 'KKS-SPS' and DPS predictions [44], with the dashed purple line showing the DPS contribution, the red dotted line showing the SPS with ISR, the blue dashed line showing the ISR and intrinsic p_{T} SPS, and the solid green line showing the sum of the DPS and ISR and intrinsic p_{T} SPS.

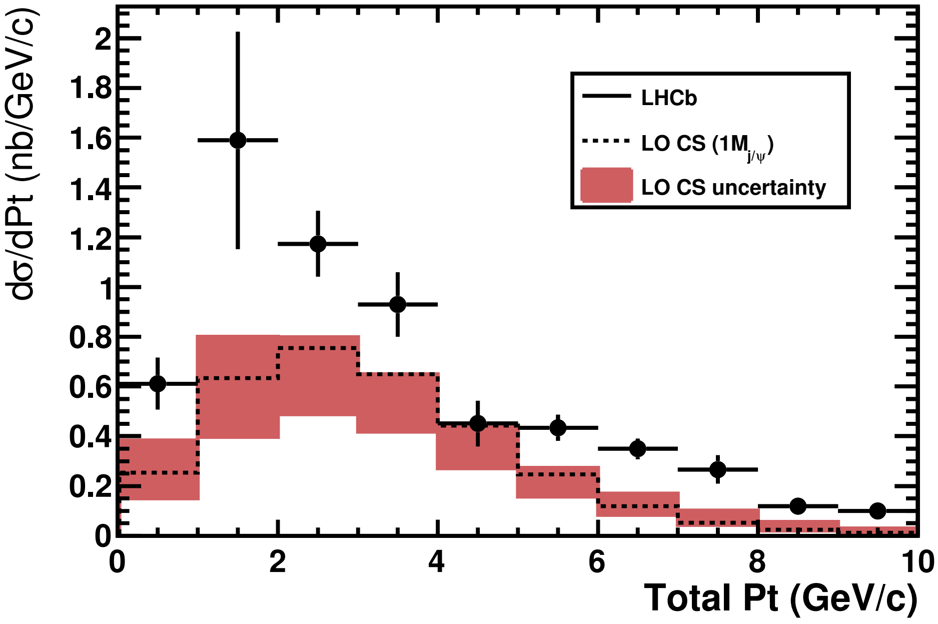

(b) 'BLLN-SPS' model Ref. [34] shown with black dotted line, with associated uncertainty shaded in red.

Figure 4.17: The transverse momentum spectra of the double J/ψ pair. The error bars show the statistical and systematic uncertainty combined in quadrature, excluding the uncertainty due to the unknown polarisation.

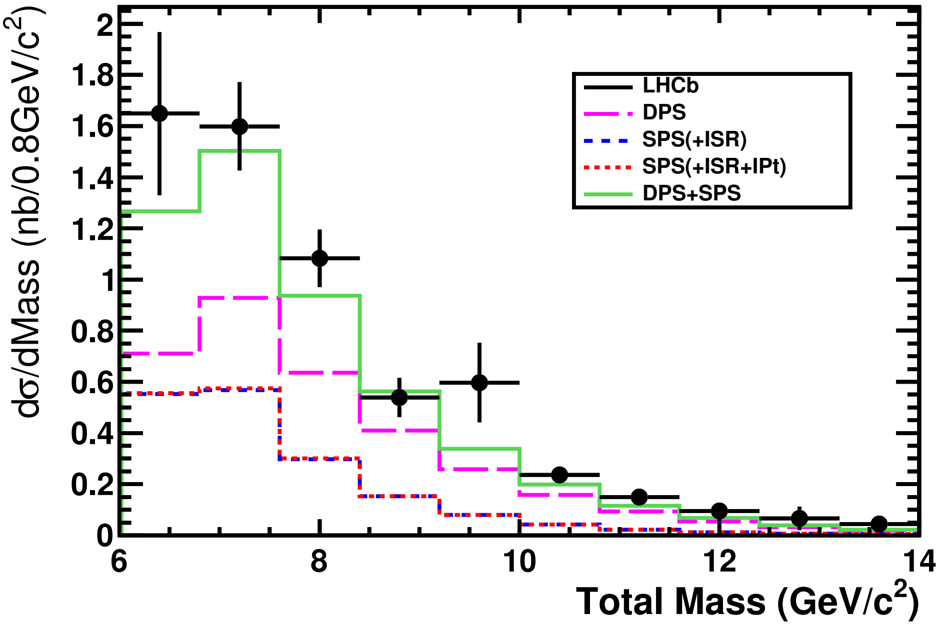

(a) 'KKS-SPS' and DPS predictions [44], with the dashed purple line showing the DPS contribution, the red dotted line showing the SPS with ISR, the blue dashed line showing the ISR and intrinsic p_{T} SPS, and the solid green line showing the sum of the DPS and ISR and intrinsic p_{T} SPS

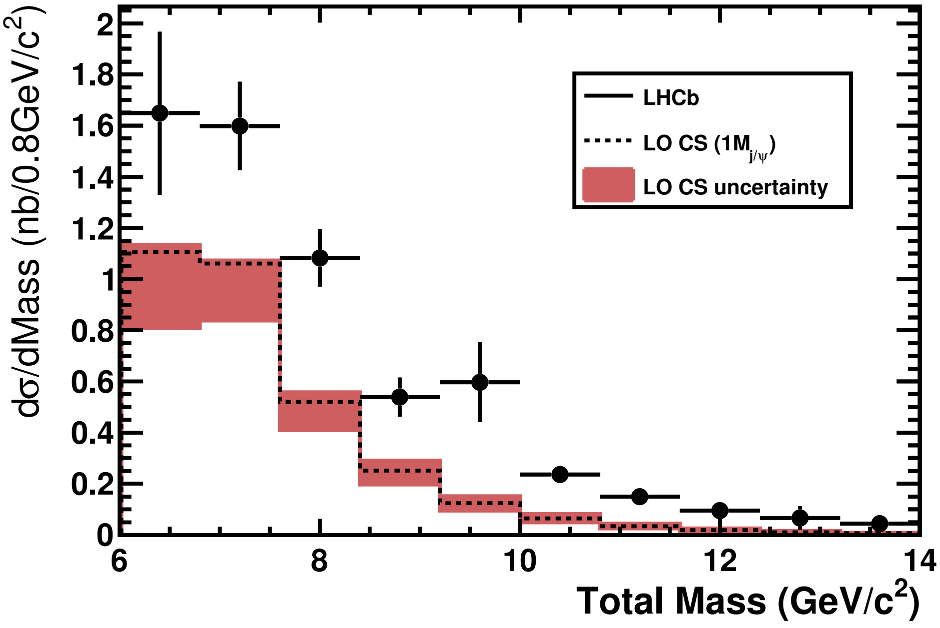

(b) 'BLLN-SPS' model Ref. [34] shown with black dotted line, with associated uncertainty shaded in red.

Figure 4.18: The total invariant mass spectra of the double J/ψ pair. The error bars show the statistical and systematic uncertainty combined in quadrature, excluding the uncertainty due to the unknown polarisation.

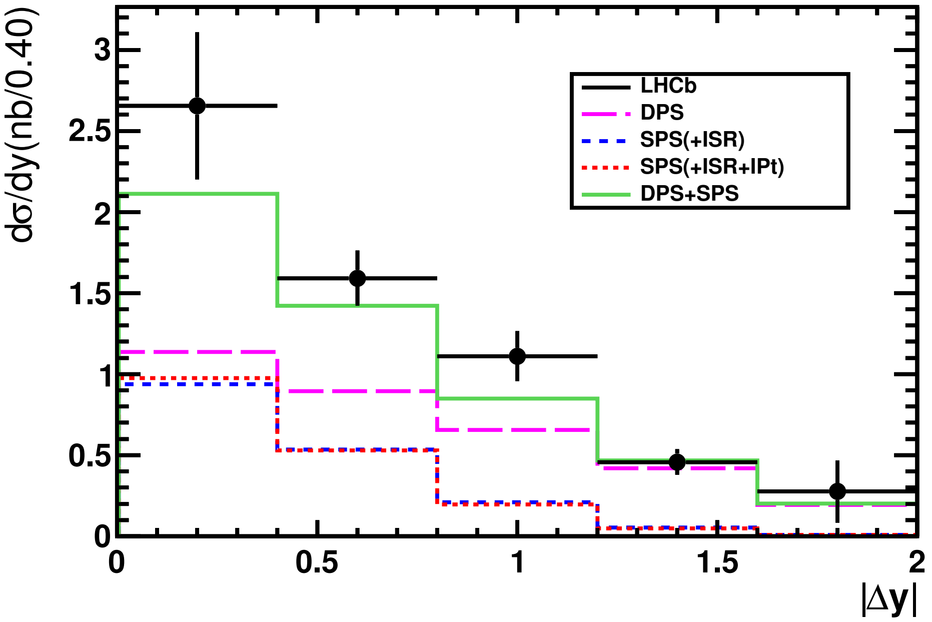

(a) 'KKS-SPS' and DPS predictions [44], with the dashed purple line showing the DPS contribution, the red dotted line showing the SPS with ISR, the blue dashed line showing the ISR and intrinsic p_T SPS, and the solid green line showing the sum of the DPS and ISR and intrinsic p_T SPS

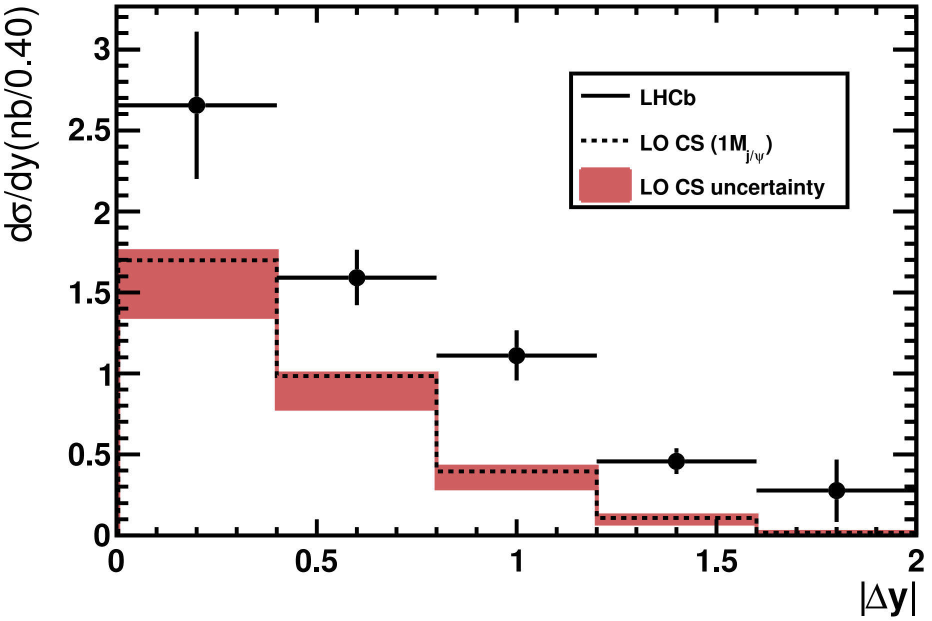

(b) 'BLLN-SPS' model Ref. [34] shown with black dotted line, with associated uncertainty shaded in red.

Figure 4.19: The absolute rapidity difference between the J/ψ pair. The error bars show the statistical and systematic uncertainty combined in quadrature, excluding the uncertainty due to the unknown polarisation.

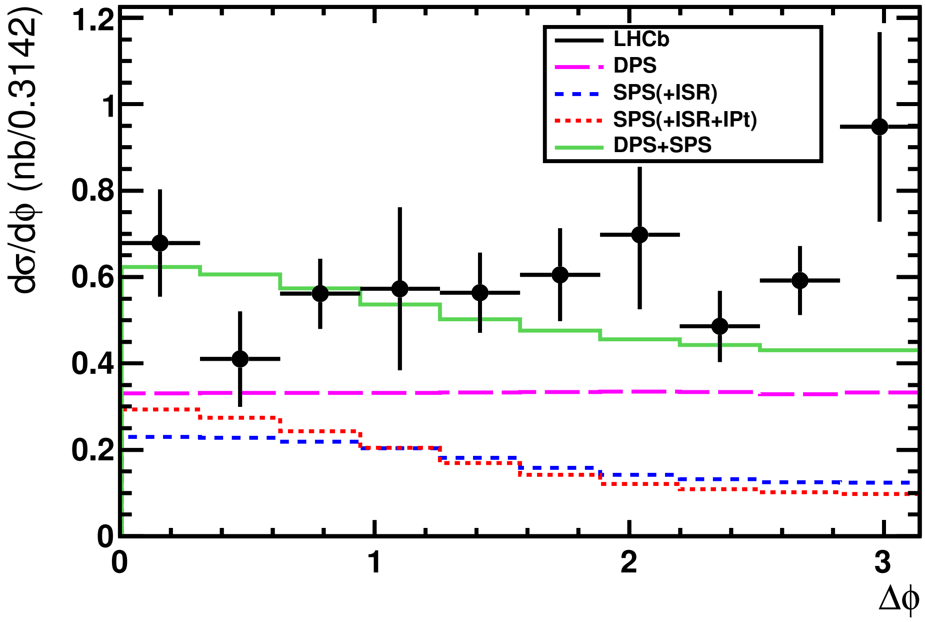

(a) 'KKS-SPS' and DPS predictions [44], with the dashed purple line showing the DPS contribution, the red dotted line showing the SPS with ISR, the blue dashed line showing the ISR and intrinsic p_{T} SPS, and the solid green line showing the sum of the DPS and ISR and intrinsic p_{T} SPS

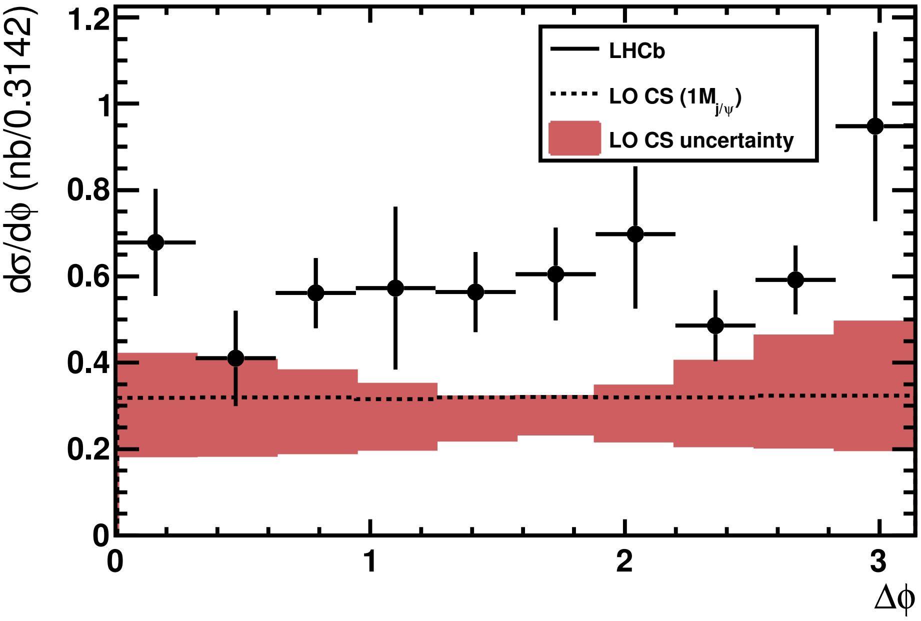

(b) 'BLLN-SPS' model Ref. [34] shown with black dotted line, with associated uncertainty shaded in red.

Figure 4.20: The azimuthal correlations for the J/ψ pair. The error bars show the statistical and systematic uncertainty combined in quadrature, excluding the uncertainty due to the unknown polarisation.

Chapter 5

Conclusions

The LHCb experiment is designed to make precision measurements of CP violation and to search for new physics in quantum loop processes. Particle identification is paramount to these goals and LHCb employs two Ring Imaging Cherenkov Detectors, RICH1 and RICH2, to this end. The performance of the RICH detectors strongly depends on a number of elements being properly aligned and calibrated. These elements include the RICH2 mirrors, which reflect Cherenkov photons out of the detector acceptance and onto photo-detectors. In Chapter 3, a procedure to speed up the RICH2 mirror alignment was developed, using only the track position in the RICH2 detector. It will be used in the HLT2 to pre-select tracks to evenly populate the mirror pairs used for alignment of the RICH2 mirrors, potentially reducing the amount of data that needs to be reconstructed by two orders of magnitude. Work is ongoing to turn the selection criteria into a HLT2 line.

Quarkonia production has been an active area of both theoretical and experimental endeavour since the discovery of the J/ψ particle four decades ago. Despite much progress, theoretical models still fail to fully describe both the kinematic and polarisation experimental data. Experimental uncertainties are already smaller than those on theoretical models, therefore, the study of further sources of quarkonium production, such as double J/ψ production are motivated. Double J/ψ production is also thought to offer an insight into events where two hard scatterings take place, which are expected to be significant in number at the LHC.

Double J/ψ production was first observed a little over three decades ago by the NA3 collaboration and was measured at a hadron collider for the first time by the LHCb experiment in 2010. More recently, double J/ψ production has also been measured at the CMS and D0 experiments, with both results indicating that DPS may be present. In Chapter 4, the cross-section for double J/ψ production at a centre of mass energy of $\sqrt{s} = 7$ TeV in the LHCb rapidity range of $2 < y < 4.2$ with $p_{\mathrm{T}} < 10$ GeV was measured to be 6.08 ± 0.40 (stat) ± 0.29 (syst) nb. The uncertainties on this value do not include the uncertainty due to the unknown polarisation, which was estimated to be up to 30 %. The cross-section appears to be consistent with the previous measurement at LHCb, although it cannot be directly compared, as the 2010 LHCb study was carried out in a slightly larger fiducial volume.

Significant uncertainties exist on theoretical models of double J/ψ production. Leading order colour singlet SPS models have uncertainties of at least 30 % and predict a cross-section that at most is approximately half the value measured in this study, although NLO CS contributions may also be significant. DPS contributions to production are theorised to be significant; potentially of the same order, or larger than LO CS SPS contributions, although uncertainties are also potentially large on this prediction. NRQCD LO and NLO order calculations may be able to account for the measured cross-section alone, although very large uncertainties of well over 100 % exist on these predictions. Colour octet production is thought to be negligible in the fiducial volume measured in this study, only becoming significant for a p_{T} above 10 GeV. The predicted theoretical differential distributions also have large uncertainties, although the invariant mass distribution and difference in rapidity distribution are less affected by model dependent effects than the combined p_{T} or difference in azimuthal angle distributions. The difference in rapidity is thought to be the most useful differential distribution in order to distinguish DPS and SPS production, with DPS being characterised by a larger rapidity difference than SPS. In this study, the measured Δy distributions show signal in a region of large rapidity difference where there is expected to be little or no contribution from LO CS SPS.

In conclusion, the cross-section for double J/ψ production calculated in this study appears to indicate contributions other than the LO CS SPS are required, and the difference in rapidity differential distribution may indicate a DPS component is present. However, in order to draw more firm conclusions, the polarisation of the J/ψ pair should be measured, in order to reduce the associated uncertainty, and also theoretical uncertainties should be further reduced.

Appendix A

RICH2 HLT Track Selection

Table A.1: Left hand side mirror pairs, showing the reconstruction efficiency, the x and y co-ordinates in the plane of the RICH2 primary mirrors in mm of selected sub-areas and the number of events required to pass through the RICH2 to find the requisite data to carry out the alignment for that mirror pair.

Mirror pair	ϵ_{ϕ}^{reco}	X_{start}	X_{end}	Y_{start}	Y_{end}	Events required
p12s8	0.50	125	150	115	162	139647
p16s8	0.09	10	70	0	200	201528
p16s12	0.59	50	150	388	424	63020
p20s12	0.47	92	138	626	662	967183
p20s16	0.60	50	75	840	870	5821445
p24s16	0.71	50	80	1010	1050	4193497
p8s8	0.29	10	40	-176	-120	84384
p8s4	0.58	50	75	-493	-307	51607
p4s4	0.46	70	190	-690	-612	159526
p4s0	0.52	135	181	-950	-885	1728460
p0s0	0.67	56	91	-1175	-1121	3875369
p12s9	0.71	330	360	-100	100	3891
p17s9	0.18	400	425	136	221	295831
p17s13	0.67	425	450	393	479	153868
p21s13	0.43	475	500	662	697	3308426
p21s17	0.39	471	506	870	930	4441071
p25s17	0.78	480	510	1248	1294	6243651
p9s9	0.32	423	469	-232	-120	60132
p9s5	0.58	375	400	-423	-400	434635
p5s5	0.49	467	533	-692	-656	767232
p5s1	0.32	500	600	-960	-840	1067981
p1s1	0.75	450	500	-1229	-1074	545478
p13s9	0.51	475	500	-110	10	63681
p13s10	0.68	733	800	50	150	174107
p18s10	0.21	825	850	100	250	1933720
p18s14	0.62	832	868	375	400	1829125
p22s14	0.53	920	980	621	707	1161192
p22s18	0.30	975	1000	930	1050	13497029
p26s18	0.77	900	1000	1274	1310	4121874
p22s19	0.11	1175	1250	900	1050	82861336
p27s19	0.72	1520	1607	1211	1277	51084416
p10s10	0.31	832	868	-232	-120	953719
p10s6	0.57	820	850	-568	-531	2299842
p6s6	0.59	900	950	-697	-662	2853442
p6s2	0.26	938	985	-950	-850	10029073
p2s2	0.72	880	905	-1280	-1190	7809411
p6s3	0.05	1100	1400	-1050	-750	26946222
p3s3	0.70	1382	1459	-1203	-1155	46827381
p14s10	0.72	906	941	-80	-40	196676
p14s11	0.53	1190	1220	-38	-2	4279539
p19s11	0.21	1262	1292	140	280	11818804
p19s15	0.66	1300	1400	438	467	5159242
p23s15	0.70	1417	1633	579	682	3897943
p11s11	0.25	1253	1307	-253	-147	8908265
p11s7	0.70	1304	1341	-552	-488	10716714
p7s7	0.64	1312	1423	-720	-640	6235813
p15s11	0.72	1300	1500	0	38	1130921

Table A.2: Right hand side mirror pairs, showing the reconstruction efficiency, the x and y co-ordinates in the plane of the RICH2 primary mirrors in mm of selected sub-areas and the number of events required to pass through the RICH2 to find the requisite data to carry out the alignment for that mirror pair.

Mirror pair	ϵ_{ϕ}^{reco}	X_{start}	X_{end}	Y_{start}	Y_{end}	Events required
p43s31	0.51	-150	-125	-150	-125	239105
p47s31	0.10	-42	4	0	200	214851
p47s35	0.63	-75	-50	400	467	131633
p51s35	0.54	-150	-75	625	650	897816
p51s39	0.61	-120	-60	875	900	4211715
p55s39	0.71	-100	-60	1032	1105	3229475
p39s31	0.22	-40	-10	-176	-120	117364
p39s27	0.63	-50	-25	-493	-447	218830
p35s27	0.48	-130	-70	-690	-625	511605
p35s23	0.52	-162	-126	-950	-820	1716746
p31s23	0.75	-50	-25	-1175	-1012	2663169
p43s30	0.70	-360	-330	-43	43	7170
p46s30	0.20	-430	-400	136	221	233243
p46s34	0.63	-425	-400	373	419	322602
p50s34	0.46	-550	-520	625	650	5832426
p50s38	0.44	-520	-490	850	950	3986547
p54s38	0.71	-500	-450	1018	1064	3213947
p38s30	0.28	-430	-400	-260	-120	104618
p38s26	0.61	-453	-418	-484	-456	439348
p34s26	0.46	-500	-475	-692	-656	3558945
p34s22	0.40	-520	-400	-930	-780	1007402
p30s22	0.75	-475	-450	-1280	-1100	1906672
p42s30	0.55	-500	-475	-50	250	36237
p42s29	0.68	-775	-750	-93	-7	728171
p45s29	0.23	-850	-825	100	300	2467061
p45s33	0.61	-875	-850	490	520	5251669
p49s33	0.54	-920	-890	690	750	8086956
p49s37	0.27	-950	-800	850	950	5211899
p53s37	0.75	-900	-750	1052	1138	1989434
p49s36	0.04	-1250	-1100	900	1050	129523886
p52s36	0.72	-1433	-1347	1052	1138	12771104
p37s29	0.37	-825	-800	-260	-120	1573585
p37s25	0.55	-873	-827	-568	-531	2694911
p33s25	0.56	-925	-900	-697	-662	11355699
p33s21	0.23	-1000	-975	-975	-900	54156625
p29s21	0.74	-933	-898	-1352	-1136	3652171
p33s20	0.05	-1250	-1100	-1050	-850	115160670
p28s20	0.76	-1433	-1289	-1300	-1155	7637979
p41s29	0.70	-925	-900	-20	130	238887
p41s28	0.57	-1220	-1190	-2	33	6430414
p44s28	0.21	-1288	-1247	140	280	10957945
p44s32	0.65	-1350	-1175	496	525	6083721
p48s32	0.60	-1460	-1200	613	728	2924575
p36s28	0.31	-1280	-1253	-200	-40	12049602
p36s24	0.67	-1385	-1335	-488	-424	8210445
p32s24	0.64	-1541	-1456	-650	-600	19485098
p40s28	0.76	-1420	-1100	0	112	311224

Appendix B

Optimisation of Selection Criteria

In order to tune the selection criteria to best optimise the signal, the statistical significance [100] of the signal was utilised, defined as

$$Sig = \frac{N_{sig}}{\sqrt{N_{sig} + N_{bkg}}} \tag{B.1}$$

where N_{sig} is the number of signal J/ψ and N_{bkg} is the number of background particles.

The significance was calculated using a data sample of 1 M single J/ψ, collected with a TCK of 0x5A0032; Monte Carlo was not utilised, as the full background in the MC sample is not generated. The values of N_{sig} and N_{bkg} were extracted from a fit to the J/ψ invariant mass distribution, using a double Crystal Ball function for the signal and an exponential function for the background.

The selection criteria, listed in Sec. 4.5, were applied with anstanz values, except for the selection criteria of interest, which was varied and the statistical significance was calculated. The optimum value of the selection criteria of interest was extracted, which corresponded to the selection value with the highest statistical significance. The process was repeated again using the optimum values extracted as the new anstanz values of the selection criteria.

Fig. B.1 shows the statistical significance as a function of the P_{NNMu} selection criteria, with Fig. B.2, Fig. B.3 and Fig. B.5 showing respectively, the statistical significance as a function of the P_{ghost}, $\chi^2_{DTF-J/\psi}$ and $\chi^2_{tr}/nDoF$ selection criteria. The values of the optimum selection criteria can be seen in Table. 4.4. Fig. B.5 shows the selection criteria of the quality of the J/ψ vertex, $\chi^2_{J/\psi}$. The significance is not improved by tightening this selection criteria above the lose selection of $\chi^2_{J/\psi} < 20$ that is carried out in the stripping line. The values of the optimised selection criteria are shown in Table. B.1.

Table B.1: Optimised selection criteria.

Selection Criterion
$\chi^2_{tr}/nDoF < 2.1$
$\mathrm{P}_{NNMu} > 0.4$
$\chi^2_{VX} < 20$
$\mathrm{P}_{ghost} < 0.2$
$\chi^2_{DTF-J/\psi}/nDoF < 12.5$

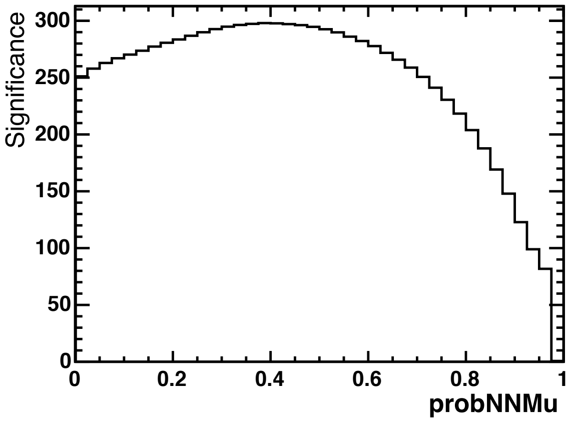

Figure B.1: Statistical significance as a function of the probNNMu selection criteria

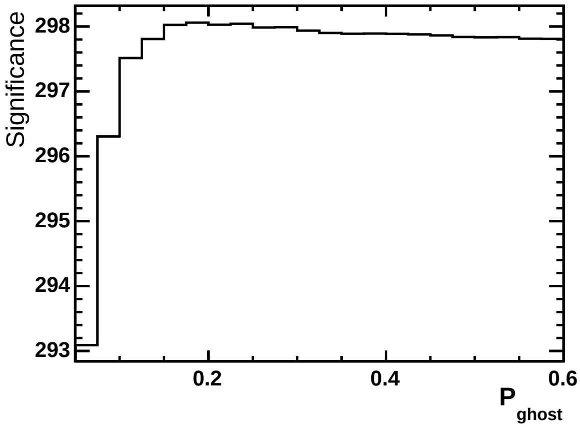

Figure B.2: Statistical significance as a function of the P_{ghost} selection criteria

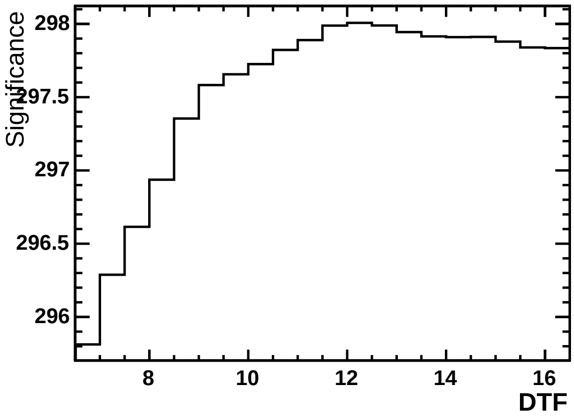

Figure B.3: Statistical significance as a function of the $\chi^2_{DTF-J/\psi}$ selection criteria

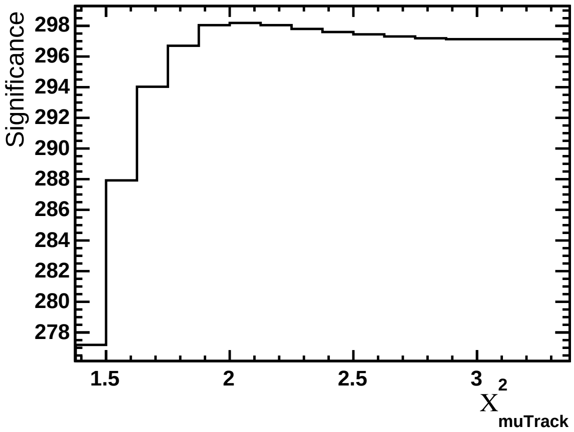

Figure B.4: Statistical significance as a function of the $\chi^2_{tr}/nDoF$ selection criteria

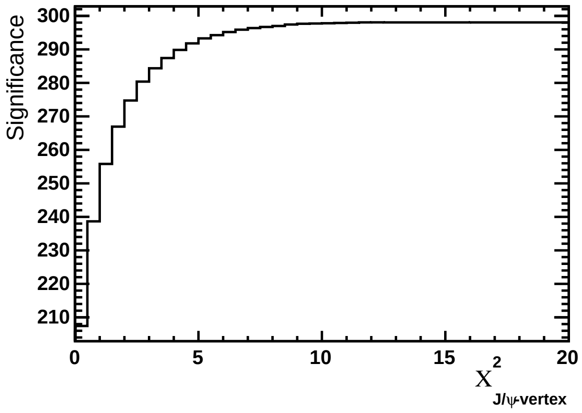

Figure B.5: Statistical significance as a function of the $\chi^2_{J/\psi}$ selection criteria

Appendix C

Efficiency by TCK

C.1 Trigger Efficiency

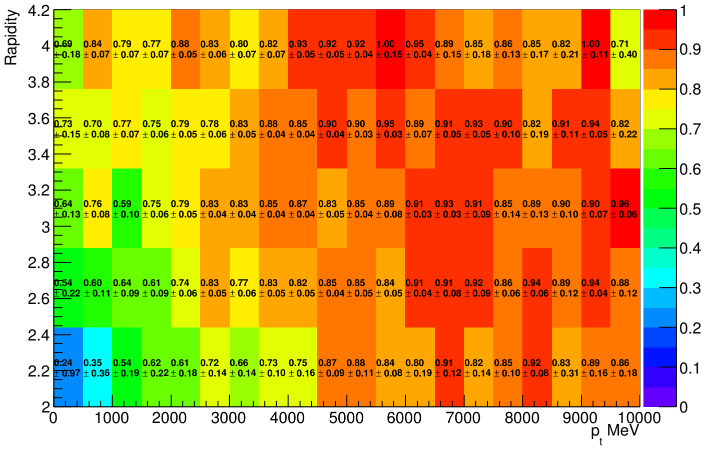

0.69 ± 0.18	0.84 ± 0.07	0.79 ± 0.07	0.77 ± 0.07	0.88 ± 0.05	0.83 ± 0.06	0.80 ± 0.07	0.82 ± 0.07	0.93 ± 0.05	0.92 ± 0.05	0.92 ± 0.04	1.00 ± 0.15	0.95 ± 0.04	0.89 ± 0.15	0.85 ± 0.18	0.86 ± 0.13	0.85 ± 0.17	0.82 ± 0.21	1.00 ± 0.11	0.71 ± 0.40
0.73 ± 0.15	0.70 ± 0.08	0.77 ± 0.07	0.75 ± 0.06	0.79 ± 0.05	0.78 ± 0.06	0.83 ± 0.05	0.88 ± 0.04	0.85 ± 0.04	0.90 ± 0.04	0.90 ± 0.03	0.95 ± 0.03	0.89 ± 0.07	0.91 ± 0.05	0.93 ± 0.05	0.90 ± 0.10	0.82 ± 0.19	0.91 ± 0.11	0.94 ± 0.05	0.82 ± 0.22
0.64 ± 0.13	0.76 ± 0.08	0.59 ± 0.10	0.75 ± 0.06	0.79 ± 0.05	0.83 ± 0.04	0.83 ± 0.04	0.85 ± 0.04	0.87 ± 0.04	0.83 ± 0.05	0.85 ± 0.04	0.89 ± 0.08	0.91 ± 0.03	0.93 ± 0.03	0.91 ± 0.09	0.85 ± 0.14	0.89 ± 0.13	0.90 ± 0.10	0.90 ± 0.07	0.96 ± 0.06
0.54 ± 0.22	0.60 ± 0.11	0.64 ± 0.09	0.61 ± 0.09	0.74 ± 0.06	0.83 ± 0.05	0.77 ± 0.06	0.83 ± 0.05	0.82 ± 0.05	0.85 ± 0.04	0.85 ± 0.05	0.84 ± 0.05	0.91 ± 0.04	0.91 ± 0.08	0.92 ± 0.09	0.86 ± 0.06	0.94 ± 0.06	0.89 ± 0.12	0.94 ± 0.04	0.88 ± 0.12
0.24 ± 0.97	0.35 ± 0.36	0.54 ± 0.19	0.62 ± 0.22	0.61 ± 0.18	0.72 ± 0.14	0.66 ± 0.14	0.73 ± 0.10	0.75 ± 0.16	0.87 ± 0.09	0.88 ± 0.11	0.84 ± 0.08	0.80 ± 0.19	0.91 ± 0.12	0.82 ± 0.14	0.85 ± 0.10	0.92 ± 0.08	0.83 ± 0.31	0.89 ± 0.16	0.86 ± 0.18

(a) 0x5A0032 magnet up.

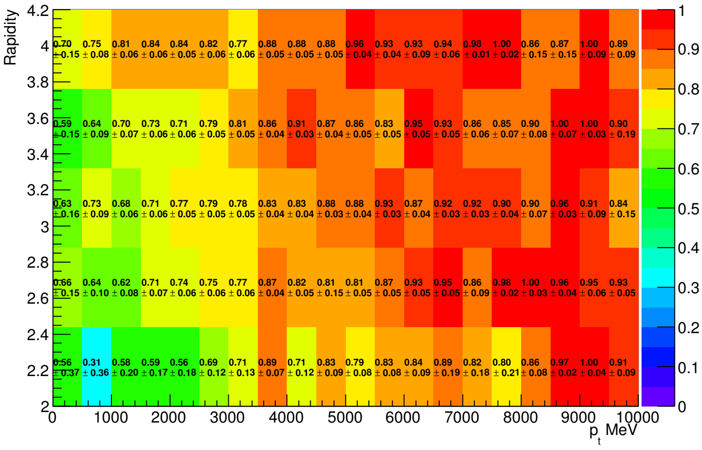

0.70 ± 0.15	0.75 ± 0.08	0.81 ± 0.06	0.84 ± 0.06	0.84 ± 0.05	0.82 ± 0.06	0.77 ± 0.06	0.88 ± 0.05	0.88 ± 0.05	0.88 ± 0.05	0.96 ± 0.04	0.93 ± 0.04	0.93 ± 0.09	0.94 ± 0.06	0.98 ± 0.01	1.00 ± 0.02	0.86 ± 0.15	0.87 ± 0.15	1.00 ± 0.09	0.89 ± 0.09
0.59 ± 0.15	0.64 ± 0.09	0.70 ± 0.07	0.73 ± 0.06	0.71 ± 0.06	0.79 ± 0.05	0.81 ± 0.05	0.86 ± 0.04	0.91 ± 0.03	0.87 ± 0.04	0.86 ± 0.05	0.83 ± 0.05	0.95 ± 0.05	0.93 ± 0.05	0.86 ± 0.06	0.85 ± 0.07	0.90 ± 0.08	1.00 ± 0.07	1.00 ± 0.03	0.90 ± 0.19
0.63 ± 0.16	0.73 ± 0.09	0.68 ± 0.06	0.71 ± 0.06	0.77 ± 0.05	0.79 ± 0.05	0.78 ± 0.05	0.83 ± 0.04	0.83 ± 0.04	0.88 ± 0.03	0.88 ± 0.04	0.93 ± 0.03	0.87 ± 0.04	0.92 ± 0.03	0.92 ± 0.03	0.90 ± 0.04	0.90 ± 0.07	0.96 ± 0.03	0.91 ± 0.09	0.84 ± 0.15
0.66 ± 0.15	0.64 ± 0.10	0.62 ± 0.08	0.71 ± 0.07	0.74 ± 0.06	0.75 ± 0.06	0.77 ± 0.06	0.87 ± 0.04	0.82 ± 0.05	0.81 ± 0.15	0.81 ± 0.05	0.87 ± 0.05	0.93 ± 0.05	0.95 ± 0.05	0.86 ± 0.09	0.98 ± 0.02	1.00 ± 0.03	0.96 ± 0.04	0.95 ± 0.06	0.93 ± 0.05
0.56 ± 0.37	0.31 ± 0.36	0.58 ± 0.20	0.59 ± 0.17	0.56 ± 0.18	0.69 ± 0.12	0.71 ± 0.13	0.89 ± 0.07	0.71 ± 0.12	0.83 ± 0.09	0.79 ± 0.08	0.83 ± 0.08	0.84 ± 0.09	0.89 ± 0.19	0.82 ± 0.18	0.80 ± 0.21	0.86 ± 0.08	0.97 ± 0.02	1.00 ± 0.04	0.91 ± 0.09

(b) 0x5A0032 magnet down.

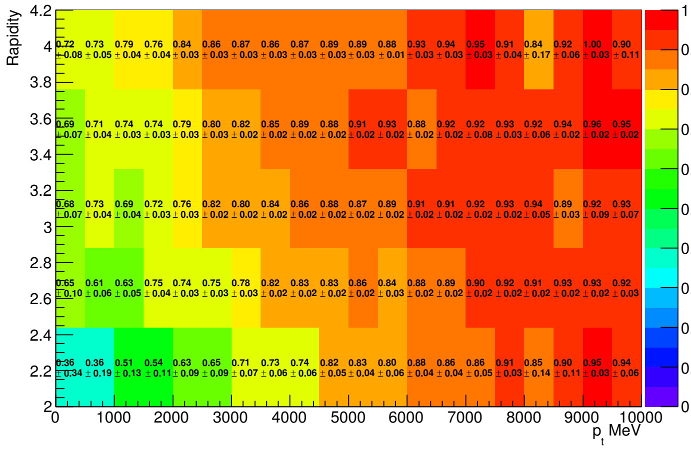

(c) 0x6D0032 magnet down.

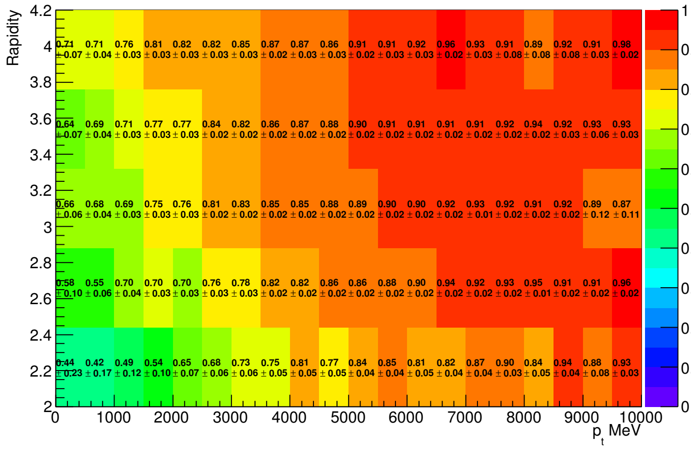

(d) 0x730035 magnet up.

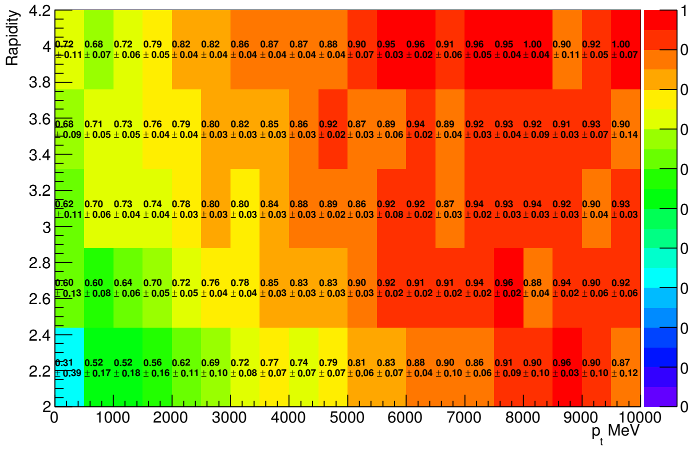

(e) 0x730035 magnet down.

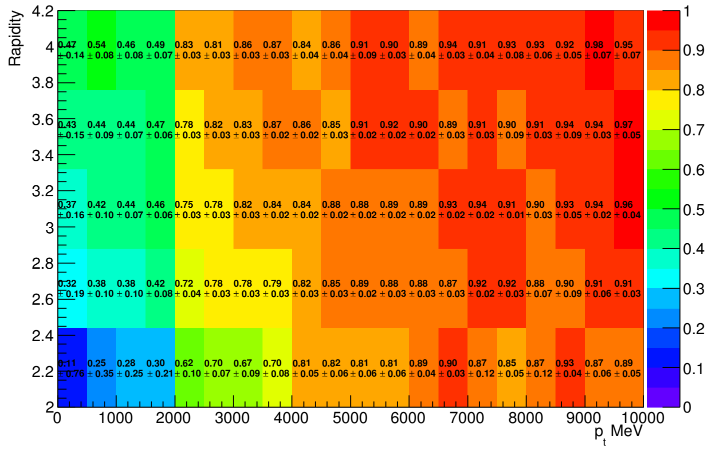

(f) 0x760037 magnet up.

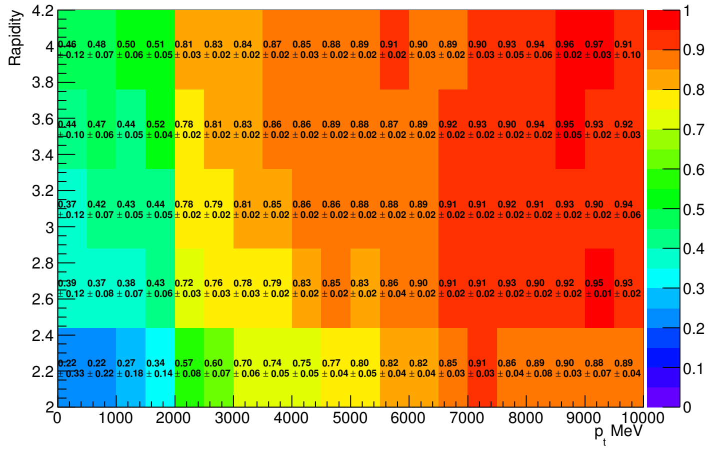

(g) 0x760037 magnet down.

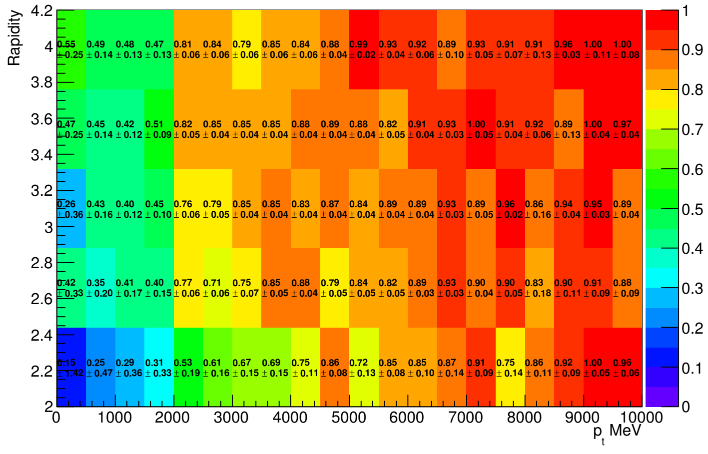

(h) 0x790037 magnet Up.

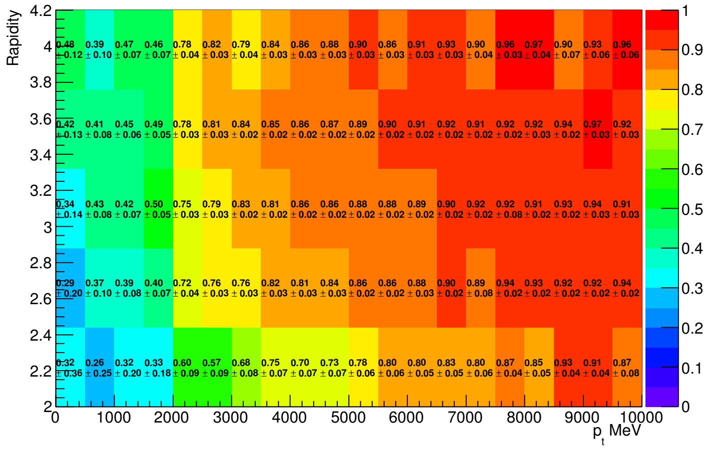

(i) 0x790038 magnet up.

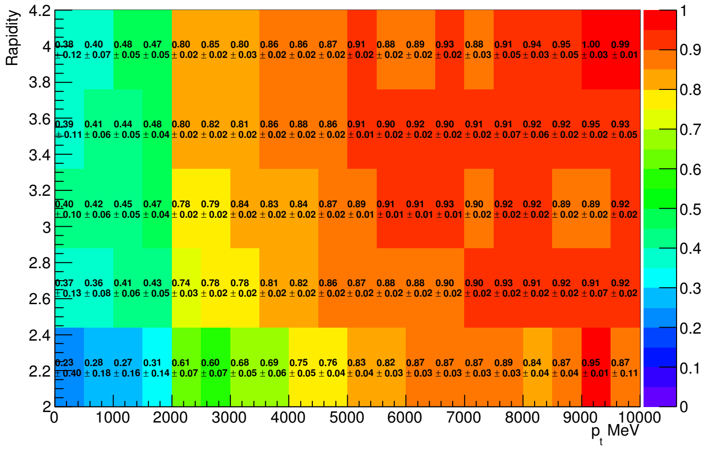

(j) 0x790038 magnet down.

Figure C.0: The trigger efficiency by TCK.

C.2 MuPid Efficiency

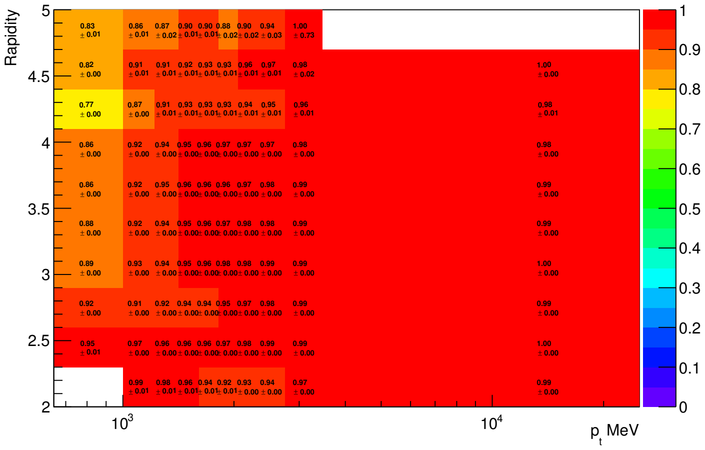

(a) 0x5A0032 magnet up.

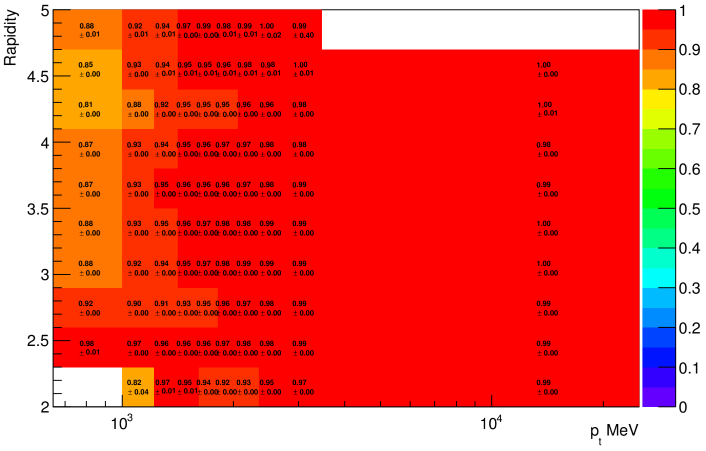

(b) 0x5A0032 magnet down.

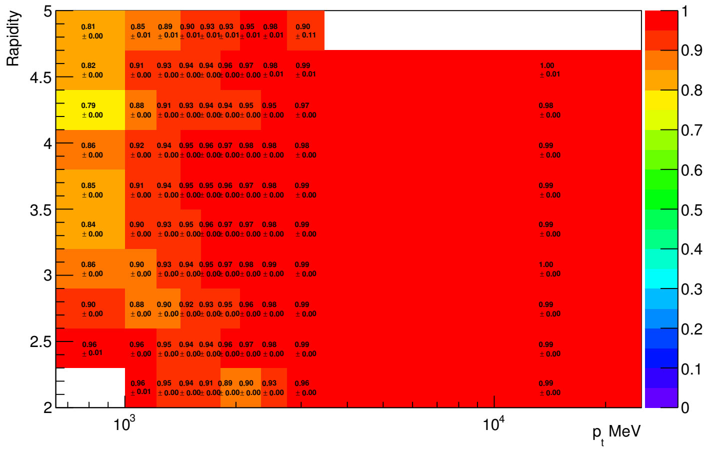

(c) 0x6D0032 magnet down.

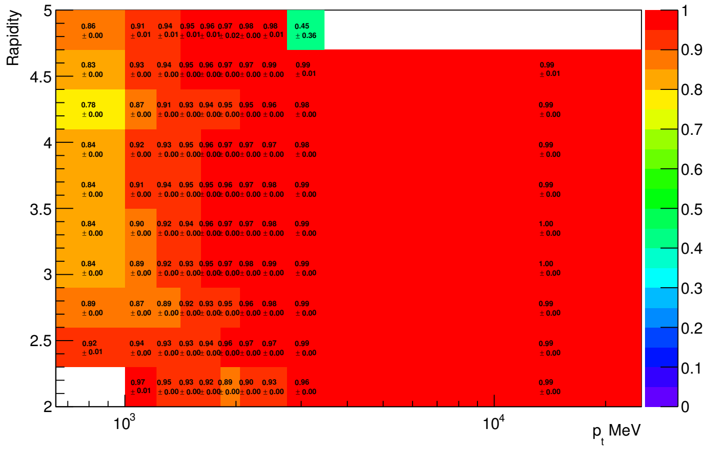

(d) 0x730035 magnet up.

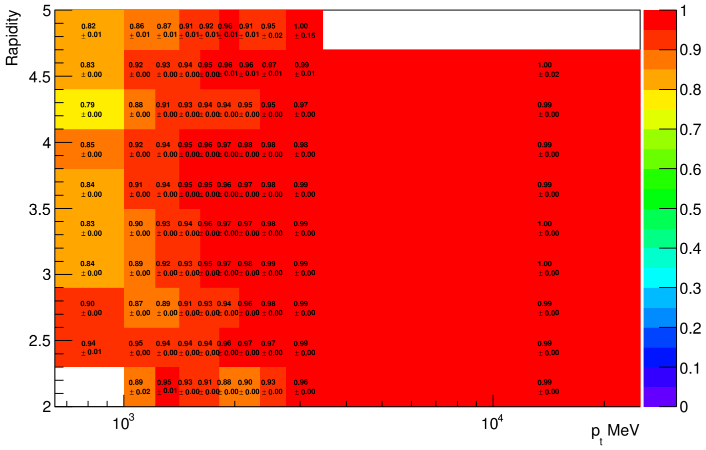

(e) 0x730035 magnet down.

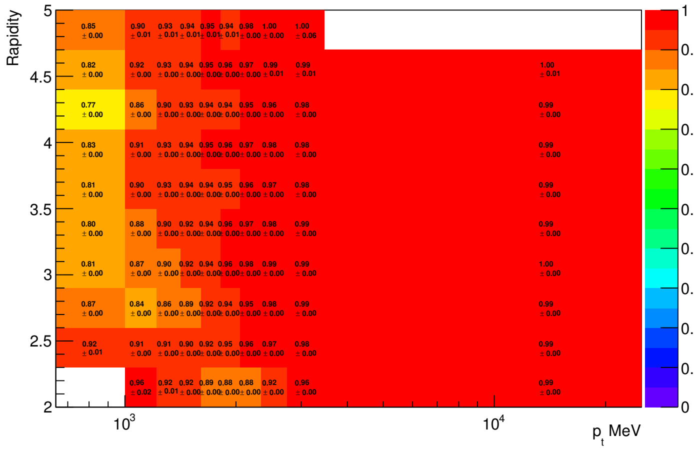

(f) 0x760037 magnet up.

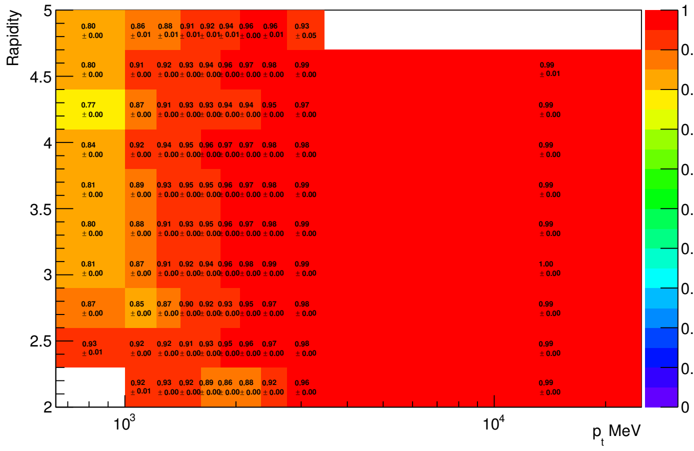

(g) 0x760037 magnet down.

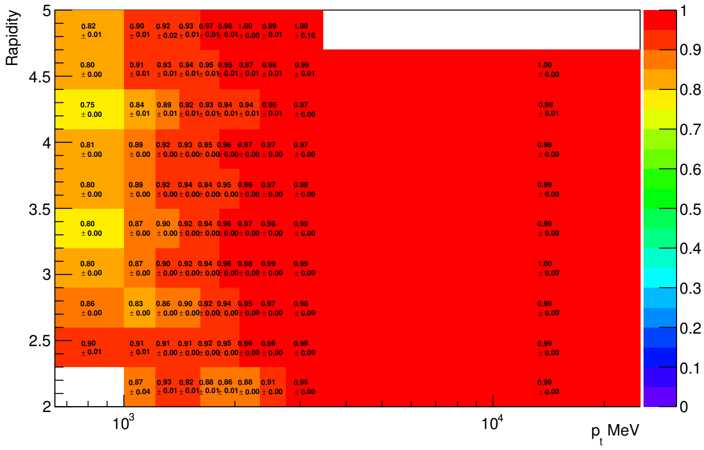

(h) 0x790037 magnet up.

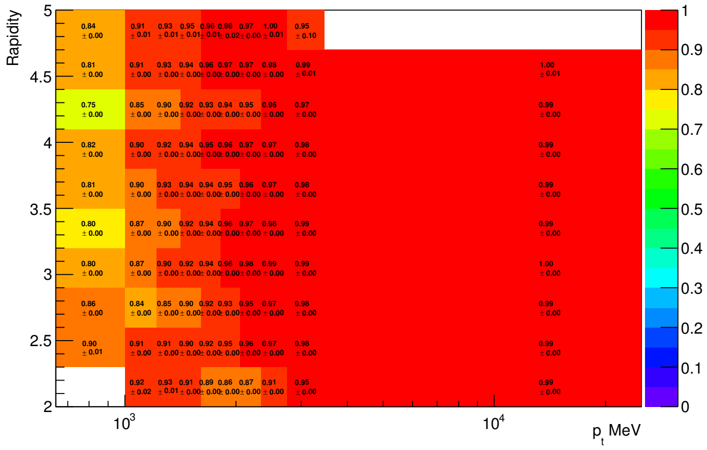

(i) 0x790038 magnet up.

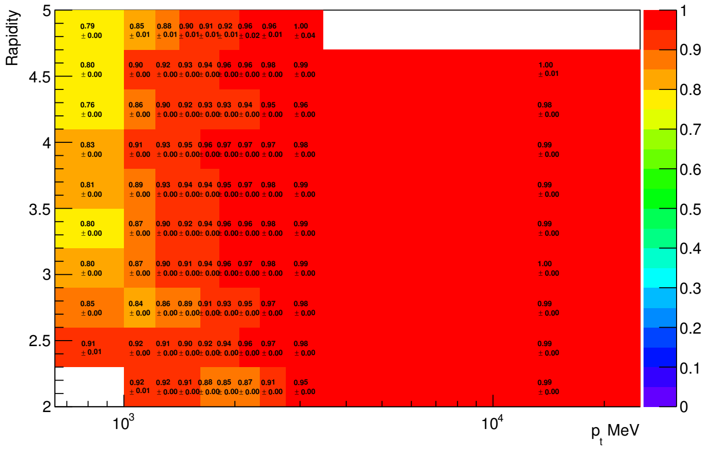

(j) 0x790038 magnet down.

Figure C.0: The MuPid efficiency for μ^+ by TCK.

C.3 Reconstruction and Selection Efficiency

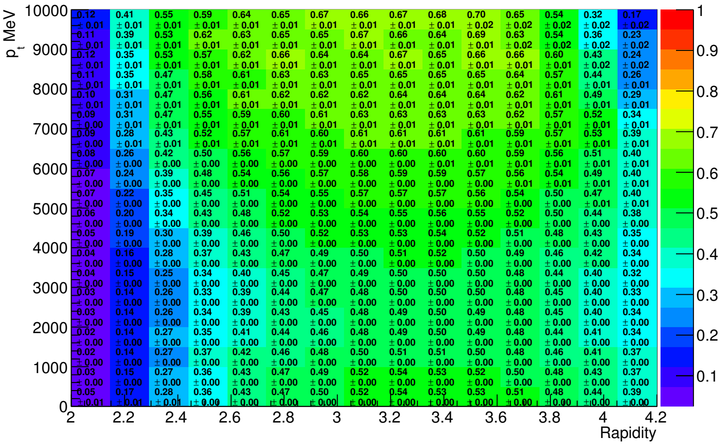

(a) 0x5A0032 magnet up.

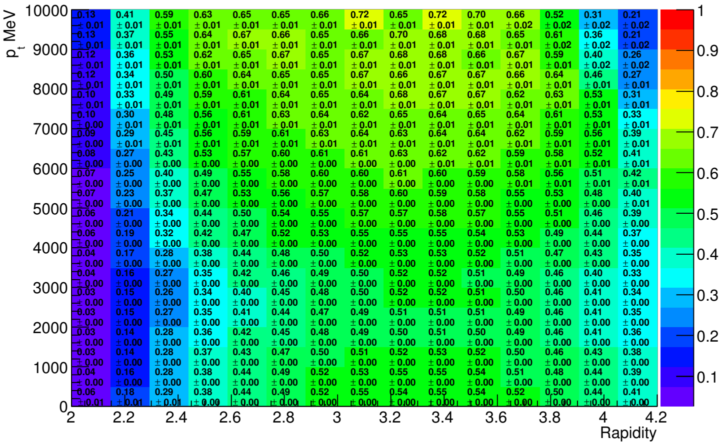

(b) 0x5A0032 magnet down.

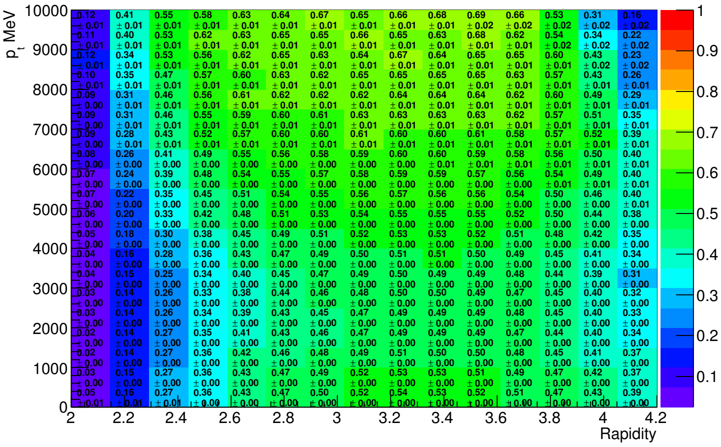

(c) 0x6D0032 magnet down.

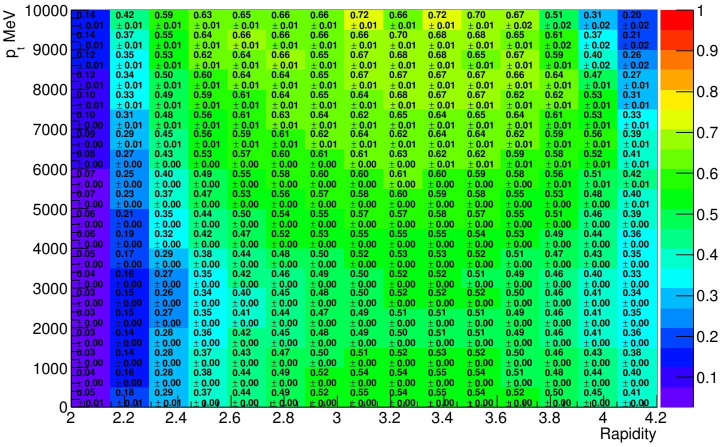

(d) 0x730035 magnet up.

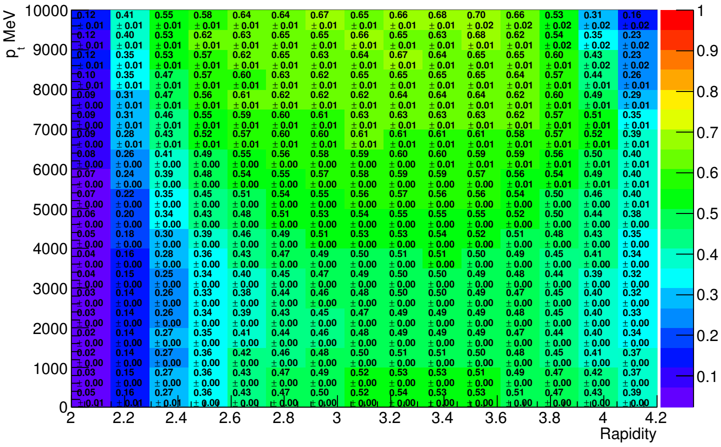

(e) 0x730035 magnet down.

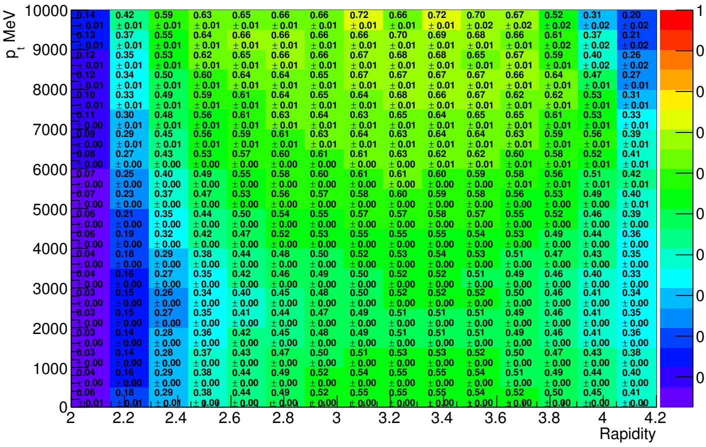

0.14 ± 0.01	0.42 ± 0.01	0.59 ± 0.01	0.63 ± 0.01	0.65 ± 0.01	0.66 ± 0.01	0.66 ± 0.01	0.72 ± 0.01	0.66 ± 0.01	0.72 ± 0.01	0.70 ± 0.02	0.67 ± 0.02	0.52 ± 0.02	0.31 ± 0.02	0.20 ± 0.02
0.13 ± 0.01	0.37 ± 0.01	0.55 ± 0.01	0.64 ± 0.01	0.66 ± 0.01	0.66 ± 0.01	0.66 ± 0.01	0.66 ± 0.01	0.70 ± 0.01	0.69 ± 0.01	0.68 ± 0.01	0.66 ± 0.01	0.61 ± 0.02	0.37 ± 0.02	0.21 ± 0.02
0.12 ± 0.01	0.35 ± 0.01	0.53 ± 0.01	0.62 ± 0.01	0.65 ± 0.01	0.66 ± 0.01	0.66 ± 0.01	0.67 ± 0.01	0.68 ± 0.01	0.68 ± 0.01	0.65 ± 0.01	0.67 ± 0.01	0.59 ± 0.01	0.40 ± 0.02	0.26 ± 0.02
0.12 ± 0.01	0.34 ± 0.01	0.50 ± 0.01	0.60 ± 0.01	0.64 ± 0.01	0.64 ± 0.01	0.65 ± 0.01	0.67 ± 0.01	0.67 ± 0.01	0.67 ± 0.01	0.67 ± 0.01	0.66 ± 0.01	0.64 ± 0.01	0.47 ± 0.01	0.27 ± 0.01
0.10 ± 0.01	0.33 ± 0.01	0.49 ± 0.01	0.59 ± 0.01	0.61 ± 0.01	0.64 ± 0.01	0.65 ± 0.01	0.64 ± 0.01	0.68 ± 0.01	0.66 ± 0.01	0.67 ± 0.01	0.62 ± 0.01	0.62 ± 0.01	0.53 ± 0.01	0.31 ± 0.01
0.11 ± 0.00	0.30 ± 0.01	0.48 ± 0.01	0.56 ± 0.01	0.61 ± 0.01	0.63 ± 0.01	0.64 ± 0.01	0.63 ± 0.01	0.65 ± 0.01	0.64 ± 0.01	0.65 ± 0.01	0.65 ± 0.01	0.61 ± 0.01	0.53 ± 0.01	0.33 ± 0.01
0.09 ± 0.00	0.29 ± 0.01	0.45 ± 0.01	0.56 ± 0.01	0.59 ± 0.01	0.61 ± 0.01	0.63 ± 0.01	0.64 ± 0.01	0.63 ± 0.01	0.64 ± 0.01	0.64 ± 0.01	0.63 ± 0.01	0.59 ± 0.01	0.56 ± 0.01	0.39 ± 0.01
0.08 ± 0.00	0.27 ± 0.00	0.43 ± 0.00	0.53 ± 0.00	0.57 ± 0.00	0.60 ± 0.00	0.61 ± 0.00	0.61 ± 0.00	0.63 ± 0.00	0.62 ± 0.01	0.62 ± 0.01	0.60 ± 0.01	0.58 ± 0.01	0.52 ± 0.01	0.41 ± 0.01
0.07 ± 0.00	0.25 ± 0.00	0.40 ± 0.00	0.49 ± 0.00	0.55 ± 0.00	0.58 ± 0.00	0.60 ± 0.00	0.61 ± 0.00	0.61 ± 0.00	0.60 ± 0.00	0.59 ± 0.00	0.58 ± 0.01	0.56 ± 0.01	0.51 ± 0.01	0.42 ± 0.01
0.07 ± 0.00	0.23 ± 0.00	0.37 ± 0.00	0.47 ± 0.00	0.53 ± 0.00	0.56 ± 0.00	0.57 ± 0.00	0.58 ± 0.00	0.60 ± 0.00	0.59 ± 0.00	0.58 ± 0.00	0.56 ± 0.00	0.53 ± 0.00	0.49 ± 0.00	0.40 ± 0.01
0.06 ± 0.00	0.21 ± 0.00	0.35 ± 0.00	0.44 ± 0.00	0.50 ± 0.00	0.54 ± 0.00	0.55 ± 0.00	0.57 ± 0.00	0.57 ± 0.00	0.58 ± 0.00	0.57 ± 0.00	0.55 ± 0.00	0.52 ± 0.00	0.46 ± 0.00	0.39 ± 0.00
0.06 ± 0.00	0.19 ± 0.00	0.32 ± 0.00	0.42 ± 0.00	0.47 ± 0.00	0.52 ± 0.00	0.53 ± 0.00	0.55 ± 0.00	0.55 ± 0.00	0.55 ± 0.00	0.54 ± 0.00	0.53 ± 0.00	0.49 ± 0.00	0.44 ± 0.00	0.36 ± 0.00
0.04 ± 0.00	0.18 ± 0.00	0.29 ± 0.00	0.38 ± 0.00	0.44 ± 0.00	0.48 ± 0.00	0.50 ± 0.00	0.52 ± 0.00	0.53 ± 0.00	0.54 ± 0.00	0.53 ± 0.00	0.51 ± 0.00	0.47 ± 0.00	0.43 ± 0.00	0.35 ± 0.00
0.04 ± 0.00	0.16 ± 0.00	0.27 ± 0.00	0.35 ± 0.00	0.42 ± 0.00	0.46 ± 0.00	0.49 ± 0.00	0.50 ± 0.00	0.52 ± 0.00	0.52 ± 0.00	0.51 ± 0.00	0.49 ± 0.00	0.46 ± 0.00	0.40 ± 0.00	0.33 ± 0.00
0.03 ± 0.00	0.15 ± 0.00	0.26 ± 0.00	0.34 ± 0.00	0.40 ± 0.00	0.45 ± 0.00	0.48 ± 0.00	0.50 ± 0.00	0.52 ± 0.00	0.52 ± 0.00	0.52 ± 0.00	0.50 ± 0.00	0.46 ± 0.00	0.41 ± 0.00	0.34 ± 0.00
0.03 ± 0.00	0.15 ± 0.00	0.27 ± 0.00	0.35 ± 0.00	0.41 ± 0.00	0.44 ± 0.00	0.47 ± 0.00	0.49 ± 0.00	0.51 ± 0.00	0.51 ± 0.00	0.51 ± 0.00	0.49 ± 0.00	0.46 ± 0.00	0.41 ± 0.00	0.35 ± 0.00
0.03 ± 0.00	0.14 ± 0.00	0.28 ± 0.00	0.36 ± 0.00	0.42 ± 0.00	0.45 ± 0.00	0.48 ± 0.00	0.49 ± 0.00	0.51 ± 0.00	0.51 ± 0.00	0.51 ± 0.00	0.49 ± 0.00	0.46 ± 0.00	0.41 ± 0.00	0.36 ± 0.00
0.03 ± 0.00	0.14 ± 0.00	0.28 ± 0.00	0.37 ± 0.00	0.43 ± 0.00	0.47 ± 0.00	0.50 ± 0.00	0.51 ± 0.00	0.53 ± 0.00	0.53 ± 0.00	0.52 ± 0.00	0.50 ± 0.00	0.47 ± 0.00	0.43 ± 0.00	0.38 ± 0.00
0.04 ± 0.00	0.16 ± 0.00	0.29 ± 0.00	0.38 ± 0.00	0.44 ± 0.00	0.49 ± 0.00	0.52 ± 0.00	0.54 ± 0.00	0.55 ± 0.00	0.55 ± 0.00	0.54 ± 0.00	0.51 ± 0.00	0.49 ± 0.00	0.44 ± 0.00	0.40 ± 0.00
0.06 ± 0.01	0.18 ± 0.01	0.29 ± 0.01	0.38 ± 0.00	0.44 ± 0.00	0.49 ± 0.00	0.52 ± 0.00	0.55 ± 0.00	0.55 ± 0.00	0.55 ± 0.00	0.54 ± 0.00	0.52 ± 0.00	0.50 ± 0.00	0.45 ± 0.00	0.41 ± 0.00

(f) 0x760037 magnet up.

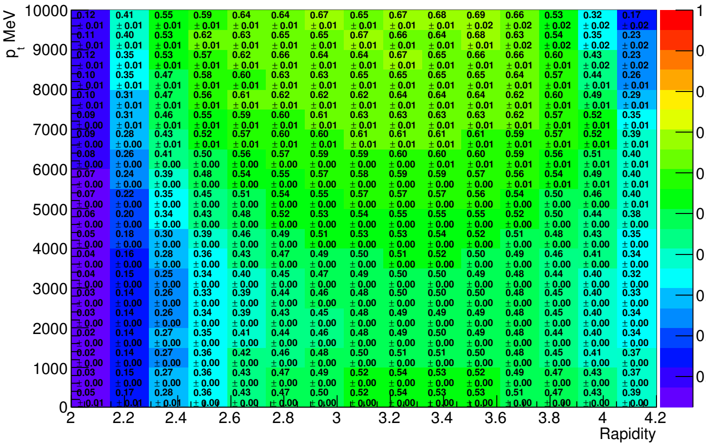

0.12 ± 0.01	0.41 ± 0.01	0.55 ± 0.01	0.59 ± 0.01	0.64 ± 0.01	0.64 ± 0.01	0.67 ± 0.01	0.65 ± 0.01	0.67 ± 0.01	0.68 ± 0.01	0.69 ± 0.02	0.66 ± 0.02	0.53 ± 0.02	0.32 ± 0.02	0.17 ± 0.02
0.11 ± 0.01	0.40 ± 0.01	0.53 ± 0.01	0.62 ± 0.01	0.63 ± 0.01	0.65 ± 0.01	0.65 ± 0.01	0.67 ± 0.01	0.66 ± 0.01	0.64 ± 0.01	0.68 ± 0.01	0.63 ± 0.02	0.54 ± 0.02	0.35 ± 0.02	0.23 ± 0.02
0.12 ± 0.01	0.35 ± 0.01	0.53 ± 0.01	0.57 ± 0.01	0.62 ± 0.01	0.66 ± 0.01	0.64 ± 0.01	0.64 ± 0.01	0.67 ± 0.01	0.65 ± 0.01	0.66 ± 0.01	0.66 ± 0.01	0.60 ± 0.01	0.43 ± 0.02	0.23 ± 0.02
0.10 ± 0.01	0.35 ± 0.01	0.47 ± 0.01	0.58 ± 0.01	0.60 ± 0.01	0.63 ± 0.01	0.63 ± 0.01	0.65 ± 0.01	0.65 ± 0.01	0.65 ± 0.01	0.65 ± 0.01	0.64 ± 0.01	0.57 ± 0.01	0.44 ± 0.01	0.26 ± 0.01
0.10 ± 0.01	0.31 ± 0.01	0.47 ± 0.01	0.56 ± 0.01	0.61 ± 0.01	0.62 ± 0.01	0.62 ± 0.01	0.62 ± 0.01	0.64 ± 0.01	0.64 ± 0.01	0.64 ± 0.01	0.62 ± 0.01	0.60 ± 0.01	0.49 ± 0.01	0.29 ± 0.01
0.09 ± 0.00	0.31 ± 0.01	0.46 ± 0.01	0.55 ± 0.01	0.59 ± 0.01	0.60 ± 0.01	0.61 ± 0.01	0.63 ± 0.01	0.63 ± 0.01	0.63 ± 0.01	0.63 ± 0.01	0.62 ± 0.01	0.57 ± 0.01	0.52 ± 0.01	0.35 ± 0.01
0.09 ± 0.00	0.28 ± 0.00	0.43 ± 0.01	0.52 ± 0.01	0.57 ± 0.01	0.60 ± 0.01	0.60 ± 0.01	0.61 ± 0.01	0.61 ± 0.01	0.61 ± 0.01	0.61 ± 0.01	0.59 ± 0.01	0.57 ± 0.01	0.52 ± 0.01	0.39 ± 0.01
0.08 ± 0.00	0.26 ± 0.00	0.41 ± 0.00	0.50 ± 0.00	0.56 ± 0.00	0.57 ± 0.00	0.59 ± 0.00	0.59 ± 0.00	0.60 ± 0.00	0.60 ± 0.01	0.60 ± 0.01	0.59 ± 0.01	0.56 ± 0.01	0.51 ± 0.01	0.40 ± 0.01
0.07 ± 0.00	0.24 ± 0.00	0.39 ± 0.00	0.48 ± 0.00	0.54 ± 0.00	0.55 ± 0.00	0.57 ± 0.00	0.58 ± 0.00	0.59 ± 0.00	0.59 ± 0.00	0.57 ± 0.00	0.56 ± 0.01	0.54 ± 0.01	0.49 ± 0.01	0.40 ± 0.01
0.07 ± 0.00	0.22 ± 0.00	0.35 ± 0.00	0.45 ± 0.00	0.51 ± 0.00	0.54 ± 0.00	0.55 ± 0.00	0.57 ± 0.00	0.57 ± 0.00	0.57 ± 0.00	0.56 ± 0.00	0.54 ± 0.00	0.50 ± 0.00	0.46 ± 0.00	0.40 ± 0.01
0.06 ± 0.00	0.20 ± 0.00	0.34 ± 0.00	0.43 ± 0.00	0.48 ± 0.00	0.52 ± 0.00	0.53 ± 0.00	0.54 ± 0.00	0.55 ± 0.00	0.55 ± 0.00	0.55 ± 0.00	0.52 ± 0.00	0.50 ± 0.00	0.44 ± 0.00	0.38 ± 0.00
0.05 ± 0.00	0.18 ± 0.00	0.30 ± 0.00	0.39 ± 0.00	0.46 ± 0.00	0.49 ± 0.00	0.51 ± 0.00	0.53 ± 0.00	0.53 ± 0.00	0.54 ± 0.00	0.52 ± 0.00	0.51 ± 0.00	0.48 ± 0.00	0.43 ± 0.00	0.35 ± 0.00
0.04 ± 0.00	0.16 ± 0.00	0.28 ± 0.00	0.36 ± 0.00	0.43 ± 0.00	0.47 ± 0.00	0.49 ± 0.00	0.50 ± 0.00	0.51 ± 0.00	0.52 ± 0.00	0.50 ± 0.00	0.49 ± 0.00	0.46 ± 0.00	0.41 ± 0.00	0.34 ± 0.00
0.04 ± 0.00	0.15 ± 0.00	0.25 ± 0.00	0.34 ± 0.00	0.40 ± 0.00	0.45 ± 0.00	0.47 ± 0.00	0.49 ± 0.00	0.50 ± 0.00	0.50 ± 0.00	0.49 ± 0.00	0.48 ± 0.00	0.44 ± 0.00	0.40 ± 0.00	0.32 ± 0.00
0.03 ± 0.00	0.14 ± 0.00	0.26 ± 0.00	0.33 ± 0.00	0.39 ± 0.00	0.44 ± 0.00	0.46 ± 0.00	0.48 ± 0.00	0.50 ± 0.00	0.50 ± 0.00	0.50 ± 0.00	0.48 ± 0.00	0.45 ± 0.00	0.40 ± 0.00	0.33 ± 0.00
0.03 ± 0.00	0.14 ± 0.00	0.26 ± 0.00	0.34 ± 0.00	0.39 ± 0.00	0.43 ± 0.00	0.45 ± 0.00	0.48 ± 0.00	0.49 ± 0.00	0.49 ± 0.00	0.49 ± 0.00	0.48 ± 0.00	0.45 ± 0.00	0.40 ± 0.00	0.34 ± 0.00
0.02 ± 0.00	0.14 ± 0.00	0.27 ± 0.00	0.35 ± 0.00	0.41 ± 0.00	0.44 ± 0.00	0.46 ± 0.00	0.48 ± 0.00	0.49 ± 0.00	0.50 ± 0.00	0.49 ± 0.00	0.48 ± 0.00	0.44 ± 0.00	0.40 ± 0.00	0.34 ± 0.00
0.02 ± 0.00	0.14 ± 0.00	0.27 ± 0.00	0.36 ± 0.00	0.42 ± 0.00	0.46 ± 0.00	0.48 ± 0.00	0.50 ± 0.00	0.51 ± 0.00	0.51 ± 0.00	0.50 ± 0.00	0.48 ± 0.00	0.45 ± 0.00	0.41 ± 0.00	0.37 ± 0.00
0.03 ± 0.00	0.15 ± 0.00	0.27 ± 0.00	0.36 ± 0.00	0.43 ± 0.00	0.47 ± 0.00	0.49 ± 0.00	0.52 ± 0.00	0.54 ± 0.00	0.53 ± 0.00	0.52 ± 0.00	0.49 ± 0.00	0.47 ± 0.00	0.43 ± 0.00	0.37 ± 0.00
0.05 ± 0.01	0.17 ± 0.01	0.28 ± 0.01	0.36 ± 0.00	0.43 ± 0.00	0.47 ± 0.00	0.50 ± 0.00	0.52 ± 0.00	0.54 ± 0.00	0.53 ± 0.00	0.53 ± 0.00	0.51 ± 0.00	0.47 ± 0.00	0.43 ± 0.00	0.39 ± 0.00

(g) 0x760037 magnet down.

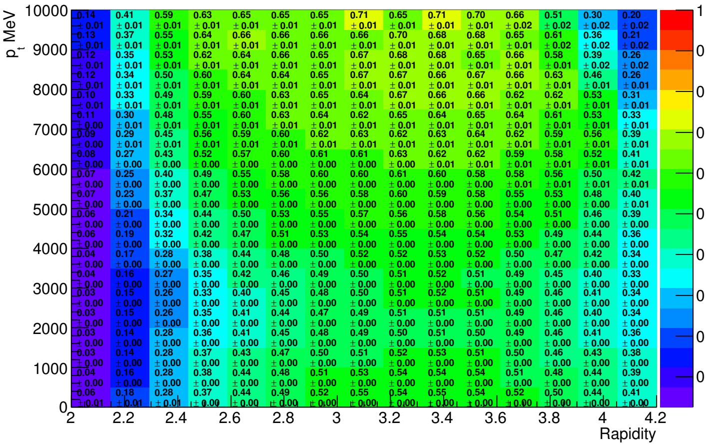

0.14 ± 0.01	0.41 ± 0.01	0.59 ± 0.01	0.63 ± 0.01	0.65 ± 0.01	0.65 ± 0.01	0.65 ± 0.01	0.71 ± 0.01	0.65 ± 0.01	0.71 ± 0.01	0.70 ± 0.01	0.66 ± 0.02	0.51 ± 0.02	0.30 ± 0.02	0.20 ± 0.02
0.13 ± 0.01	0.37 ± 0.01	0.55 ± 0.01	0.64 ± 0.01	0.66 ± 0.01	0.66 ± 0.01	0.66 ± 0.01	0.66 ± 0.01	0.70 ± 0.01	0.68 ± 0.01	0.68 ± 0.01	0.65 ± 0.01	0.61 ± 0.02	0.36 ± 0.02	0.21 ± 0.02
0.12 ± 0.01	0.35 ± 0.01	0.53 ± 0.01	0.62 ± 0.01	0.64 ± 0.01	0.66 ± 0.01	0.65 ± 0.01	0.67 ± 0.01	0.68 ± 0.01	0.68 ± 0.01	0.65 ± 0.01	0.66 ± 0.01	0.58 ± 0.01	0.39 ± 0.02	0.26 ± 0.02
0.12 ± 0.01	0.34 ± 0.01	0.50 ± 0.01	0.60 ± 0.01	0.64 ± 0.01	0.64 ± 0.01	0.65 ± 0.01	0.67 ± 0.01	0.67 ± 0.01	0.66 ± 0.01	0.67 ± 0.01	0.66 ± 0.01	0.63 ± 0.01	0.46 ± 0.01	0.26 ± 0.01
0.10 ± 0.01	0.33 ± 0.01	0.49 ± 0.01	0.59 ± 0.01	0.60 ± 0.01	0.63 ± 0.01	0.65 ± 0.01	0.64 ± 0.01	0.67 ± 0.01	0.66 ± 0.01	0.66 ± 0.01	0.62 ± 0.01	0.62 ± 0.01	0.53 ± 0.01	0.31 ± 0.01
0.11 ± 0.00	0.30 ± 0.01	0.48 ± 0.01	0.55 ± 0.01	0.60 ± 0.01	0.63 ± 0.01	0.64 ± 0.01	0.62 ± 0.01	0.65 ± 0.01	0.64 ± 0.01	0.65 ± 0.01	0.64 ± 0.01	0.61 ± 0.01	0.53 ± 0.01	0.33 ± 0.01
0.09 ± 0.00	0.29 ± 0.01	0.45 ± 0.01	0.56 ± 0.01	0.59 ± 0.01	0.60 ± 0.01	0.62 ± 0.01	0.63 ± 0.01	0.62 ± 0.01	0.63 ± 0.01	0.64 ± 0.01	0.62 ± 0.01	0.59 ± 0.01	0.56 ± 0.01	0.39 ± 0.01
0.08 ± 0.00	0.27 ± 0.00	0.43 ± 0.00	0.52 ± 0.00	0.57 ± 0.00	0.60 ± 0.00	0.61 ± 0.00	0.61 ± 0.00	0.63 ± 0.00	0.62 ± 0.01	0.62 ± 0.01	0.59 ± 0.01	0.58 ± 0.01	0.52 ± 0.01	0.41 ± 0.01
0.07 ± 0.00	0.25 ± 0.00	0.40 ± 0.00	0.49 ± 0.00	0.55 ± 0.00	0.58 ± 0.00	0.60 ± 0.00	0.60 ± 0.00	0.61 ± 0.00	0.60 ± 0.00	0.58 ± 0.00	0.58 ± 0.01	0.56 ± 0.01	0.50 ± 0.01	0.42 ± 0.01
0.07 ± 0.00	0.23 ± 0.00	0.37 ± 0.00	0.47 ± 0.00	0.53 ± 0.00	0.56 ± 0.00	0.56 ± 0.00	0.58 ± 0.00	0.60 ± 0.00	0.59 ± 0.00	0.58 ± 0.00	0.55 ± 0.00	0.53 ± 0.00	0.48 ± 0.00	0.40 ± 0.01
0.06 ± 0.00	0.21 ± 0.00	0.34 ± 0.00	0.44 ± 0.00	0.50 ± 0.00	0.53 ± 0.00	0.55 ± 0.00	0.57 ± 0.00	0.56 ± 0.00	0.58 ± 0.00	0.56 ± 0.00	0.54 ± 0.00	0.51 ± 0.00	0.46 ± 0.00	0.39 ± 0.00
0.06 ± 0.00	0.19 ± 0.00	0.32 ± 0.00	0.42 ± 0.00	0.47 ± 0.00	0.51 ± 0.00	0.53 ± 0.00	0.54 ± 0.00	0.55 ± 0.00	0.54 ± 0.00	0.54 ± 0.00	0.53 ± 0.00	0.49 ± 0.00	0.44 ± 0.00	0.36 ± 0.00
0.04 ± 0.00	0.17 ± 0.00	0.28 ± 0.00	0.38 ± 0.00	0.44 ± 0.00	0.48 ± 0.00	0.50 ± 0.00	0.52 ± 0.00	0.52 ± 0.00	0.53 ± 0.00	0.52 ± 0.00	0.50 ± 0.00	0.47 ± 0.00	0.42 ± 0.00	0.34 ± 0.00
0.04 ± 0.00	0.16 ± 0.00	0.27 ± 0.00	0.35 ± 0.00	0.42 ± 0.00	0.46 ± 0.00	0.49 ± 0.00	0.50 ± 0.00	0.51 ± 0.00	0.52 ± 0.00	0.51 ± 0.00	0.49 ± 0.00	0.45 ± 0.00	0.40 ± 0.00	0.33 ± 0.00
0.03 ± 0.00	0.15 ± 0.00	0.26 ± 0.00	0.33 ± 0.00	0.40 ± 0.00	0.45 ± 0.00	0.48 ± 0.00	0.50 ± 0.00	0.51 ± 0.00	0.52 ± 0.00	0.51 ± 0.00	0.49 ± 0.00	0.46 ± 0.00	0.41 ± 0.00	0.34 ± 0.00
0.03 ± 0.00	0.15 ± 0.00	0.26 ± 0.00	0.35 ± 0.00	0.41 ± 0.00	0.44 ± 0.00	0.47 ± 0.00	0.49 ± 0.00	0.51 ± 0.00	0.51 ± 0.00	0.51 ± 0.00	0.49 ± 0.00	0.46 ± 0.00	0.40 ± 0.00	0.34 ± 0.00
0.03 ± 0.00	0.14 ± 0.00	0.28 ± 0.00	0.36 ± 0.00	0.41 ± 0.00	0.45 ± 0.00	0.48 ± 0.00	0.49 ± 0.00	0.50 ± 0.00	0.51 ± 0.00	0.50 ± 0.00	0.49 ± 0.00	0.46 ± 0.00	0.41 ± 0.00	0.36 ± 0.00
0.03 ± 0.00	0.14 ± 0.00	0.28 ± 0.00	0.37 ± 0.00	0.43 ± 0.00	0.47 ± 0.00	0.50 ± 0.00	0.51 ± 0.00	0.52 ± 0.00	0.53 ± 0.00	0.51 ± 0.00	0.50 ± 0.00	0.46 ± 0.00	0.43 ± 0.00	0.38 ± 0.00
0.04 ± 0.00	0.16 ± 0.00	0.28 ± 0.00	0.38 ± 0.00	0.44 ± 0.00	0.48 ± 0.00	0.51 ± 0.00	0.53 ± 0.00	0.54 ± 0.00	0.54 ± 0.00	0.54 ± 0.00	0.51 ± 0.00	0.48 ± 0.00	0.44 ± 0.00	0.39 ± 0.00
0.06 ± 0.01	0.18 ± 0.01	0.28 ± 0.01	0.37 ± 0.00	0.44 ± 0.00	0.49 ± 0.00	0.52 ± 0.00	0.55 ± 0.00	0.54 ± 0.00	0.55 ± 0.00	0.54 ± 0.00	0.52 ± 0.00	0.50 ± 0.00	0.44 ± 0.00	0.41 ± 0.00

(h) 0x790037 Up.

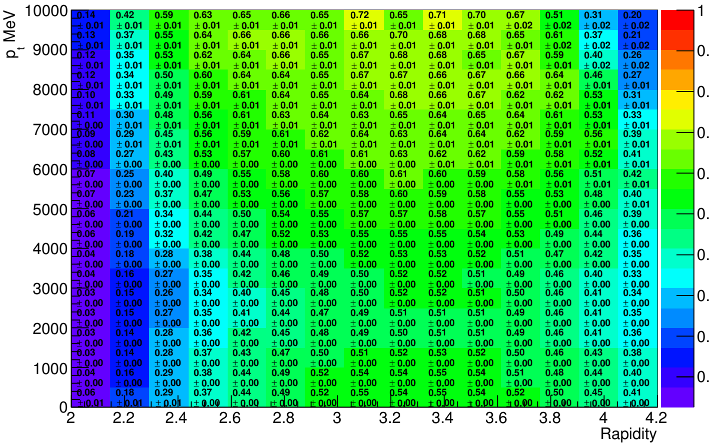

(i) 0x790038 magnet up.

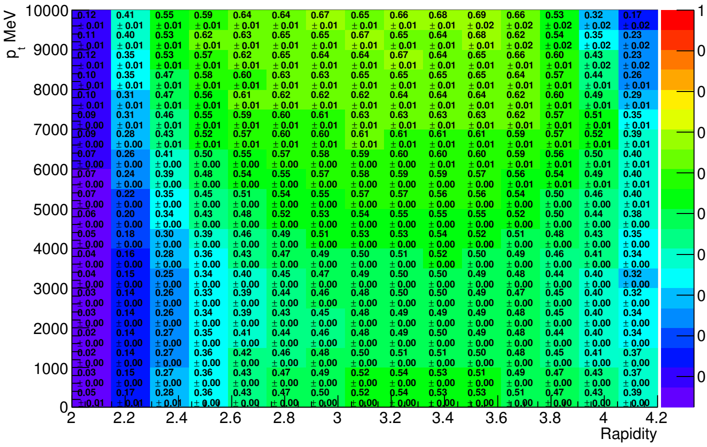

(j) 0x790038 magnet down.

Figure C.0: The reconstruction and selection efficiency by TCK.

Appendix D

Global Event Cuts

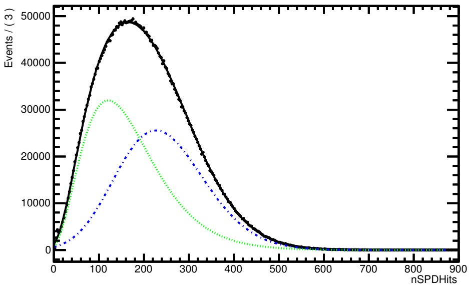

(a) Number of primary vertices = 1.

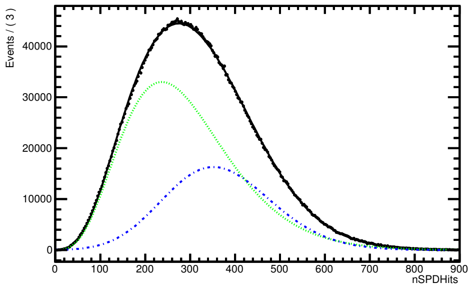

(b) Number of primary vertices = 2.

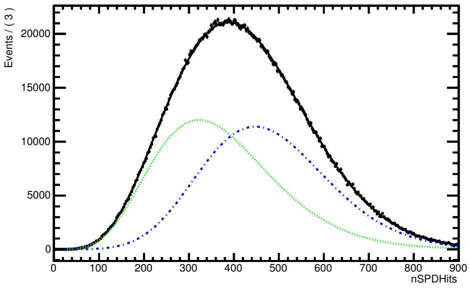

(c) Number of primary vertices = 3.

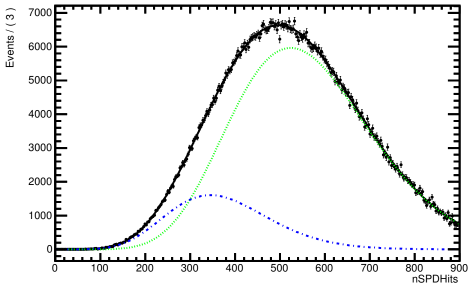

(d) Number of primary vertices = 4.

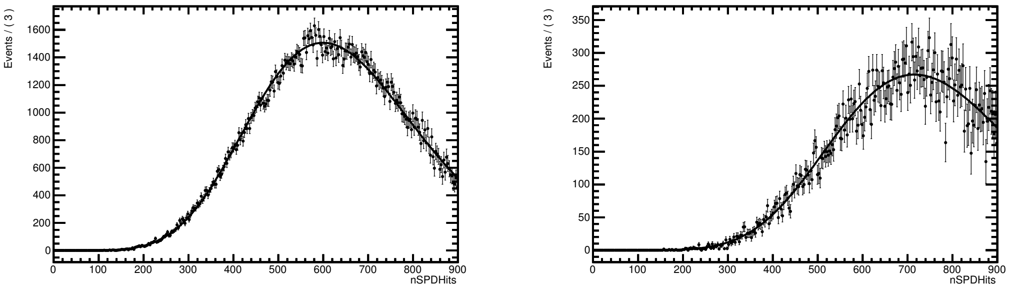

(e) Number of primary vertices = 5.

(f) Number of primary vertices = 6.

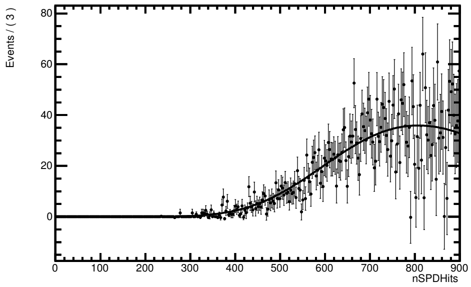

(g) Number of primary vertices = 7.

Figure D.0: The **L0Dimuon** background subtracted SPD multiplicity distribution fitted with the sum of two gamma functions for TCK = 0x760037.

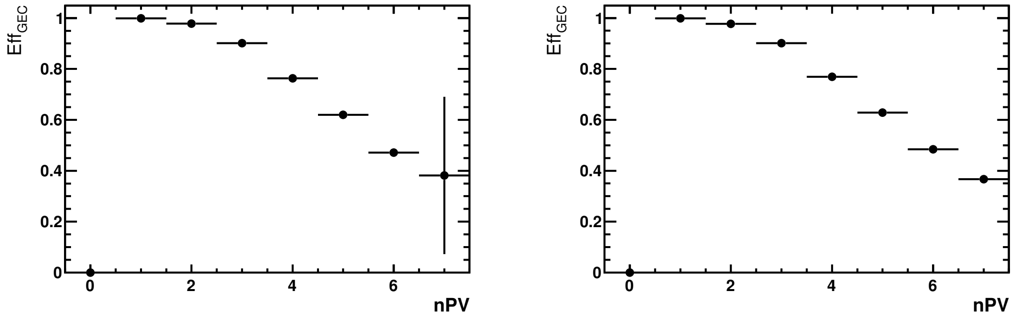

(a) 0x5A0032 magnet up.

(b) 0x5A0032 magnet down.

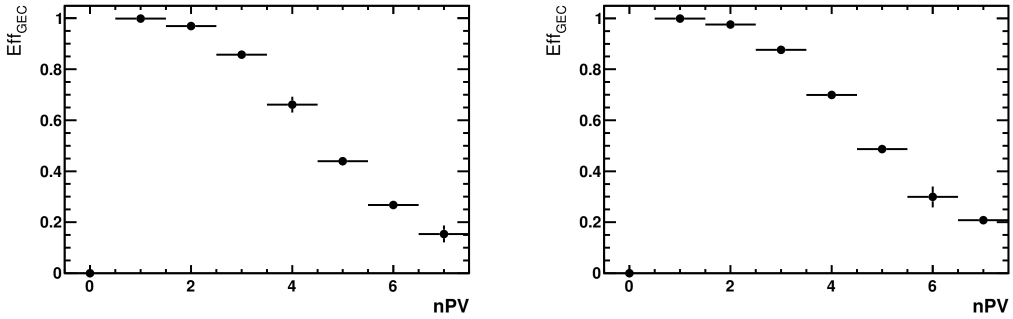

(c) 0x6D0032 magnet down.

(d) 0x730035 magnet up.

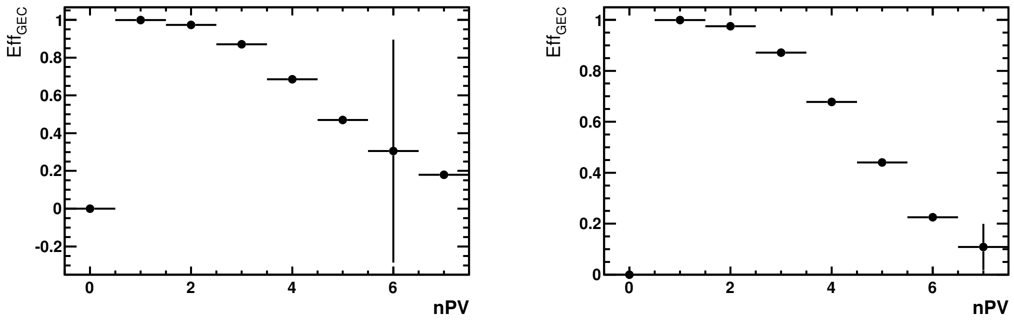

(e) 0x730035 magnet down.

(f) 0x760037 magnet up.

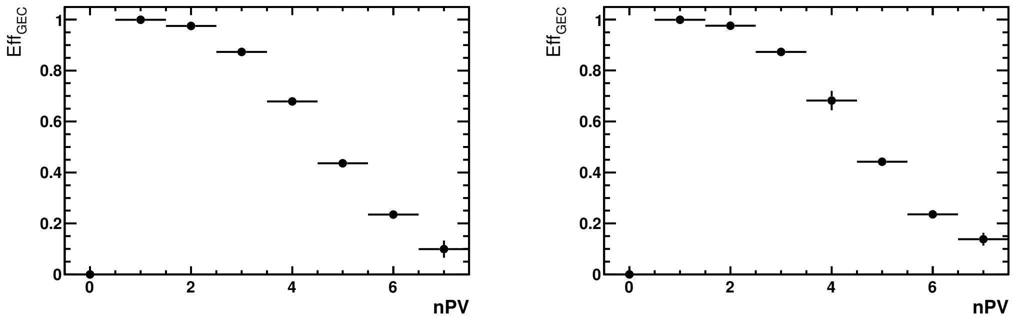

(g) 0x760037 magnet down.

(h) 0x790037 Up.

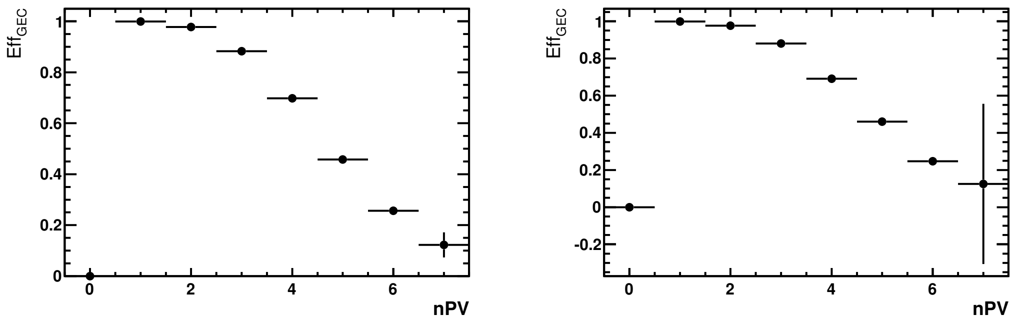

(i) 0x790038 magnet up.

(j) 0x790038 magnet down.

Figure D.0: The L0Muon global event cut efficiency by TCK.

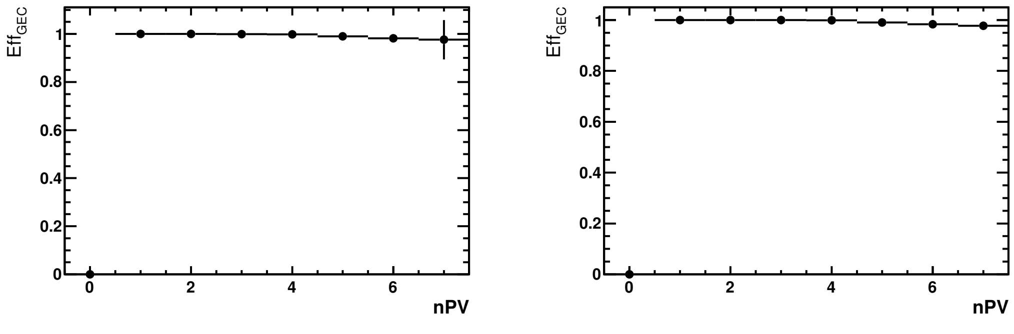

(a) 0x5A0032 magnet up.

(b) 0x5A0032 magnet down.

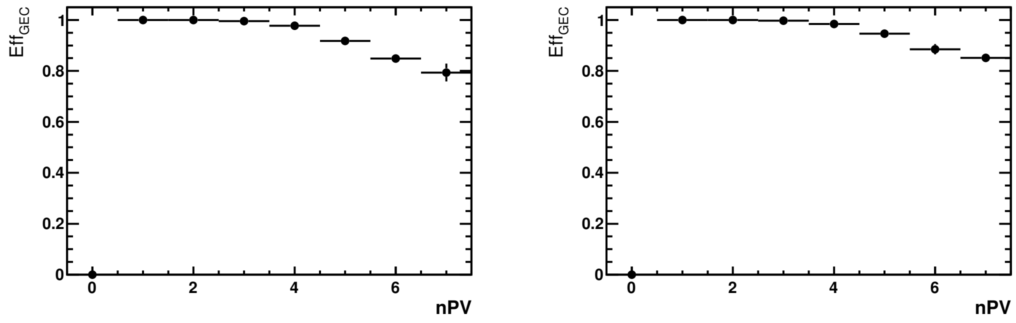

(c) 0x6D0032 magnet down.

(d) 0x730035 magnet up.

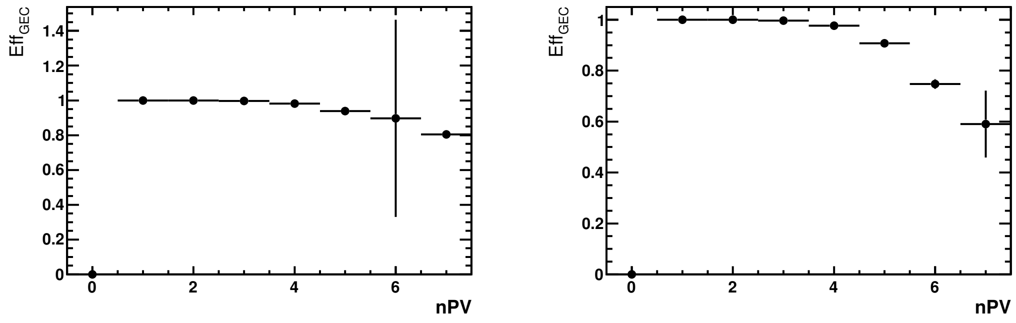

(e) 0x730035 magnet down.

(f) 0x760037 magnet up.

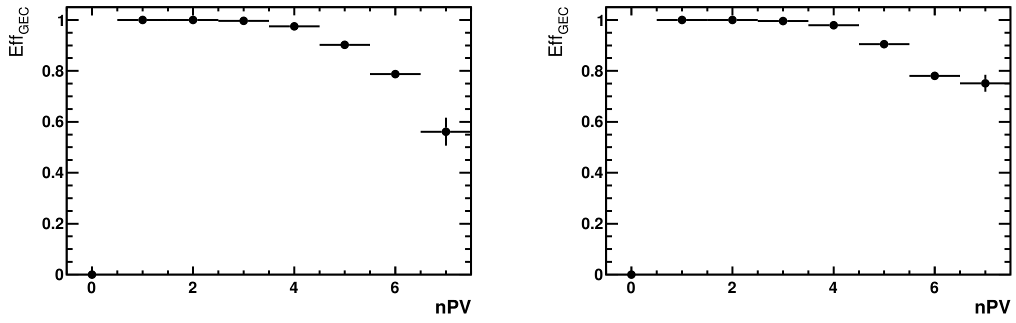

(g) 0x760037 magnet down.

(h) 0x790037 Up.

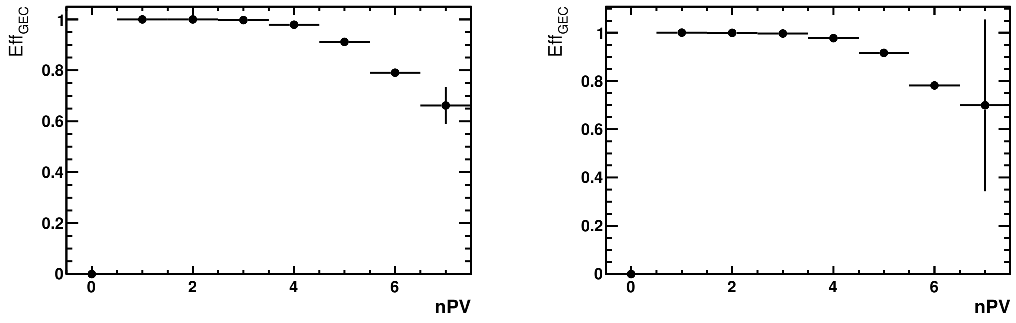

(i) 0x790038 magnet up.

(j) 0x790038 magnet down.

Figure D.0: The L0Muon global event cut efficiency by TCK.

Appendix E

Tabulated Differential Distributions

Table E.1: Cross-section as a function of the total p_{T}

p_{T} GeV/c^2	$\sigma_{J/\psi\, J/\psi}$ nb
0.50	0.61 ± 0.10(stat) ± 0.03(syst)
1.50	1.59 ± 0.32(stat) ± 0.29(syst)
2.50	1.17 ± 0.12(stat) ± 0.05(syst)
3.50	0.93 ± 0.12(stat) ± 0.04(syst)
4.50	0.45 ± 0.09(stat) ± 0.03(syst)
5.50	0.43 ± 0.05(stat) ± 0.02(syst)
6.50	0.35 ± 0.04(stat) ± 0.02(syst)
7.50	0.27 ± 0.06(stat) ± 0.01(syst)
8.50	0.12 ± 0.02(stat) ± 0.01(syst)
9.50	0.10 ± 0.02(stat) ± 0.01(syst)

Table E.2: Cross-section as a function of the total invariant mass.

Mass GeV/c	$\sigma_{J/\psi\, J/\psi}$ nb
0.16	0.68 ± 0.12(stat) ± 0.03(syst)
0.47	0.41 ± 0.11(stat) ± 0.03(syst)
0.79	0.56 ± 0.08(stat) ± 0.03(syst)
1.10	0.57 ± 0.17(stat) ± 0.08(syst)
1.41	0.56 ± 0.09(stat) ± 0.03(syst)
1.73	0.61 ± 0.10(stat) ± 0.04(syst)
2.04	0.70 ± 0.17(stat) ± 0.04(syst)
2.36	0.49 ± 0.08(stat) ± 0.03(syst)
2.67	0.59 ± 0.07(stat) ± 0.03(syst)
2.98	0.95 ± 0.20(stat) ± 0.09(syst)

Table E.3: Cross-section as a function of the absolute rapidity difference.

Δy	$\sigma_{J/\psi\,J/\psi}$ nb
0.20	2.65 ± 0.29(stat) ± 0.35(syst)
0.60	1.59 ± 0.15(stat) ± 0.07(syst)
1.00	1.11 ± 0.15(stat) ± 0.05(syst)
1.40	0.46 ± 0.07(stat) ± 0.03(syst)
1.80	0.28 ± 0.18(stat) ± 0.06(syst)

Table E.4: Cross-section as a function of difference in azimuthal angle.

$\Delta\phi$	$\sigma_{J/\psi\,J/\psi}$ nb
0.16	0.68 ± 0.12(stat) ± 0.03(syst)
0.47	0.41 ± 0.11(stat) ± 0.03(syst)
0.79	0.56 ± 0.08(stat) ± 0.03(syst)
1.10	0.57 ± 0.17(stat) ± 0.08(syst)
1.41	0.56 ± 0.09(stat) ± 0.03(syst)
1.73	0.61 ± 0.10(stat) ± 0.04(syst)
2.04	0.70 ± 0.17(stat) ± 0.04(syst)
2.36	0.49 ± 0.08(stat) ± 0.03(syst)
2.67	0.59 ± 0.07(stat) ± 0.03(syst)
2.98	0.95 ± 0.20(stat) ± 0.09(syst)

Bibliography

[1] **E598 Collaboration** Collaboration, J. Aubert *et al.*, “Experimental Observation of a Heavy Particle J,” *Phys.Rev.Lett.* **33** (1974) 1404–1406.

[2] **SLAC-SP-017 Collaboration** Collaboration, J. Augustin *et al.*, “Discovery of a Narrow Resonance in e+ e- Annihilation,” *Phys.Rev.Lett.* **33** (1974) 1406–1408.

[3] G. A. Schuler, “Quarkonium production and decays,” *Phys.Rept.* (1994) , `arXiv:hep-ph/9403387 [hep-ph]`.

[4] **CDF Collaboration** Collaboration, F. Abe *et al.*, “J/psi psi(2S) production in pp collisions at sqrt(s)=1.8 TeV,” *Phys.Rev.Lett.* **79** (1997) 578.

[5] **CDF Collaboration** Collaboration, A. Abulencia *et al.*, “Polarization of J/ψ and ψ_{2S} mesons produced in $p\bar{p}$ collisions at $\sqrt{s} = 1.96$-TeV,” *Phys.Rev.Lett.* **99** (2007) 132001, `arXiv:0704.0638 [hep-ex]`.

[6] N. Brambilla, S. Eidelman, P. Foka, S. Gardner, A. Kronfeld, *et al.*, “QCD and strongly coupled gauge theories: challenges and perspectives,” `arXiv:1404.3723 [hep-ph]`.

[7] A. Berezhnoy, A. Likhoded, A. Luchinsky, and A. Novoselov, “Double J/psi-meson Production at LHC and 4c-tetraquark state,” *Phys.Rev.* **D84** (2011) 094023, `arXiv:1101.5881 [hep-ph]`.

[8] S. Baranov, A. Snigirev, N. Zotov, A. Szczurek, and W. Schafer, “Interparticle correlations in the production of J/psi pairs in proton-proton collisions,” *Phys. Rev. D87,* **034035** (2013) , `arXiv:1210.1806 [hep-ph]`.

[9] **NA3 Collaboration** Collaboration, J. Badier *et al.*, “Evidence for psi psi production in pi- interactions at 150-GeV/c AND 280-GeV/c,” *Phys.Lett.* **B114** (1982) 457.

[10] **LHCb Collaboration** Collaboration, R. Aaij *et al.*, “Observation of J/ψ pair production in pp collisions at $\sqrt{s} = 7TeV$,” *Phys.Lett.* **B707** (2012) 52–59, `arXiv:1109.0963 [hep-ex]`.

[11] **CMS Collaboration** Collaboration, C. Collaboration, "Measurement of the Prompt Double J/psi Production Cross Section in pp Collisions at sqrt(s) = 7 TeV,".

[12] **D0 Collaboration** Collaboration, V. M. Abazov *et al.*, "Observation and studies of double J/psi production at the Tevatron," `arXiv:1406.2380 [hep-ex]`.

[13] **LHCb collaboration** Collaboration, A. A. Alves Jr. *et al.*, "The LHCb detector at the LHC," *JINST* **3** (2008) S08005.

[14] L. Evans and P. Bryant, "LHC Machine," *JINST* **3** (2008) S08001.

[15] S. Glashow, J. Iliopoulos, and L. Maiani, "Weak Interactions with Lepton-Hadron Symmetry," *Phys.Rev.* **D2** (1970) 1285–1292.

[16] G. Abrams, D. Briggs, W. Chinowsky, C. Friedberg, G. Goldhaber, *et al.*, "The Discovery of a Second Narrow Resonance in e+ e- Annihilation," *Phys.Rev.Lett.* **33** (1974) 1453–1455.

[17] **Particle Data Group** Collaboration, J. Beringer *et al.*, "Review of particle physics," *Phys. Rev.* **D86** (2012) 010001.

[18] J. Lansberg, "J/ψ, ψ ' and υ production at hadron colliders: A Review," *Int.J.Mod.Phys.* **A21** (2006) 3857–3916, `arXiv:hep-ph/0602091 [hep-ph]`.

[19] E. Braaten and T. C. Yuan, "Gluon fragmentation into heavy quarkonium," *Phys.Rev.Lett.* **71** (1993) 1673–1676, `arXiv:hep-ph/9303205 [hep-ph]`.

[20] N. Brambilla, S. Eidelman, B. Heltsley, R. Vogt, G. Bodwin, *et al.*, "Heavy quarkonium: progress, puzzles, and opportunities," *Eur.Phys.J.* **C71** (2011) 1534, `arXiv:1010.5827 [hep-ph]`.

[21] M. Kramer, "Quarkonium production at high-energy colliders," *Prog.Part.Nucl.Phys.* **47** (2001) 141–201, `arXiv:hep-ph/0106120 [hep-ph]`.

[22] **LHCb Collaboration** Collaboration, R. Aaij *et al.*, "Measurement of J/psi production in pp collisions at sqrt(s)=7 TeV," *Eur.Phys.J.* **C71** (2011) 1645, `arXiv:1103.0423 [hep-ex]`.

[23] H. Fritzsch, "Producing Heavy Quark Flavors in Hadronic Collisions: A Test of Quantum Chromodynamics," *Phys.Lett.* **B67** (1977) 217.

[24] F. Halzen, "Cvc for Gluons and Hadroproduction of Quark Flavors," *Phys.Lett.* **B69** (1977) 105.

[25] J. Amundson, O. J. Eboli, E. Gregores, and F. Halzen, "Colorless states in perturbative QCD: Charmonium and rapidity gaps," *Phys.Lett.* **B372** (1996) 127–132, `arXiv:hep-ph/9512248 [hep-ph]`.

[26] W. Caswell and G. Lepage, "Effective Lagrangians for Bound State Problems in QED, QCD, and Other Field Theories," *Phys.Lett.* **B167** (1986) 437.

[27] G. T. Bodwin, E. Braaten, and G. P. Lepage, "Rigorous QCD analysis of inclusive annihilation and production of heavy quarkonium," *Phys.Rev.* **D51** (1995) 1125–1171, `arXiv:hep-ph/9407339 [hep-ph]`.

[28] K.-T. Chao, Y.-Q. Ma, H.-S. Shao, K. Wang, and Y.-J. Zhang, "J/ψ Polarization at Hadron Colliders in Nonrelativistic QCD," *Phys.Rev.Lett.* **108** (2012) 242004, `arXiv:1201.2675 [hep-ph]`.

[29] **LHCb Collaboration** Collaboration, R. Aaij *et al.*, "Measurement of J/ψ polarization in pp collisions at $\sqrt{s} = 7$ TeV," *Eur.Phys.J.* **C73** (2013) 2631, `arXiv:1307.6379 [hep-ex]`.

[30] M. Butenschoen and B. A. Kniehl, "J/ψ production in NRQCD: A global analysis of yield and polarization," *Nucl.Phys.Proc.Suppl.* **222-224** (2012) 151–161, `arXiv:1201.3862 [hep-ph]`.

[31] B. Gong, L.-P. Wan, J.-X. Wang, and H.-F. Zhang, "Polarization for Prompt J/psi, psi(2s) production at the Tevatron and LHC," *Phys.Rev.Lett.* **110** (2013) 042002, `arXiv:1205.6682 [hep-ph]`.

[32] J. Lansberg, "On the mechanisms of heavy-quarkonium hadroproduction," *Eur.Phys.J.* **C61** (2009) 693–703, `arXiv:0811.4005 [hep-ph]`.

[33] **NA3 Collaboration** Collaboration, J. Badier *et al.*, "$\psi\psi$ Production and Limits on Beauty Meson Production From 400-GeV/c Protons," *Phys.Lett.* **B158** (1985) 85.

[34] A. Berezhnoy, A. Likhoded, A. Luchinsky, and A. Novoselov, "Double $c\bar{c}$ production at LHCb," *Phys.Rev.* **D86** (2012) 034017, `arXiv:1204.1058 [hep-ph]`.

[35] J.-P. Lansberg and H.-S. Shao, "J/psi-Pair Production at Large Momenta: Indications for Double-Parton Scatterings and Large alphas5 Contributions," `arXiv:1410.8822 [hep-ph]`.

[36] C.-F. Qiao, L.-P. Sun, and P. Sun, "Testing Charmonium Production Mechamism via Polarized J/psi Pair Production at the LHC," *J.Phys.* **G37** (2010) 075019, `arXiv:0903.0954 [hep-ph]`.

[37] P. Ko, C. Yu, and J. Lee, "Inclusive double-quarkonium production at the Large Hadron Collider," *JHEP* **1101** (2011) 070, `arXiv:1007.3095 [hep-ph]`.

[38] P. Bartalini, E. Berger, B. Blok, G. Calucci, R. Corke, *et al.*, "Multi-Parton Interactions at the LHC," `arXiv:1111.0469 [hep-ph]`.

[39] **Axial Field Spectrometer Collaboration** Collaboration, T. Akesson *et al.*, “Double Parton Scattering in pp Collisions at $\sqrt{s} = 63$-GeV,” *Z.Phys.* **C34** (1987) 163.

[40] **CDF Collaboration** Collaboration, F. Abe *et al.*, “Double parton scattering in $\bar{p}p$ collisions at $\sqrt{s} = 1.8$TeV,” *Phys.Rev.* **D56** (1997) 3811–3832.

[41] A. Novoselov, “Double parton scattering as a source of quarkonia pairs in LHCb,” `arXiv:1106.2184 [hep-ph]`.

[42] R. Maciula, M. Luszczak, and A. Szczurek, “Production of charm quark/antiquark pairs at LHC,” *PoS* **QNP2012** (2012) 125, `arXiv:1207.6533 [hep-ph]`.

[43] M. Bahr, M. Myska, M. H. Seymour, and A. Siodmok, “Extracting sigma effective from the CDF gamma+3jets measurement,” *JHEP* **1303** (2013) 129, `arXiv:1302.4325 [hep-ph]`.

[44] C. Kom, A. Kulesza, and W. Stirling, “Pair Production of J/psi as a Probe of Double Parton Scattering at LHCb,” *Phys.Rev.Lett.* **107** (2011) 082002, `arXiv:1105.4186 [hep-ph]`.

[45] C. Flensburg, G. Gustafson, L. Lonnblad, and A. Ster, “Correlations in double parton distributions at small x,” *JHEP* **1106** (2011) 066, `arXiv:1103.4320 [hep-ph]`.

[46] **CMS Collaboration** Collaboration, S. Chatrchyan *et al.*, “Observation of a new boson at a mass of 125 GeV with the CMS experiment at the LHC,” *Phys.Lett.* **B716** (2012) 30–61, `arXiv:1207.7235 [hep-ex]`.

[47] **ATLAS Collaboration** Collaboration, G. Aad *et al.*, “Observation of a new particle in the search for the Standard Model Higgs boson with the ATLAS detector at the LHC,” *Phys.Lett.* **B716** (2012) 1–29, `arXiv:1207.7214 [hep-ex]`.

[48] **LHCb Collaboration** Collaboration, M. Adamus *et al.*, “LHCb VELO TDR: Vertex locator. Technical design report,”.

[49] **LHCb VELO** Collaboration, S. De Capua, “Performance, radiation damage effects and upgrade of the LHCB vertex locator,” *Nucl.Instrum.Meth.* **A732** (2013) 70–73.

[50] R. Aaij, A. Affolder, K. Akiba, M. Alexander, S. Ali, *et al.*, “Performance of the LHCb Vertex Locator,” `arXiv:1405.7808 [physics.ins-det]`.

[51] **LHCb Collaboration** Collaboration, M. Adamus *et al.*, “LHCb: Inner tracker technical design report,”.

[52] **LHCb Collaboration** Collaboration, M. Adamus *et al.*, “LHCb: Outer tracker technical design report,”.

[53] **LHCb Collaboration** Collaboration, M. Adamus *et al.*, “LHCb: RICH technical design report,”.

[54] **LHCb Collaboration** Collaboration, M. Adinolfi *et al.*, “Performance of the LHCb RICH detector at the LHC,” *Eur.Phys.J.* **C73** (2013) 2431, `arXiv:1211.6759 [physics.ins-det]`.

[55] **LHCb Collaboration** Collaboration, M. Adamus *et al.*, “LHCb magnet: Technical design report,”.

[56] **LHCb Collaboration** Collaboration, M. Adamus *et al.*, “LHCb calorimeters: Technical design report,”.

[57] **LHCb** Collaboration, I. Machikhiliyan, “First years of running for the LHCb Calorimeter System,”.

[58] **LHCb calorimeters Collaboration** Collaboration, X. V. Cardona, “First years of running for the LHCb calorimeters,” *J.Phys.Conf.Ser.* **404** (2012) 012003.

[59] **LHCb Collaboration** Collaboration, M. Adamus *et al.*, “LHCb muon system technical design report,”.

[60] F. Archilli, W. Baldini, G. Bencivenni, N. Bondar, W. Bonivento, *et al.*, “Performance of the Muon Identification at LHCb,” *JINST* **8** (2013) P10020, `arXiv:1306.0249 [physics.ins-det]`.

[61] R. Aaij, J. Albrecht, F. Alessio, S. Amato, E. Aslanides, *et al.*, “The LHCb Trigger and its Performance in 2011,” *JINST* **8** (2013) P04022, `arXiv:1211.3055 [hep-ex]`.

[62] **LHCb Collaboration** Collaboration, “LHCb trigger system technical design report,”.

[63] G. Barrand, I. Belyaev, P. Binko, M. Cattaneo, R. Chytracek, *et al.*, “GAUDI - A software architecture and framework for building HEP data processing applications,” *Comput.Phys.Commun.* **140** (2001) 45–55.

[64] **LHCb Collaboration** Collaboration, G. Corti, “LHCb computing,” *Nucl.Instrum.Meth.* **A462** (2001) 265–269.

[65] **LHCb Collaboration** Collaboration, M. Clemencic *et al.*, “The LHCb simulation application, Gauss: Design, evolution and experience,” *J.Phys.Conf.Ser.* **331** (2011) 032023.

[66] T. Sjöstrand, S. Mrenna, and P. Skands, "PYTHIA 6.4 physics and manual," *JHEP* **05** (2006) 026, `arXiv:hep-ph/0603175 [hep-ph]`.

[67] D. J. Lange, "The EvtGen particle decay simulation package," *Nucl. Instrum. Meth.* **A462** (2001) 152–155.

[68] P. Golonka and Z. Was, "PHOTOS Monte Carlo: a precision tool for QED corrections in Z and W decays," *Eur.Phys.J.* **C45** (2006) 97–107, `arXiv:hep-ph/0506026 [hep-ph]`.

[69] **GEANT4 collaboration** Collaboration, J. Allison, K. Amako, J. Apostolakis, H. Araujo, P. Dubois, *et al.*, "Geant4 developments and applications," *IEEE Trans.Nucl.Sci.* **53** (2006) 270.

[70] **GEANT4 collaboration** Collaboration, S. Agostinelli *et al.*, "GEANT4: A simulation toolkit," *Nucl. Instrum. Meth.* **A506** (2003) 250.

[71] M. Clemencic *et al.*, "The LHCb simulation application, Gauss: design, evolution and experience," *J. of Phys.: Conf. Ser.* **331** (2011) 032023.

[72] J. Seguinot and T. Ypsilantis, "Photoionization and Cherenkov Ring Imaging," *Nucl.Instrum.Meth.* **142** (1977) 377.

[73] J. Seguinot and T. Ypsilantis, "A Historical survey of ring imaging Cherenkov counters," *Nucl.Instrum.Meth.* **A343** (1994) 1–29.

[74] A. Gorisek, P. Krizan, S. Korpar, and M. Staric, "Alignment of the HERA-B RICH optical system with data," *Nucl.Instrum.Meth.* **A433** (1999) 408–412.

[75] W. Adam, E. Albrecht, D. Allen, M. Andrieux, G. van Apeldoorn, *et al.*, "The ring imaging Cherenkov detectors of DELPHI," *IEEE Trans.Nucl.Sci.* **42** (1995) 499–504.

[76] N. Brook, M. Coombes, T. Hampson, and A. Solomin, "The software framework and method for the alignment of the LHCb RICH optical system using proton-proton collisions," Tech. Rep. CERN-LHCb-INT-2013-007, CERN, Geneva, 2013.

[77] C. G. Blanks, "V^0 production ratios at LHCb and the alignment of its RICH detectors,".

[78] T. R. Hampson, "Measurement of prompt charm production and the decay $D^0 \to K^+\pi^-\pi^+\pi^-$ at LHCb,".

[79] J. Albrecht, V. Gligorov, G. Raven, and S. Tolk, "Performance of the LHCb High Level Trigger in 2012," `arXiv:1310.8544 [hep-ex]`.

[80] C. D'Ambrosio, L. Fernndez, M. Laub, and D. Piedigrossi, "The optical systems of LHCb RICHes : a study on the mirror walls and mirrors specifications,".

[81] A. Apollonio *et al.*, "HL-LHC:Integrated Luminosity and Availablity,".

[82] M. Pivk and F. R. Le Diberder, "SPlot: A Statistical tool to unfold data distributions," *Nucl.Instrum.Meth.* **A555** (2005) 356–369, `arXiv:physics/0402083 [physics.data-an]`.

[83] **LHCb Collaboration** Collaboration, X. Cid Vidal, "Muon Identification in the LHCb experiment," `arXiv:1005.2585 [hep-ex]`.

[84] R. Aaij and J. Albrecht, "Muon triggers in the High Level Trigger of LHCb,".

[85] E. Rodrigues, "Dealing with clones in the tracking,".

[86] **LHCb** Collaboration, M. Needham, "Clone Track Identification using the Kullback-Liebler Distance,".

[87] **LHCb collaboration** Collaboration, R. Aaij *et al.*, "Absolute luminosity measurements with the LHCb detector at the LHC," *JINST* **7** (2012) P01010, `arXiv:1110.2866 [hep-ex]`.

[88] **LHCb** Collaboration, R. Aaij *et al.*, "LHCb Detector Performance," `arXiv:1412.6352 [hep-ex]`.

[89] M. Needham, "Identification of Ghost Tracks using a Likelihood Method,".

[90] A. Jaeger, P. Seyfert, M. De Cian, J. van Tilburg, and S. Hansmann-Menzemer, "Measurement of the track finding efficiency,".

[91] W. D. Hulsbergen, "Decay chain fitting with a Kalman filter," *Nucl.Instrum.Meth.* **A552** (2005) 566–575, `arXiv:physics/0503191 [physics]`.

[92] **LHCb collaboration** Collaboration, R. Aaij *et al.*, "Production of J/ψ and Υ mesons in pp collisions at $\sqrt{s} = 8$ TeV," *JHEP* **1306** (2013) 064, `arXiv:1304.6977 [hep-ex]`.

[93] D. Martnez Santos and F. Dupertuis, "Mass distributions marginalized over per-event errors," *Nucl.Instrum.Meth.* **A764** (2014) 150–155, `arXiv:1312.5000 [hep-ex]`.

[94] J. Hernando Morata, E. Lopez Asamar, D. Martinez Santos, H. Ruiz-Perez, and F. Teubert, "Measurement of trigger efficiencies and biases,".

[95] **LHCb Collaboration** Collaboration, R. Aaij *et al.*, "Measurement of b-hadron masses," *Phys.Lett.* **B708** (2012) 241–248, `arXiv:1112.4896 [hep-ex]`.

[96] M. Bahr, S. Gieseke, M. Gigg, D. Grellscheid, K. Hamilton, *et al.*, "Herwig++ Physics and Manual," *Eur.Phys.J.* **C58** (2008) 639–707, `arXiv:0803.0883 [hep-ph]`.

[97] A. Martin, W. Stirling, R. Thorne, and G. Watt, "Parton distributions for the LHC," *Eur.Phys.J.* **C63** (2009) 189–285, `arXiv:0901.0002 [hep-ph]`.

[98] J. Pumplin, D. Stump, J. Huston, H. Lai, P. M. Nadolsky, *et al.*, "New generation of parton distributions with uncertainties from global QCD analysis," *JHEP* **0207** (2002) 012, `arXiv:hep-ph/0201195 [hep-ph]`.

[99] **CTEQ Collaboration** Collaboration, H. Lai *et al.*, "Global QCD analysis of parton structure of the nucleon: CTEQ5 parton distributions," *Eur.Phys.J.* **C12** (2000) 375–392, `arXiv:hep-ph/9903282 [hep-ph]`.

[100] Y.-S. Zhu, "On Statistical Significance of Signal," *HEPNP* **30** (2006) 331–334, `arXiv:0812.2708 [physics.data-an]`.